Trends in neutron single-particle energies below $N=82$

A thesis submitted to the University of Manchester for the degree of

Doctor of Philosophy

in the Faculty of Engineering and Physical Sciences

2011

Alan Michael Howard

School of Physics and Astronomy

CONTENTS

Final word count: 21,365

ABSTRACT

Two separate investigations are described, linked by their common interest in single-particle structure around the N=82 shell closure.

A systematic study of single-particle strength below the N=82 shell closure is reported. States in ^{137}Ba, ^{139}Ce, ^{141}Nd and ^{143}Sm were populated using the single-neutron removal reactions (p,d) and (^{3}He,α) at beam energies of 23 MeV and 34 MeV, respectively. Absolute cross sections are presented for all observed states. Relative spectroscopic factors have been determined through a DWBA analysis. The observed $g_{7/2}$ strength is consistently lower than that of $h_{11/2}$ across all four isotones. It is postulated that as much as 50% of the $g_{7/2}$ strength is fragmented into unresolved states which form part of the reaction background below 3.5 MeV. A speculative analysis based upon the observed strength reveals a relative behaviour of the $g_{7/2}$ and $h_{11/2}$ centroid energies that is in qualitative agreement with the predicted action of the tensor force.

Details are presented also from an exploratory study of the ^{132}Sn region using the ^{136}Xe + ^{238}U reaction at 926 MeV. The time-of-flight spectrometer PRISMA was used to identify the beam-like reaction products, and a mass resolution $> 1/200$ and Z-resolution of $\sim 1/60$ is reported. The total production yields at the focal plane are compared to calculations using the multi-nucleon transfer code GRAZING and rather poor agreement found for transfer of more then a few nucleons. The prospects for future studies in the region, particularly lifetime measurements, are discussed.

DECLARATION

No portion of the work referred to in this thesis has been submitted in support of an application for another degree or qualification of this or any other university or other institute of learning.

COPYRIGHT STATEMENT

(i) The author of this thesis (including any appendices and/or schedules to this thesis) owns certain copyright or related rights in it (the Copyright) and s/he has given The University of Manchester certain rights to use such Copyright, including for administrative purposes.

(ii) Copies of this thesis, either in full or in extracts and whether in hard or electronic copy, may be made only in accordance with the Copyright, Designs and Patents Act 1988 (as amended) and regulations issued under it or, where appropriate, in accordance with licensing agreements which the University has from time to time. This page must form part of any such copies made.

(iii) The ownership of certain Copyright, patents, designs, trade marks and other intellectual property (the Intellectual Property) and any re- productions of copyright works in the thesis, for example graphs and tables (Reproductions), which may be described in this thesis, may not nbe owned by the author and may be owned by third parties. Such Intellectual Property and Reproductions cannot and must not be made available for use without the prior written permission of the owner(s) of the relevant Intellectual Property and/or Reproductions.

(iv) Further information on the conditions under which disclosure, publication and commercialisation of this thesis, the Copyright and any Intellectual Property and/or Reproductions described in it may take

ACKNOWLEDGEMENTS

I must begin by thanking Prof. Sean Freeman whose guidance throughout my PhD, in areas both academic and otherwise, has been both invaluable and unfaltering. His supervision has been, without doubt, first rate. I can only apologise for never getting round to painting those fascias. The additional assistance I have received from Ben Kay, Alick Deacon and, more recently, Jeffry Thomas has also been exceptional and is gratefully acknowledged. I must thank Jeff in particular for introducing me to the musical and culinary delights of Katsouris.

Thanks go to the entire Nuclear Group at Manchester for the three wonderful years I have spent there. Special thanks go to Joesph Dare for making lunch breaks educational; Dave Steppenbeck, Pete Mason and Nicola Lumley for the 'Belgian power hour'; David Sharp and Mark Procter for that curry in Leicester (as well as so many others) and AJ Mitchell, Sean McAllister, Paul Campbell and Bradley Cheal for many enlightening post-work discussions. Additional thanks go to Paul Campbell for proving that good things (from Sainsburys at least) come in red circles.

The experiments at Yale could not have succeeded without the help, experience and dedication of Peter Parker and our Argonne collaborators; John Schiffer, Catherine Deibel and Jason Clark. Our stays in New Haven were made all the more enjoyable by the bed and breakfast (and eggs!) provided by Janet Seltzer. The kind assistance of both Jose-Javier Valiente Dobon and Andres Gadea is gratefully acknowledged during my time at LNL. I would

also like to acknowledge the receipt of funding from the STFC which has made this work possible.

I am eternally grateful to my parents for their unwavering love and support over the years, even when it became obvious I was simply putting off getting a 'real' job. Finally I must thank Birgit for being quite simply wonderful. ILD.

Alan Michael Howard
2010

CHAPTER

ONE

SHELL STRUCTURE OF THE NUCLEUS

Understanding the atomic nucleus constitutes an enormous challenge. It is a highly complex quantum-mechanical system, containing as many as 250 nucleons undergoing many-body interactions. The strong force via which these nucleons interact is itself not fully understood, emphasising the scale of this challenge. Nonetheless, huge progress has been made towards this goal.

1.1 The nucleon-nucleon interaction

Although a precise, analytic description of the strong force is not known at present, many aspects of the nucleon-nucleon interaction are well established. For example, based upon experimental observations (details of which may be found in many textbooks, such as Refs. [1, 2]),

- The existence of nuclei requires that the interaction be attractive and sufficiently strong to overcome the Coulomb repulsion between protons in the nucleus.

- The interaction has a range of the order 1-2 fm. This is seen in the saturation of nucleon binding energies, where only 'touching' nuclei

interact.

- Scattering measurements indicate that nucleons exhibit a hard core, with the interaction becoming strongly repulsive at separations below ~ 0.5 fm.

- There exists a non-central tensor component of the interaction, evidenced by the non-zero quadrupole moment of the deuteron.

- The similar structure exhibited by mirror nuclei, in which the proton and neutron numbers are swapped, indicate the force is charge symmetric.

Using the available data phenomenological models of the nucleon-nucleon interaction have been constructed. *Ab initio* calculations have attempted to model nuclear systems from the ground up on the basis of these interactions. Although successful for light systems, the computational power required for such calculations increases rapidly with mass as the model-space expands. For nuclei more massive than $A \sim 12$, a different approach is required.

1.2 The nuclear shell model

Evidence for the shell-like structure of the atomic nucleus is plentiful. At certain so-called 'magic numbers' of protons and neutrons, nuclei show signs of increased stability and adopt spherical, stable structures. This is observed in measurements of nuclear masses, radii and quadrupole moments, for example [2]. This shell structure is familiar in atomic physics; electrons move independently within a central potential created by the positively-charged nucleus, and fill orbits of definite angular momentum in accordance with the Pauli exclusion principle.

Applying a similar treatment to the nucleus may at first seem unreasonable; the assumption of independent motion is at odds with having many strongly interacting bodies in close proximity. The ability of nucleons to

scatter from each other, however, is dependent on there existing open channels to scatter into. If all states up to the Fermi energy are occupied, which represents the lowest energy state of the system, then scattering must take place to states above the Fermi energy. Thus the process becomes sufficiently hindered that independent-particle motion becomes a reasonable approximation.

Mean-field potentials

The potential in which the nucleons move is, as discussed, complicated. To reduce the problem to a manageable scale the concept of a mean-field potential is introduced. This represents the time-averaged potential created by the motion of the individual nucleons, and is modelled as a central force. As the strong interaction is short-ranged, the potential is usually chosen to reflect the matter density of the nucleus.

A common parametrisation is the harmonic oscillator (HO) potential, defined as

$$U_{HO}(r) = \frac{1}{2}m\omega^2 r^2, \tag{1.1}$$

where m is the nucleon mass and ω the frequency of oscillation. Analytic solutions to the Schrödinger equation are known for the HO potential which greatly simplifies calculations. The form of the potential is unrealistic at large radii, however, as the potential tends to infinity. If any degree of accuracy is demanded at these radii a correction factor proportional to $-\ell^2$ is required.

A more realistic parametrisation, at the cost of analytic solutions, is the Woods-Saxon potential

$$U_{WS}(r) = \frac{V_0}{1 + e^{\frac{r-R}{a}}}, \tag{1.2}$$

where V_0 is the well depth, R the nuclear radius and a the diffuseness of the nuclear surface. The relative forms of the HO and Woods-Saxon potentials are shown in Fig. 1.1.

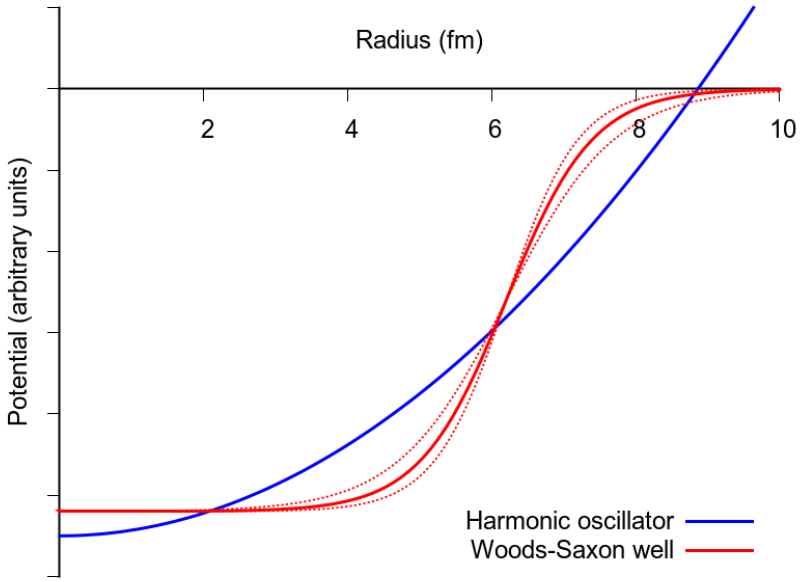

Figure 1.1: Two commonly used parametrisations of the mean-field potential, the harmonic oscillator and the Woods-Saxon well. The dotted lines illustrate the effect of a 20 % variation in the surface diffusivity parameter of the Woods-Saxon well.

The Hamiltonian for a nucleon moving in these potentials is written

$$\hat{h}_i = \frac{\hat{p}_i^2}{2m_i} + U(r_i). \tag{1.3}$$

where the first term is the kinetic energy of the nucleon and the second term the mean-field potential. The Schrödinger equation for these nucleons is

$$\hat{h}_i \mid \phi_i >= \epsilon_i \mid \phi_i > . \tag{1.4}$$

The eigenvalues of Eqn. 1.4 are the individual nucleon energies and the eigenfunctions their wave functions. The nuclear Hamiltonian is the sum of the individual $\hat{h}_i$

$$\hat{H} = \sum_i \hat{h}_i, \tag{1.5}$$

which yields eigenfunctions of the Schrödinger equation which are products

of the individual nucleon wave functions,

$$| \varphi\rangle = \prod_i | \phi_i\rangle. \tag{1.6}$$

To satisfy the Pauli exclusion principle the overall nuclear wave function must be antisymmetric under the exchange of like nucleons. Mathematically this is dealt with using Slater determinants,

$$|\phi_1, \cdots, \phi_A\rangle = \frac{1}{\sqrt{A!}} \begin{bmatrix} \phi_1(r_1) & \phi_1(r_2) & \cdots & \phi_1(r_A) \\ \phi_2(r_1) & \phi_2(r_2) & \cdots & \phi_2(r_A) \\ \vdots & \vdots & \ddots & \vdots \\ \phi_A(r_1) & \phi_A(r_2) & \cdots & \phi_A(r_A) \end{bmatrix}. \tag{1.7}$$

Spin-orbit interaction

The single-nucleon energies that result from the mean-field potentials described above exhibit the energy clustering of states required to produce shell effects. The magic numbers that characterise these shells are however only in agreement for the first three closures, observed at nucleon numbers of 2, 8 and 20. This discrepancy suggests that an aspect of the potential has been neglected, and this is found to be the spin-orbit interaction. The form of this additional potential is

$$V_{SO}(r) = -V_{ls} \frac{1}{r} \frac{\partial U(r)}{\partial r} \boldsymbol{l} \cdot \boldsymbol{s}, \tag{1.8}$$

which produces opposing results for spin-orbit partners (states with the same ℓ, but opposite projections of the intrinsic spin).

As illustrated in Fig. 1.2, the inclusion of the spin-orbit interaction lifts the j degeneracy of the single-particle energies; the $j = \ell + s$ partner is pushed down in energy and the $j = \ell - s$ partner pushed up. The magnitude of the splitting is described by

$$\Delta E \propto \frac{1}{2}(2\ell + 1)\hbar^2, \tag{1.9}$$

which for high ℓ becomes sufficiently large to alter the magic-numbers, splitting the two states over different shells.

Configuration mixing

The single-nucleon Hamiltonian in Eqn. 1.3 contains an approximate potential using a mean-field description. A more accurate, though far more complex, potential is described by the sum of all two-body interactions experienced by the nucleon

$$V = \sum_{j \neq i} V_{ij}(\boldsymbol{r}_i, \boldsymbol{r}_j), \tag{1.10}$$

where j runs over all other nucleons. Using the definition of the nuclear Hamiltonian in Eqn. 1.5, this can be written explicitly as

$$\hat{H} = \sum_i \underbrace{\left[\frac{\hat{p}_i^2}{2m_i} + U(r_i)\right]}_{\hat{H}_0} + \sum_i \underbrace{\left[\sum_{j \neq i} V_{ij} - U(r_i)\right]}_{\hat{H}_{res}}. \tag{1.11}$$

In this form $\hat{H}_0$ represents the mean-field Hamiltonian introduced earlier and $\hat{H}_{res}$ describes residual interactions which arise due to the approximate nature of the mean-field potential. The magnitude of $\hat{H}_{res}$ is governed by the choice of mean field, but in practice is always sufficiently large to require attention and too large to consider as a small perturbation.

The effect of the residual interactions is to mix the single-particle configurations generated by the mean-field Hamiltonian to give eigenfunctions with the form

$$\mid \psi_k \rangle = \sum_i a_{ik} \mid \varphi_i \rangle, \tag{1.12}$$

where a_{ik} is the contribution of each single-particle configuration in the resulting wave function, and $a^* a$ the probability of measuring each φ_i (also referred to as the strength). The energies of the underlying single-particle orbitals are determined by the centroid of this strength. The techniques in-

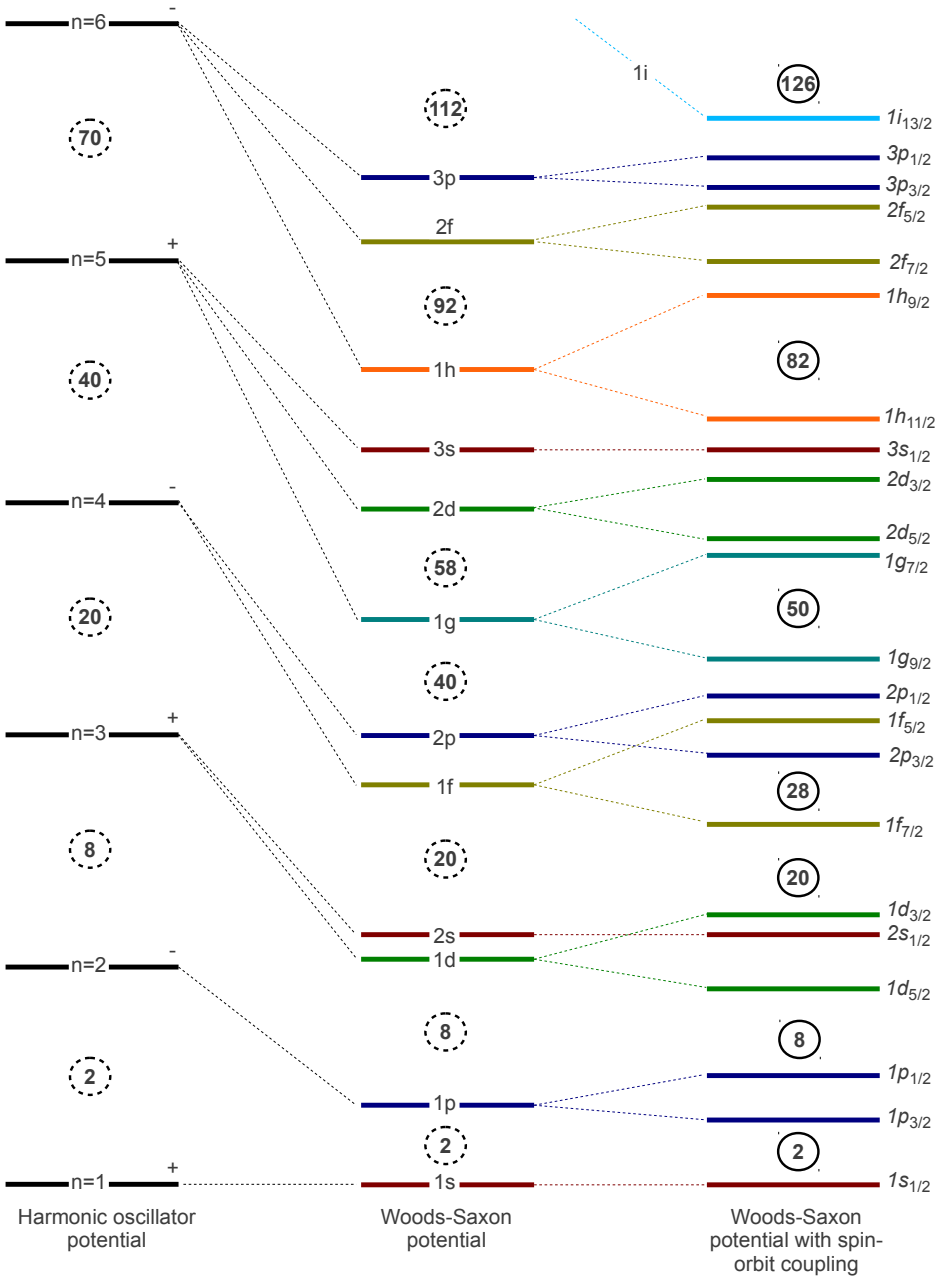

Figure 1.2: Illustrative diagram of single-particle levels in the nuclear shell model. From left to right the levels are calculated using a harmonic oscillator potential, a Woods-Saxon potential and finally with the addition of a spin-orbit interaction. The circled numbers are the 'magic numbers' of nucleons required to fill up to each shell closure.

volved in measuring single-particle strengths are the subject of later chapters of this thesis.

It is noted that in the shell-model only valence nucleons (i.e. those outside a shell closure) contribute to $\hat{H}_{res}$, with the remaining nucleons forming an inert core. The problem is thus reduced dramatically, particularly near doubly-magic nuclei where only a few valence nucleon interactions need be considered. It is, therefore, unsurprising that is for these nuclei that the shell-model has the greatest predictive power.

1.3 Evolution of shell structure

The relative energies of the single-particle orbitals are not fixed quantities. The picture presented in Fig. 1.2 is only an approximation for nuclei in the valley of stability, which themselves represent only a small fraction of the known nuclear landscape. As experimental techniques and facilities have developed, so has the knowledge of nuclei in more exotic regions. This has revealed evidence for the evolution of nuclear structure, through changes in these underlying single-particle energies.

The monopole shift

It is well known that the interactions between valence protons and neutrons are important in the context of shell evolution [1]. The addition of valence protons directly affects neutron single-particle energies, and vice-versa. The magnitude of this effect is described by the monopole component of the interaction responsible, written as [3]

$$V_{j_1 j_2} = \frac{\sum_J (2J+1)\langle j_1 j_2 \mid V \mid j_1 j_2 \rangle}{\sum_J (2J+1)}. \tag{1.13}$$

This represents the angle-averaged effect of the interaction described by the two-body matrix elements $\langle j_1 j_2 \mid V \mid j_1 j_2 \rangle$. The j dependence is removed in this form and only the number of nucleons in each orbit is important. The

resulting change in single-particle energies is referred to as the monopole shift.

The central component of the π-ν interaction results in an attractive force between orbitals. Due to the short-range nature of the force, the magnitude depends also on the radial overlap between the interacting orbitals. Where this is large the nucleon pairs spend more time in close proximity, and so the average effect is greater. This interaction is well illustrated by the closing of the Z=64 shell gap in the $A \sim 150$ region [4]. At $N \gtrsim 83$ neutrons begin to fill the $1h_{9/2}$ orbital. This has a large radial overlap with the proton $1h_{11/2}$ orbital, and so acts to pull it down in energy. The large energy-spacing above the $2d_{5/2}$ proton orbital is reduced by this action and thus the Z=64 shell gap vanishes.

The tensor interaction

Further work on the role of the π-ν interaction has been prompted by the observation of phenomena not reproduced by the central component of the interaction. For example, in light, neutron-rich systems a new shell-gap opens at N=16 [5]. It has been shown that this behaviour is reproduced through the inclusion of an interaction favouring spin-flip, isospin-flip partners in the monopole shift [3]. In ^{24}O, where the N=16 gap is reported, there are no valence protons in the *sd*-shell. In ^{30}Si, where the more familiar N=20 gap is present, there are six valence protons in the $d_{5/2}$ orbital which have a particularly strong attraction with neutrons in the $d_{3/2}$ orbital. This pulls both orbitals down in energy, quenching the N=16 gap. This situation is illustrated in Fig. 1.3.

The tensor component of the nucleon-nucleon interaction has the properties described above [6]. It produces a force proportional to the operator [7]

$$S_{12} = 3\frac{(\boldsymbol{\sigma_1} \cdot \boldsymbol{r})(\boldsymbol{\sigma_2} \cdot \boldsymbol{r})}{r^2}\boldsymbol{\sigma_1} \cdot \boldsymbol{\sigma_2}, \tag{1.14}$$

where $\boldsymbol{\sigma_i}$ are the spin-components of the interacting nucleons and $\boldsymbol{r}$ the vector

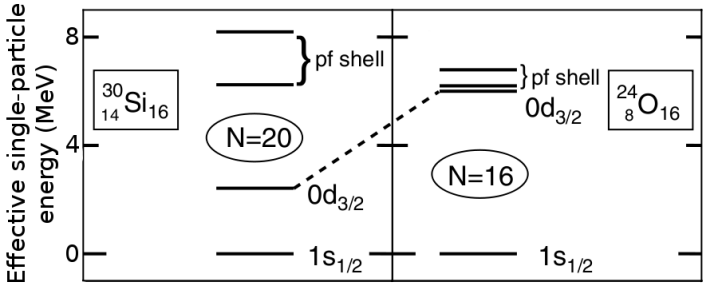

Figure 1.3: The opening of a shell-gap at N=16 near the neutron drip line. The additional protons in ^{30}Si relative to ^{24}O are primarily in a $d_{5/2}$ orbital which acts to lower the energy of the spin-flip, isospin-flip neutron $d_{3/2}$ orbital. Figure adapted from Ref. [3].

connecting them. If the interacting nucleon-pair couple to a spin-singlet state then $S_{12} = 0$. Only the $S = 1$ spin-triplet is therefore affected.

The dependence of the force on whether the interacting orbitals have $j_<$ $(= \ell - s)$ or $j_>$ $(= \ell + s)$ can be qualitatively understood with reference to Fig. 1.4. For a $j_<$ $j_>^{'}$ pair (see Fig. 1.4(a)) there is a large relative momentum component between the nucleons. Due to the uncertainty principle this results in a narrow spatial wave function of relative motion, orientated parallel to the total spin projection. This coupling of σ and r results in a positive S_{12} and hence an attractive interaction. For large ℓ and $\ell^{'}$ the relative momentum is greater resulting in a narrower, better aligned spatial wave function, and hence a more attractive interaction. For a $j_<$ $j_<^{'}$ pair (see Fig. 1.4(b)) this argument is reversed and the vector r is perpendicular to the spin projection. The value of S_{12} is therefore negative, giving rise to a repulsive interaction.

Realistic nucleon-nucleon interactions have been developed which contain both the central and tensor components of the nuclear force [8, 9]. The calculation of monopole-shifts using these interactions indicate that global trends in single-particle energies are well reproduced by the central component alone. The tensor component manifests itself in localised, relative shifts between high-ℓ $j_<$ and $j_>$ orbitals, coinciding with the filling of high-ℓ orbitals of opposite isospin. This characteristic behaviour results in rather dramatic effects in some systems, for instance the quenching of the N=20 shell gap.

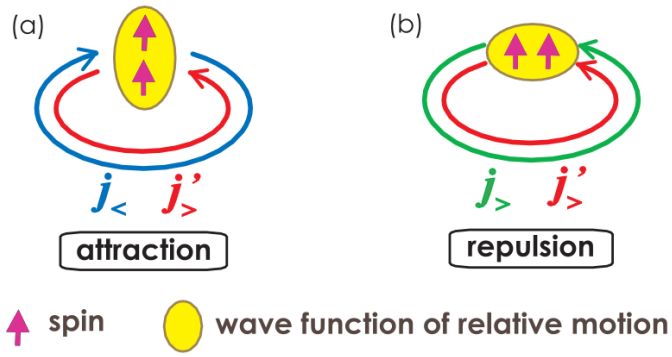

Figure 1.4: Illustrative diagram of nucleon pairs interacting via a tensor force in the case of a) alligned spin and anti-aligned angular momenta and b) aligned spin and angular momenta. In case a) the resulting force is attractive whereas in case b) it is repulsive. Figure from Ref. [6].

In most situations the effects are more subtle, however.

The use of transfer reactions to measure the fragmentation of single-particle strength is well established, and gives the opportunity to make accurate measurements of single-particle energies. Regardless of whether large structural changes result from the effects of the tensor force, its action should still be reflected in these energies. They provide a valuable source of information regarding both the strength and robustness of the interaction, and against which the realistic interactions discussed can be tested

Such measurements have been made across the Z=51 isotopes. The energy-separation between the lowest lying $7/2^+$ and $11/2^-$ states is found to increase by $\sim$ 2 MeV between ^{113}Sb and ^{125}Sb, as shown in Fig. 1.5. Since the Sb isotopes are formed from a single valence-proton outside of a Sn core, it seems reasonable to assume that these should correspond to excitations of the proton to the $1g_{7/2}$ and $1h_{11/2}$ orbitals. Single-proton adding reactions on the stable, even-mass Sn isotopes have confirmed that these lowest states carry $\sim$ 90 % of the single particle strength [10], and that the inclusion of the higher lying strength does not effect the trend observed [11].

It has been suggested that the splitting of these orbitals is a direct consequence of the tensor interaction [6]. The neutrons filling the Sn core between ^{112}Sn and ^{124}Sn increase the occupancy of the $\nu h_{11/2}$ orbital, as is shown in

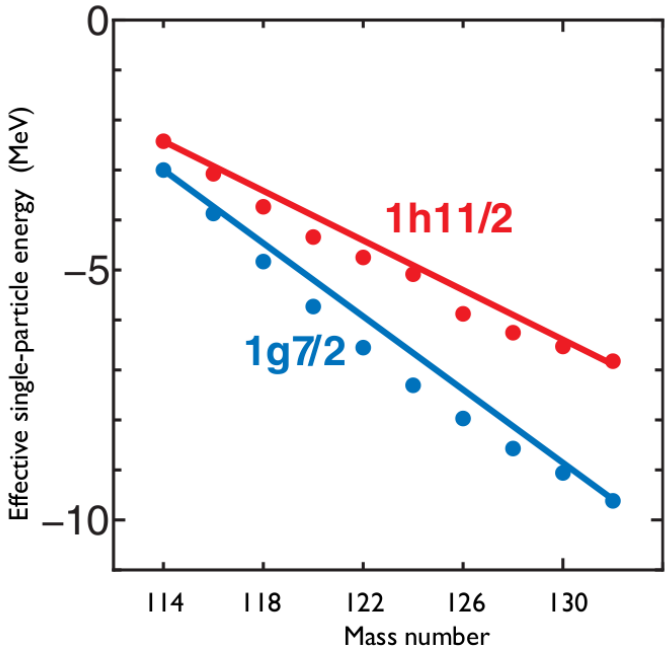

Figure 1.5: Trends in the single-particle energies of the proton $g_{7/2}$ and $h_{11/2}$ orbitals in Sb isotopes. The solid lines represent calculations including the tensor force. Figure from Ref. [6].

Fig. 1.6. The large radial overlap between this orbital and the $\pi g_{7/2}$ and $\pi h_{11/2}$ orbitals results in strong nucleon-nucleon interactions. As these are all high-ℓ states, the tensor component of the interaction is maximised and acts repulsively for the $j_>$ $h_{11/2}$ and attractively for the $j_<$ $g_{7/2}$. The measured splitting of these orbitals is compared to that expected from the tensor interaction in Fig. 1.5. and the trends in both cases found to be in good agreement.

Across the stable N=82 isotones there is again the filling of a high-ℓ orbital, and so the characteristic splitting of high-j states by the tensor interaction is expected. In this instance it is the $\pi g_{7/2}$ occupancy which is increasing, as shown in Fig 1.7. In the N=83 isotones, formed by an N=82 core plus valence neutron, measurements have been made of the single-particle energies of the high-j $h_{9/2}$ and $i_{13/2}$ states [12]. The fragmentation of strength is greater than observed in the Sb isotopes with the lowest states carrying ∼70% of the strength. The energy-separation between these orbitals, together with

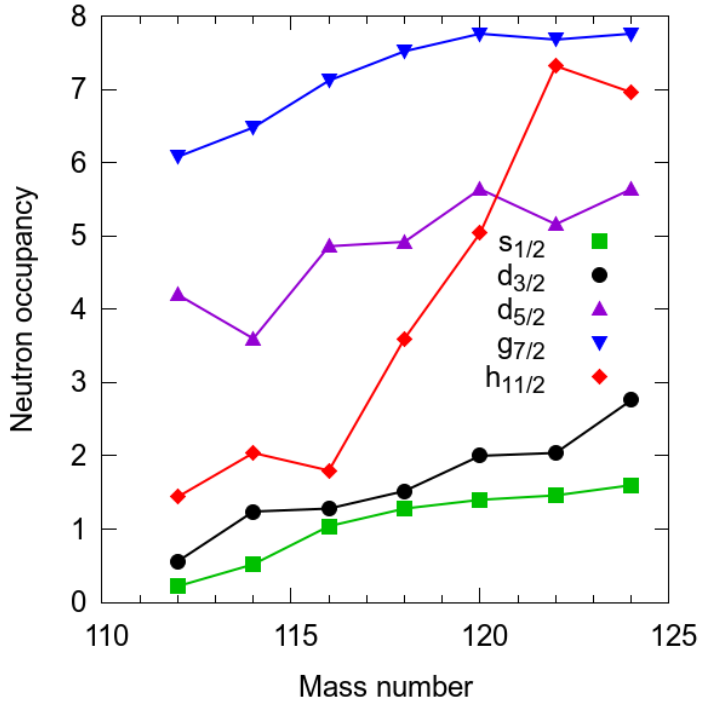

Figure 1.6: Occupancies of neutron orbitals in the stable Sn nuclei. Figure adapted from Ref. [11].

calculations using the tensor force, are in Fig. 1.8. The agreement between measured and predicted values is again very good. The data shown do include the strength found in higher lying fragments, although the trend differs only slightly from that found using the lowest lying states.

1.4 Aims of this work

If the tensor force does produce a robust effect across the nuclear landscape, as suggested in Ref. [6], then it should describe equally well trends in single-particle energies for hole-states within the core as particle-states outside of it. The N=81 system provides a test of this statement. The isotones ^{137}Ba, ^{139}Ce, ^{141}Nd and ^{143}Sm can all be produced via traditional light-ion reactions, populating neutron-hole states inside the N=82 core. The high-ℓ orbitals in the N=50-82 shell, $g_{7/2}$ and $h_{11/2}$, both possess large radial overlaps with the $\pi g_{7/2}$ orbital, as illustrated in Fig 1.9. As the $\pi g_{7/2}$ fills with

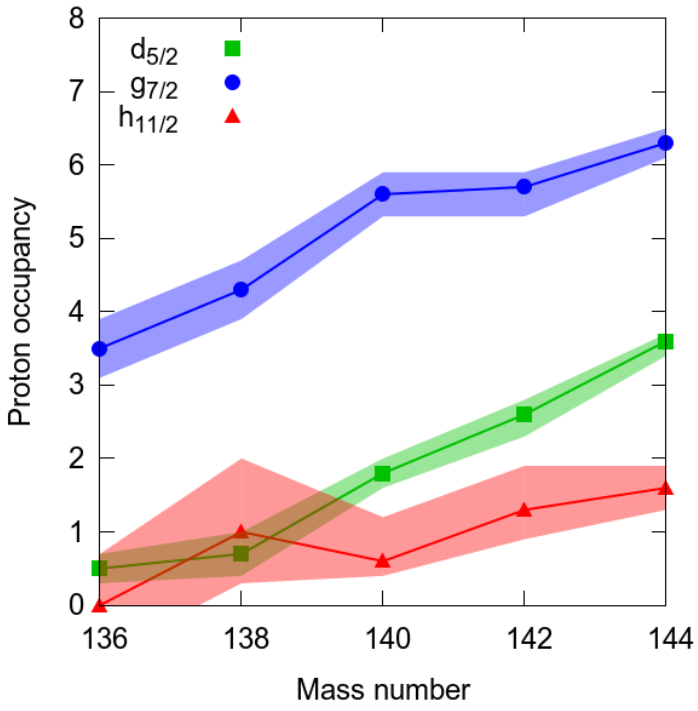

Figure 1.7: Occupancy of proton orbitals in the N=82 isotones, measured through single-proton transfer reactions [13]. The transparent bands represent the uncertainties on the measurements.

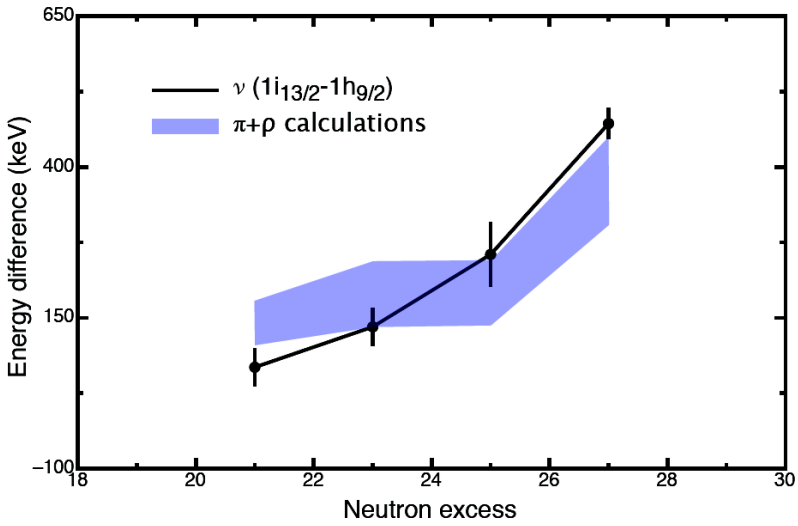

Figure 1.8: Separation of the energy centroids of the $i_{13/2}$ and $g_{9/2}$ neutron orbitals in the N=83 isotones. The shaded region represents the calculated value including a tensor force. The range of the region is due to uncertainties in proton occupancies. Figure from Ref. [12].

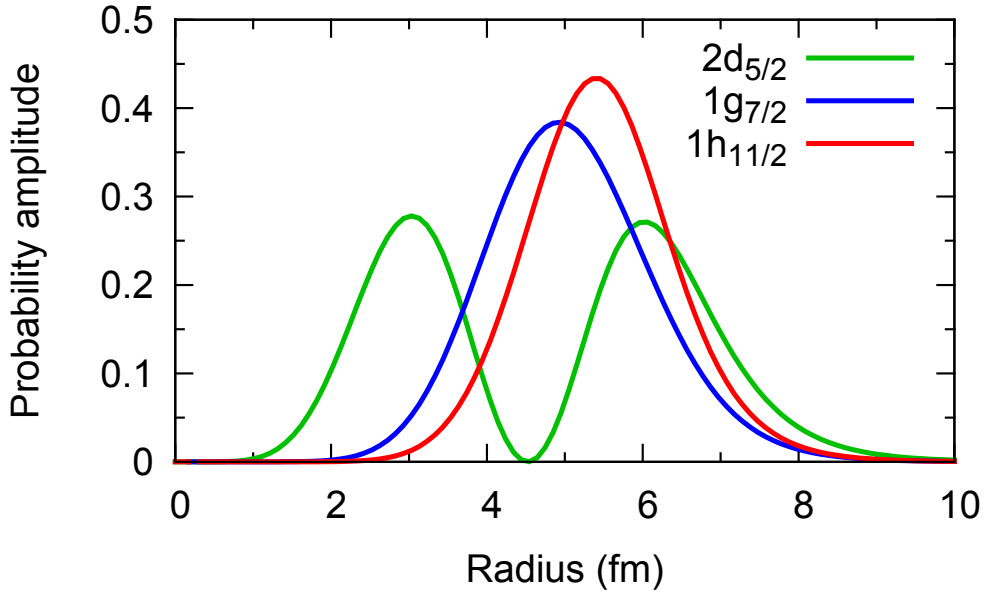

Figure 1.9: Radial probability amplitudes for the $2d_{5/2}$, $1g_{7/2}$ and $1h_{11/2}$ orbitals.

protons (see Fig. 1.7) the $\nu g_{7/2}$ and $\nu h_{11/2}$ should experience an increasingly strong tensor force. Using the arguments in Fig. 1.4, this should be repulsive for $\nu g_{7/2}$ and attractive for $\nu h_{11/2}$. Since the central force should affect both similarly, due to their similar radial overlaps, the tensor force should manifest itself as a relative splitting of the single-particle energies.

The current single-particle knowledge of the N=81 isotones is provided by a number of independent measurements, made using the (p,d), (d,p) and (^{3}He,α) reactions [14–20]. These data indicate that the fragmentation of single-particle strength is more severe than that observed in the Sb or N=83 systems, with $\sim$ thirty states associated with the five N=50-82 shell orbitals in each isotope. In the case of the $d_{5/2}$ and $g_{7/2}$ orbitals, it is further found that the majority of strength is in high-lying fragments, and so the lowest lying states of correct spin-parity can not be assumed to provide a realistic indication of trends.

The states populated in transfer reactions depend strongly on the reaction kinematics, as will be discussed in Chapter 2; the (p,d) and (d,t) reactions favour the population of low-ℓ states and (^{3}He,α) the population

of high-ℓ states. Both sets of data are required in order to obtain a complete description of the single-particle behaviour. Furthermore, due to the degree of fragmentation it is clear that for accurate centroids to be measured, consistent spectroscopic data are required.

The disparate measurements made to date do not provide the level of consistency required for such measurements. Differences in the experimental methods alone will result in systematic errors between the data sets. More significant are differences in the analyses carried out to extract the spectroscopic information, the results of which are impossible to verify due to the lack of published cross section data. The effect of these inconsistencies between experiments is well illustrated by the variation in the reported strength carried by the lowest lying $7/2^+$ states across the isotones. These are seen to vary between $\sim 15\%$ and 40%, with the data not even available for ^{137}Ba.

The aim of this work is to carry out a single set of measurements, using both the (p,d) and (^{3}He,α) reactions, with consistent experimental technique and analyses. This approach minimises the systematic error introduced and provides an accurate set of relative measurements which may then be used for further study of the role of the tensor force in the evolution of nuclear structure.

CHAPTER

TWO

DIRECT REACTIONS

Direct nuclear reactions are powerful tools for probing nuclear structure. They are one-step processes occurring via a single degree of freedom. This is in contrast to compound reactions which involve many different degrees of freedom and occur via a sequence of multiple steps. The chances of multistep processes are greatly increased for impact parameters less than the nuclear radius, and as a result direct reactions occur primarily at the nuclear surface.

Within the approximation of first-order perturbation theory, the probability of a direct reaction occurring can be described by Fermi's Golden Rule

$$\lambda = \frac{2\pi}{\hbar}|V_{\beta\alpha}|^2\rho(E_k), \tag{2.1}$$

where $\rho(E_k)$ is the density of final states and $V_{\beta\alpha}$ the matrix element of the interaction linking the initial and final systems:

$$V_{\beta\alpha} = \langle \Psi_\beta \mid V \mid \Psi_\alpha \rangle. \tag{2.2}$$

Here α refers to an initial partition of target nucleus A and projectile a, and β a final partition of target-like recoil B and ejectile b. The reaction itself is written in the form A(a,b)B. For the purposes of this discussion, the wave functions Ψ are decomposed into a wave component describing the relative

motion of the nuclei χ, and a component describing their internal structure Φ.

By applying the golden rule to a reaction scenario (see Ref. [21] for example), it can be shown that the differential reaction cross section is

$$\left(\frac{d\sigma}{d\Omega}\right)_{\beta\alpha} = \frac{m_\alpha m_\beta}{(2\pi\hbar^2)^2}\frac{k_\beta}{k_\alpha}|V_{\beta\alpha}|^2, \tag{2.3}$$

where m_i are reduced masses and k_i are wave numbers. This is an observable quantity and the details of making such measurements are discussed in Chapter 3.

As the reaction rate is dependent on a matrix element (Eqn. 2.2), direct reactions allow a high degree of selectivity in the populated reaction channels since a given interaction operator will only connect strongly through particular initial and final states. The study of single-particle structure using single-nucleon transfer is an excellent example of this. States in the recoil nucleus which resemble the initial nucleus plus the transferred nucleon result in a large matrix element in Eqn. 2.2, and therefore a high cross section for population. This is quantified by the spectroscopic factor which describes how single-particle in nature the state transferred to is. The extraction of spectroscopic data forms a key part of transfer-reaction studies. Additional information on the nature of the state populated is provided by the angular distribution of reaction cross sections. These have characteristic shapes dependent on the orbital angular-momentum transfer which takes place, and are discussed in more detail below.

Two transfer reactions were used in this work, (p,d) and (^{3}He,α), both of which proceed via the removal of a single neutron from the target nucleus. Before discussing the specifics of these reactions, a formalism for their description is introduced.

2.1 Modelling direct reactions

Early models of direct reactions adopted a plane-wave approximation for the relative motion χ to simplify the problem [22]. In making this approximation, the interactions between scattering nucleons are being ignored. This approach yields some valuable insights, including a qualitative description of the observed link between ejectile distribution and transferred angular momentum. The reaction amplitude, however, is poorly reproduced, limiting the spectroscopic information obtainable [23].

The distorted-wave Born approximation (DWBA) replaces the aforementioned plane-waves with distorted-waves, generated by the realistic potentials between reaction partners in the entrance and exit channel before and after the reaction occurs. The result is a more robust framework for the description of direct reactions. In the following section the distorting potential, referred to as the optical potential, is introduced. The role it plays within the DWBA is discussed later.

The optical potential

The potential between interacting nuclei is complex, arising from many-body interactions. This problem is reduced using the concept of an average potential, analogous to the mean-field potential introduced in the shell model. The dominant process during low-energy nuclear bombardment is elastic scattering. With reference to Eqn. 2.2, this is understandable given the similarity between initial and final states. The optical potential is therefore chosen so that it accurately describes behaviour in this channel.

The potential must clearly possess a Coulomb term, to describe the electrostatic interaction between nuclei, in addition to a nuclear term, describing scattering due to the strong interaction. The latter term is typically parametrised using a Woods-Saxon form such that it approximates the nuclear matter distribution. In the region of the nuclear surface, the spin-orbit interaction becomes important. This vanishes in the nuclear interior, where

the matter distribution becomes uniform, and so a differential form of the Woods-Saxon potential is used for its parametrisation.

These three contributions to the potential are all real functions and therefore conserve the total flux in the incoming and outgoing elastic channels. To account for scattering to non-elastic channels an imaginary, absorptive term is required. In practice two such terms are included, one describing absorption in the nuclear volume and the other absorption at the nuclear surface. Again these are chosen to have the form of a Woods-Saxon well and its derivative, respectively.

The parametrisation described above is written formally as [24]

$$\begin{aligned} U_{OM}(r) =& V_c - V_0 f(x_0) + \left(\frac{\hbar}{m_\pi c}\right)^2 V_{SO}(\boldsymbol{\sigma}\cdot\boldsymbol{\ell})\frac{1}{r}\frac{d}{dr}f(x_{SO}) \\ & - i\left[W f(x_w) - 4W_D\frac{d}{dx_D}f(x_D)\right], \end{aligned} \tag{2.4}$$

where $f(x_i)$ are Woods-Saxon potentials

$$f(x_i) = \left[1 + \exp\left(\frac{r - r_i A^{1/3}}{a_i}\right)\right]^{-1}. \tag{2.5}$$

In Eqn. 2.4 V_c is the electrostatic potential, which is simply a Coulomb potential outside the nuclear volume, and V_0 and V_{SO} the strengths of the nuclear volume and spin-orbit potentials, respectively. Together they describe the real part of the optical potential. W and W_D are the strengths of the imaginary volume and surface potentials, respectively. The individual contributions of these terms to the optical potential are illustrated in Fig. 2.1.

The parameters in U_{OM} are found by fitting the various parameters to the results of elastic scattering experiments. It has been common practice in the past for elastic scattering data to be collected from only the target used for transfer, and the optical potential determined from that alone. This

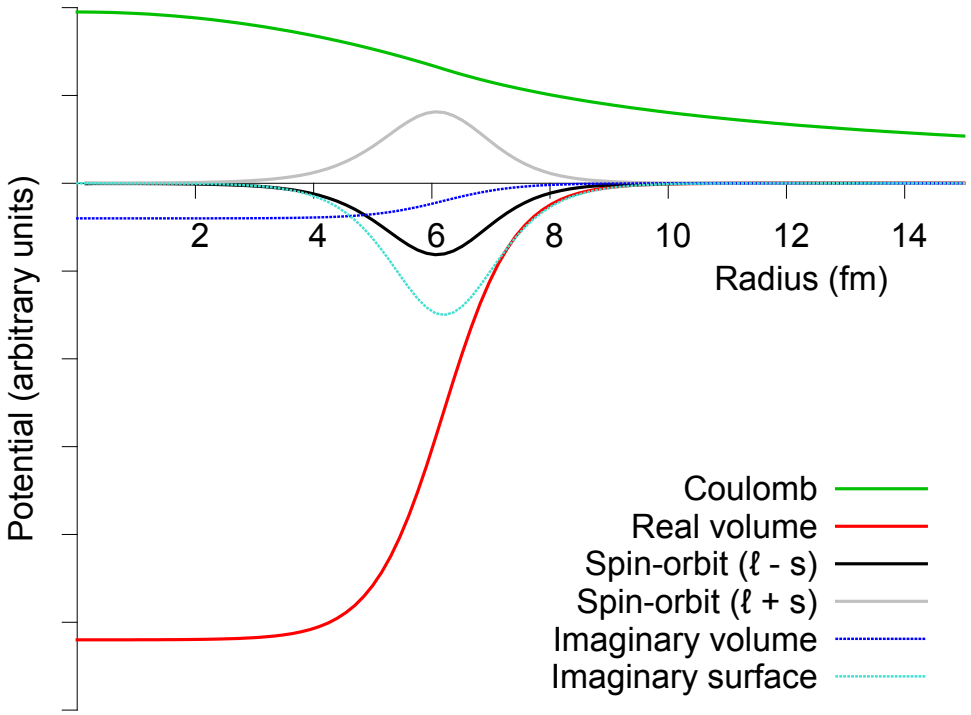

Figure 2.1: The form of the individual terms in Eqn. 2.4. This is only an illustrative picture since the amplitudes of the various terms are partition dependent. The spin-orbit interaction is dependent on the coupling of orbital and intrinsic angular momenta.

approach is perhaps ill-advised, since it introduces the danger of falling into local χ^2 minima. As an alternative, phenomenological global parameters are available, fitted for data sets spanning regions of mass and energy. These permit the study of nuclei in partitions lacking detailed scattering data. They are themselves not without risk, however, since if their applicable range is stretched too far they are likely to lose accuracy on a localised level due to an over-smoothing of parameters. Somewhere between these two extremes exists a happy medium, with potentials fitted over a sufficient range to ensure the various parameters are well constrained, but still valid for all nuclei considered.

There are some general properties of optical potentials worthy of brief mention:

- The depth of the real potential, V_0, is found to be $\sim$ 50 MeV per nucleon at low energies. At higher energies the short-range repulsive component of the nuclear force decreases this depth.

- The spin-orbit term leads to an asymmetry in the scattering depending upon the spin-projection of the projectile. This gives rise to spin-polarisation in the outgoing channel, which differentiates ℓ+s and ℓ-s states.

- The relative contribution of the imaginary terms is energy dependent. At low bombardment energies the volume contribution is small; inelastic scattering within the nuclear volume is inhibited by the Pauli exclusion principle and absorption occurs only at the nuclear surface. At higher projectile energies inelastic channels open up within the nuclear interior and the volume term becomes dominant.

The DWBA

Derivations of the DWBA can be found in References [21, 23, 25], amongst others. Presented here is a brief summary of the procedure highlighting the important concepts. The notation used here is consistent with that in Reference [23].

The (p,d) reaction will be used as an example during this discussion. An illustrative diagram of this reaction is in Fig. 2.2. A description of the (^{3}He,α) reaction requires only minor modification of that for (p,d). The process to be described can be considered as three distinct stages. We start with two nuclei scattering elastically in a potential described by the optical model. A nucleon is then transferred directly between bound states of the beam and target through a weak interaction. Finally, we return to elastically scattering nuclei, although in a different partition to the initial system.

If the interaction inducing the transition between reaction channels is weak relative to elastic scattering, it may be treated as a perturbation on it. Interactions not satisfying this criteria require an approach other then the

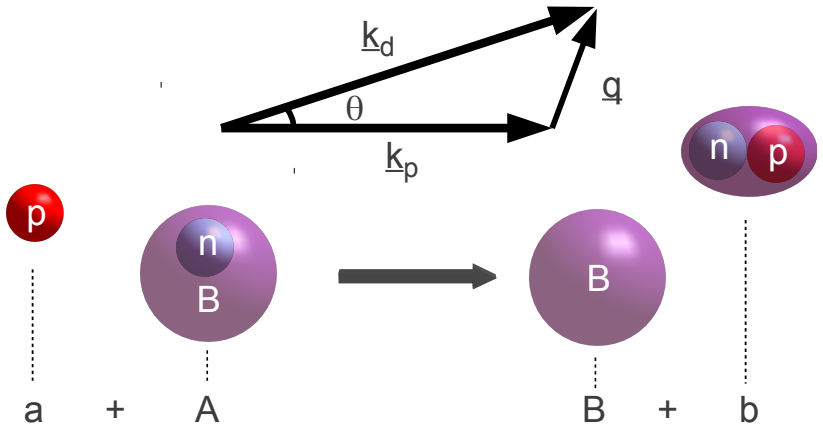

Figure 2.2: An illustrative diagram of the (p,d) reaction. The vector coupling of the incoming and outgoing waves is shown in the upper portion. The target nucleon A is composed of a core B plus transferred neutron. Likewise, the ejectile b is a proton plus the transferred neutron.

DWBA, for example the coupled-channel formalism [23]. A Hamiltonian for the initial partition in Fig. 2.2 can be written

$$\hat{H}_\alpha = \hat{H}_p + \hat{H}_A + T_\alpha + V_\alpha, \tag{2.6}$$

where H_p and H_A refer to internal structure only , T_α is the kinetic energy of the center of mass and V_α is the potential between nuclei. An equivalent relation can be written for any other partition (including also the projectile internal structure if required).

In the DWBA the realistic nuclear potential V_α is replaced by the optical potential U_α plus the perturbing potential W. With reference to Fig. 2.2, we recognise that V_α may be expressed

$$V_\alpha = \sum_{\substack{i\in a \\ j\in A}} V_{ij} = V_{pn} + V_{pB}. \tag{2.7}$$

A general feature of optical potentials is that they exhibit smooth trends across neighbouring nuclei, hence the potential U_α is well approximated by V_{pB}. Through comparison we therefore obtain an estimate for the perturbing potential of $W = V_{pn}$. This result is substituted into Eqn. 2.2 to obtain the

matrix element:

$$V_{\beta\alpha} = \langle \Phi_B \Phi_d \chi_\beta \mid V_{pn} \mid \Phi_A \Phi_p \chi_\alpha \rangle. \tag{2.8}$$

The distorted waves χ_α and χ_β are solutions to the Schrödinger equation using the Hamiltonian given in Eqn. 2.6, and the equivalent for the final partition. In the case of elastic scattering the realistic nuclear interaction V is approximated by the optical model potential U to give

$$(\hat{H}_\alpha - T_\alpha - U_\alpha)\chi_\alpha = 0. \tag{2.9}$$

It is noted that whilst the resulting waves have the correct asymptotic form of plane waves, there is no guarantee that they should remain physical at small radii as well. Nonetheless, the approximation has been found to work remarkably well.

For single-nucleon transfer the nucleus A can be described as the recoil nucleus B plus a neutron in a shell-model state, $\phi_{n,j,l}$. A similar description can be applied to the ejectile b. The wave functions for these nuclei are then written, after expanding over all possible shell-model states, as

$$\begin{aligned} \Phi_A &= \sum_{n,j,\ell} \beta_{n,j,\ell} \phi_{n,j,\ell} \Phi_B, \\ \Phi_d &= \sum_{n',j',\ell'} \beta_{n',j',\ell'} \phi_{n',j',\ell'} \Phi_p, \end{aligned} \tag{2.10}$$

where the $\beta_{n,j,l}$ are the parentage coefficients. The physical meaning of these is discussed below.

The matrix element of Eqn. 2.9 is now written

$$V_{\beta\alpha} = \sum \beta_{j,\ell}\beta_{j',l'} \langle \Phi_B \Phi_p \phi_{j',\ell'} \chi_\beta(r_\beta) \mid V_{pn} \mid \Phi_B \Phi_p \phi_{j,\ell} \chi_\alpha(r_\alpha) \rangle. \tag{2.11}$$

As the reaction is a direct process the core nucleons are unchanged, hence their respective terms vanish from Eqn. 2.11. Furthermore, for reactions involving even-even nuclei, the summation over j and ℓ collapses to a single

term due to coupling with the 0^+ ground state. The differential cross section (Eqn. 2.3) can now be written

$$\left(\frac{d\sigma}{d\Omega}\right)_{\beta\alpha} = \beta^2_{n,j,l}\beta^2_{n',j',l'}\frac{m_\alpha m_\beta}{(2\pi\hbar^2)^2}\frac{k_\beta}{k_\alpha}\langle\phi_{n',j',l'}\chi_\beta(r_\beta) \mid V_{pn} \mid \phi_{n,j,l}\chi_\alpha(r_\alpha)\rangle^2. \quad (2.12)$$

The first two terms in Eqn. 2.12 are the spectroscopic factors for the target and projectile, respectively, whose meaning is discussed below. The remainder of the expression is the DWBA cross section; the expected cross section when both spectroscopic factors are unity. The entire expression is written more conveniently as

$$\frac{d\sigma}{d\Omega} = S^t_{n,j,\ell}S^p_{n',j',\ell'}\left(\frac{d\sigma}{d\Omega}\right)_{DWBA}. \quad (2.13)$$

The calculation of the DWBA cross section is typically performed using computer codes. Early versions of these used a zero-range approximation for the radial dependence, with the scattering interaction replaced by a delta function. Gains in computing power have reduced the need for this approximation and all calculations in this work were performed using the finite-range code PTOLEMY [26].

Spectroscopic sum rules

The spectroscopic factors which appear in Eqn. 2.13 provide a measure of how single-particle in nature the bound state of the transferred nucleon is in the ejectile and target systems. In an idealised shell-model picture these would be pure single-particle states with spectroscopic factors of unity. As discussed in Chapter 1, however, the effect of residual interactions is to mix different nuclear configurations, thereby fragmenting the single-particle strength over multiple states.

The total spectroscopic strengths associated with shell-model orbitals are described by so-called sum rules [27]. For nucleon removal this sum relates to the total occupancy of the orbital, and for nucleon adding the total vacancy.

In reactions involving closed-shell nuclei, sum rules provide a check of the fraction of single-particle strength observed. In the case of nucleon removal from a fully-occupied orbital, the summed spectroscopic strength becomes

$$\sum_i S_{n,l,j,i} = 2j + 1, \tag{2.14}$$

where i runs over all states containing strength from the single-particle orbit described by the quantum numbers n, j, l.

2.2 Experimental considerations

The extraction of robust spectroscopic factors requires suitable reaction conditions. These include the reaction constituents, the projectile energy and the angles at which cross sections are measured. In general it is desirable to maximise the DWBA cross section as calculations reproduce more reliably strong channels. From a purely experimental perspective, this approach also provides increased statistics in the collected data.

Momentum matching

An appreciation for good conditions can be gained through consideration of the angular-momentum transfer taking place. In the classical limit this is

$$\Delta\ell = R \times q, \tag{2.15}$$

where R is the nuclear radius and q the momentum carried by the transferred nucleon.

As shown in Fig. 2.2, the value of q is determined by the linear momentum in the initial and final channels, and also the angle of ejectile emission, θ. This suggests that for large ℓ, a large momentum mismatch between the initial and final channels or large θ is required. The Q values for the (p,d) and (^{3}He,α) reactions on the N=82 isotones are $\sim$ -7 and +11 MeV, respectively.

Eqn. 2.15 gives estimates of the transferred angular momentum of $\sim 1\ \hbar$ in (p,d) and $\sim 5\ \hbar$ in (^{3}He,α).

Reactions in (p,d) requiring large ℓ will probe the tails of nuclear wave functions at large radii. These carry only a small fraction of the amplitude, resulting in low interaction probabilities, and are less well described by the phenomenological potentials typically employed. Conversely, the population of states with small ℓ in (^{3}He,α) will probe the nucleus at small radii. Non-direct channels are expected to dominate here, with additional reaction cross section being generated through multi-step processes. These are not accounted for in DWBA calculations, hence reduce the validity of the output.

With reference to the single-particle states in the $N = 50$ - 82 shell (see Fig. 1.2), the (p,d) reaction should provide a good description of states carrying $s_{1/2}$, $d_{3/2}$ and $d_{5/2}$ strength, whilst the (^{3}He,α) reaction is better matched for states carrying $g_{7/2}$ and $h_{11/2}$ strength. An overlay of data from both reactions used is shown in Fig. 2.3 and the states labelled with the ℓ-transfer involved. It is clearly observed that low ℓ-transfer is favoured in (p,d) and high ℓ-transfer in (^{3}He,α).

Energy dependence

Nuclei must overcome a Coulomb barrier in order to interact, resulting in a strong energy dependence of the cross section at low projectile energies. At energies just above the Coulomb barrier cross sections rise rapidly. This dependence is reduced at higher energy. Calculations of the cross sections for the (p,d) and (^{3}He,α) reactions on $N = 82$ nuclei are shown in Fig. 2.4.

In addition to the reaction cross section obtained at a given energy, the quality of the collected spectra must be considered. This is discussed in Chapter 3, but in summary the attainable excitation-energy resolution of the recoiling nucleus (the $N = 81$ isotone in this case) decreases with increasing projectile energy. A compromise is therefore required when selecting the beam energy. For this work the minimum beam energy capable of providing

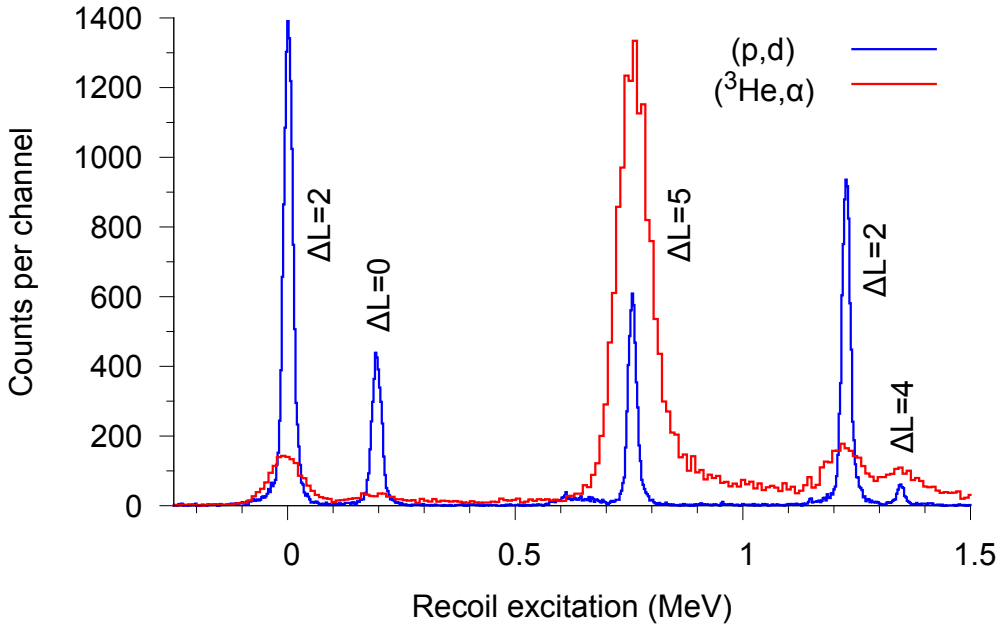

Figure 2.3: Data showing the relative population of states involving different angular momentum transfer in the single-neutron removal reactions (p,d) and (^{3}He,α) on ^{142}Nd at 23 and 34 MeV, respectively.

sufficient statistics within the available time was used.

To allow for robust spectroscopic factors to be extracted, and also to discriminate different ℓ, measurements at multiple angles in each reaction are required. The selection of these are discussed below, with each measurement linked to population of a specific single-particle state. The definition of sufficient statistics, whilst clearly subjective, was here selected as an expectation of 1000 counts in a 10 % fragment of that single-particle strength. The beam energies selected were 23 MeV for protons and 34 MeV for ^{3}He.

Angular distributions

With reference to Fig 2.3, the relative cross section between the two reactions provides some discrimination between the different ℓ involved. Further discrimination is provided by the characteristic angular distributions produced. DWBA calculations are plotted in Fig. 2.5, showing the expected form of these.

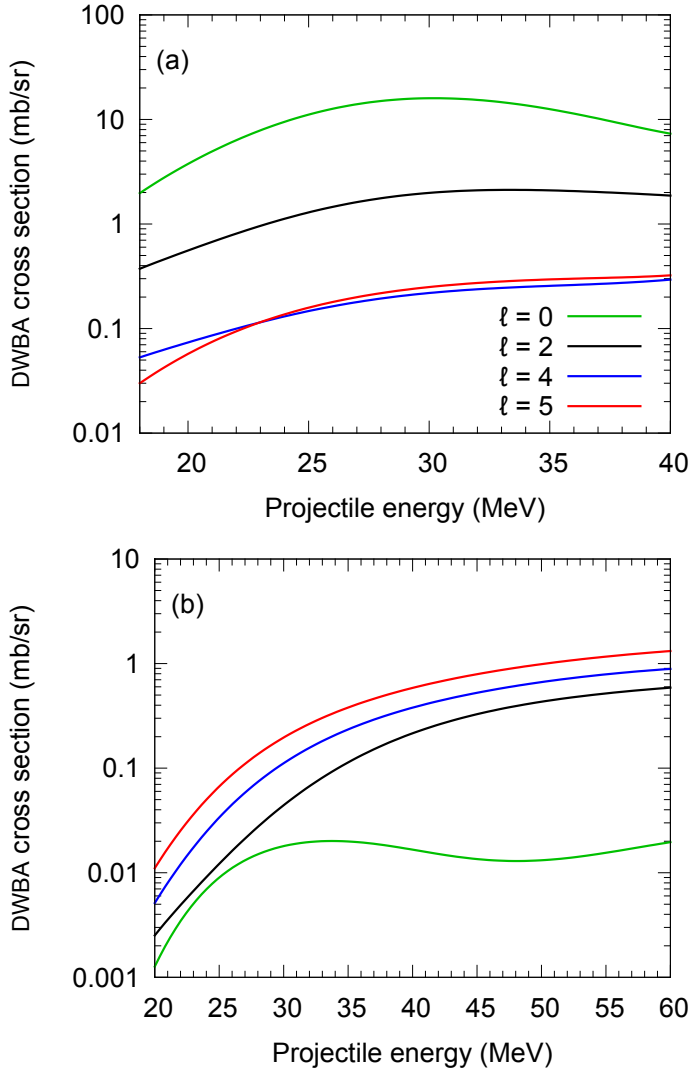

Figure 2.4: DWBA calculations of reaction cross sections, in the lab frame, at $\theta_{lab} = 5°$ for (a) (p,d) and (b) (^{3}He,α) on $N = 82$ isotones as a function of projectile energy.

The distributions shown in Fig. 2.5 have first maxima whose angular positions increase with ℓ, although this is a more subtle effect in (^{3}He,α) with the extent of the first maxima moving out. Returning to Eqn. 2.15, this is a consequence of the relation between q and θ, illustrated in Fig. 2.2. Using the same arguments as invoked earlier, these maxima should correspond to the most reliable DWBA output.

For the (p,d) reaction these peak angles vary with recoil excitation, but angles of 5°, 20°, 35° and 42° are found to be reasonable approximations for

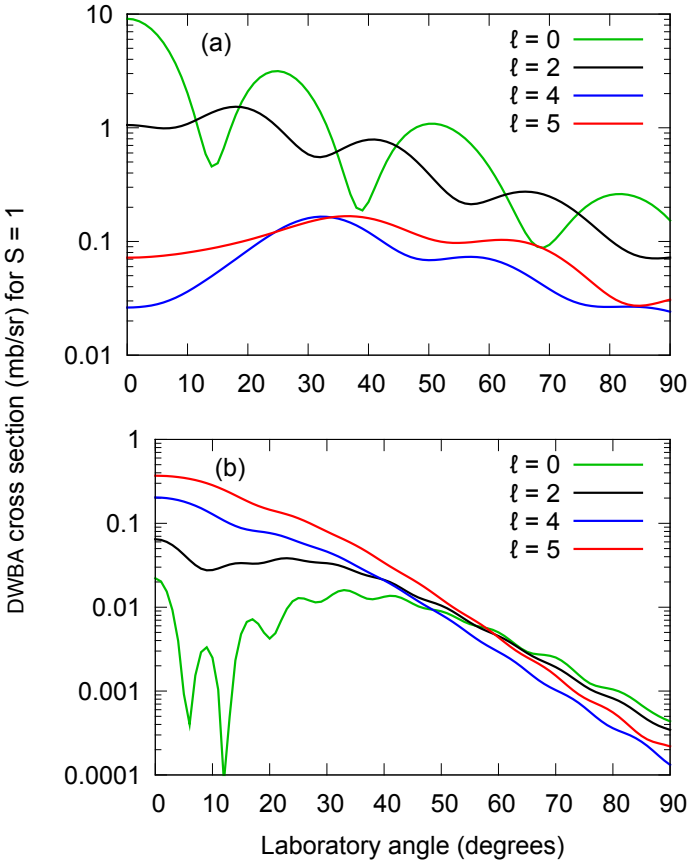

Figure 2.5: DWBA calculations for transfer involving different ℓ in (a) (p,d) at 23 MeV and (b) (^{3}He,α) at 34 MeV.

transfer of 0, 2, 4 and 5 units of angular momentum, respectively (the $\ell = 0$ distribution actually peaks at 0°, however experimental limitations prevent a measurement at $\theta < 5°$). In addition, comparisons between these angles provide good discrimination between the different ℓ.

For (^{3}He,α) the distributions are less distinct and all are forward peaked. Good distinction between low and high ℓ is provided between reactions and so the primary interest in measuring at multiple angles in this case is to distinguish $\ell = 4$ and $\ell = 5$ transfer. A quantity defining the discriminating power between these transfers is defined as

$$D_{xy} = \frac{(\theta_x/\theta_y)_{\ell=5}}{(\theta_x/\theta_y)_{\ell=4}}, \tag{2.16}$$

where θ_i is the differential cross section at laboratory angle i. D_{xy} thus describes the difference in ratios expected between the measured cross sections at any two angles. The matrix defined by Eqn. 2.16 is in Fig. 2.6. It can be seen that good discrimination is obtained between angles of 5° and 15°, these being the angles chosen. Greater discrimination is seen using $\sim 35°$ instead of 5°, but this is offset by a large drop in cross section.

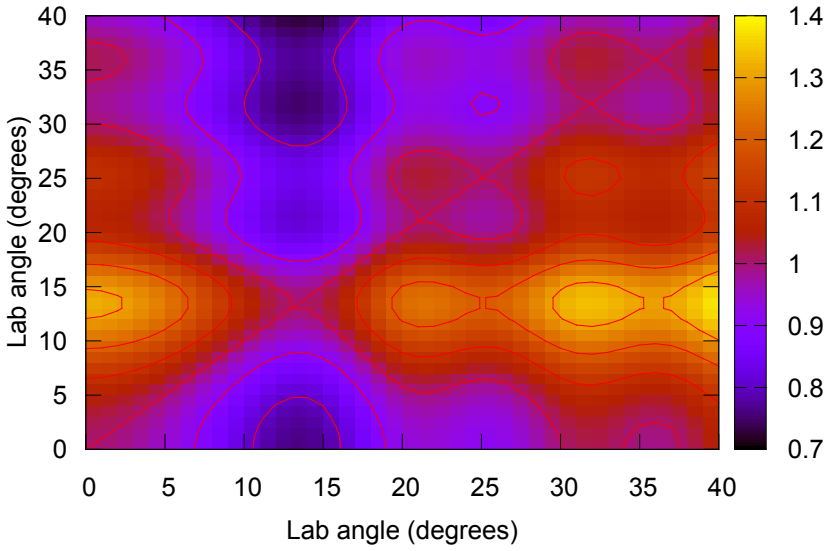

Figure 2.6: Matrix illustrating the discriminating power between $\ell = 4$ and $\ell = 5$ states in (^{3}He,α). See Eqn. 2.16 and the text for details.

CHAPTER

THREE

EXPERIMENTAL SETUP

The data that form the basis of this work were collected at the A.W. Wright Nuclear Structure Laboratory (WNSL), at Yale University, in two separate experiments. The experimental setup and methodology were identical for both and are described in this chapter. In both experiments single-neutron removal reactions were used to populate states in the N=81 isotones ^{137}Ba, ^{139}Ce, ^{141}Nd and ^{143}Sm.

In the first experiment the (^{3}He,α) reaction was used at a beam energy of 34 MeV, with cross sections measured at laboratory angles of 5° and 15°. An extra measurement at 10° was made for ^{137}Ba, as no previous (^{3}He,α) data exist for this isotone.

Additional data were collected in the second experiment, using the (p,d) reaction at 23 MeV, with cross sections measured at laboratory angles of 5°, 20°, 35° and 42°. The angles chosen here match peaks in the angular distributions corresponding to different ℓ transfer, as discussed in Chapter 2.

The outgoing light ejectiles from these reactions were momentum-analysed using an Enge split-pole spectrograph and detected at the focal-plane using a position-sensitive ionisation chamber, backed by a plastic scintillator. The ejectiles were identified using their differential energy-loss within these detectors.

3.1 Beam production

The p and ^{3}He beams required for this work were provided by the Yale ESTU tandem accelerator. This is an upgrade of the MP-1 tandem at WNSL and is capable of achieving terminal voltages of up to 22 MV (for further details see Ref. [28, 29]).

The accelerator requires that ions are injected into the machine with negative charge. For species capable of forming solid compounds, this is typically achieved using a sputter source. The H^- ions were formed by the bombardment of TiH_2 powder with Cs ions and the sputtered H^- ions extracted using an electric potential applied across the source. The He^- ions were formed using a duoplasmatron charge-exchange source; He^+ ions formed in the plasma were accelerated through a lithium vapour resulting in charge exchange and the production of He^- ions.

The sources were mounted on a high-voltage platform, held at +300 kV, pre-accelerating ions to 300 keV upon their exit. The ions are then passed through an injector, including a 90° inflector magnet with mass resolution$\sim$ 1/240. This is sufficient to ensure isotopically pure beams of the light species used here. Further details on ion sources may be found in, for example, Ref. [30].

A plan of the laboratory at WNSL, including a simple schematic diagram of the Yale tandem accelerator, is shown in Fig. 3.1. The negative ions enter the tandem from the left as shown, and are accelerated towards the high-voltage terminal. At the terminal the ions are passed through a thin, carbon stripper foil, losing electrons in the process, resulting in a positively-charged beam. They are then further accelerated away from the terminal towards ground potential. The energy of ions exiting the tandem is given by

$$E = E_S + (q+1)eV, \tag{3.1}$$

where E_S is the energy at which the ions are injected from the ion source, V is the terminal voltage and q is the ionic charge state after the stripper

foil. This assumes that there are no charge-exchanging collisions with residual gasses in the accelerator, which would result in a smearing of the ionic energy distribution.

The accelerated ion beam is passed through a dipole analyser magnet, which disperses ions according to their magnetic rigidity, p/q. For isotopically-pure beams, this selection is sensitive enough to transmit a single ionic charge state, resulting in a monoenergetic beam.

Beam stability is achieved by monitoring the beam current on image slits located after the analyser magnet. Fluctuations in the beam energy shift the trajectories of ions within the analyser, changing the beam current deposited on these slits. The image-slit currents are used to drive a feedback circuit which adjusts the tandem charging mechanism such that a constant terminal voltage is maintained. In practice a beam stability of $\sim 1/10^4$ is attainable, the contribution of which towards the final energy resolution in the experiment is negligible.

The beam is directed towards the required experimental station using two dipole switcher magnets. Before reaching the target the beam passes through three quadrupole magnets, used for focussing, separated by two dipole steerer magnets to ensure the beam remains on axis. Fine tuning of the beam focus is performed by monitoring the beam current measured on additional slits mounted in the beam pipe, and finally using a collimator at the target position and a Faraday cup as discussed later.

3.2 Targets

The targets used in this work are an important experimental consideration. Target thickness impacts on the rate of data collection as well as the spectral resolution. In addition, the composition of the targets must be taken into account due to competing reactions involving contaminant species.

The N=82 nuclei used as targets during this work were ^{138}Ba, ^{140}Ce, ^{142}Nd and ^{144}Sm. The targets all consisted of isotopically-enriched oxides

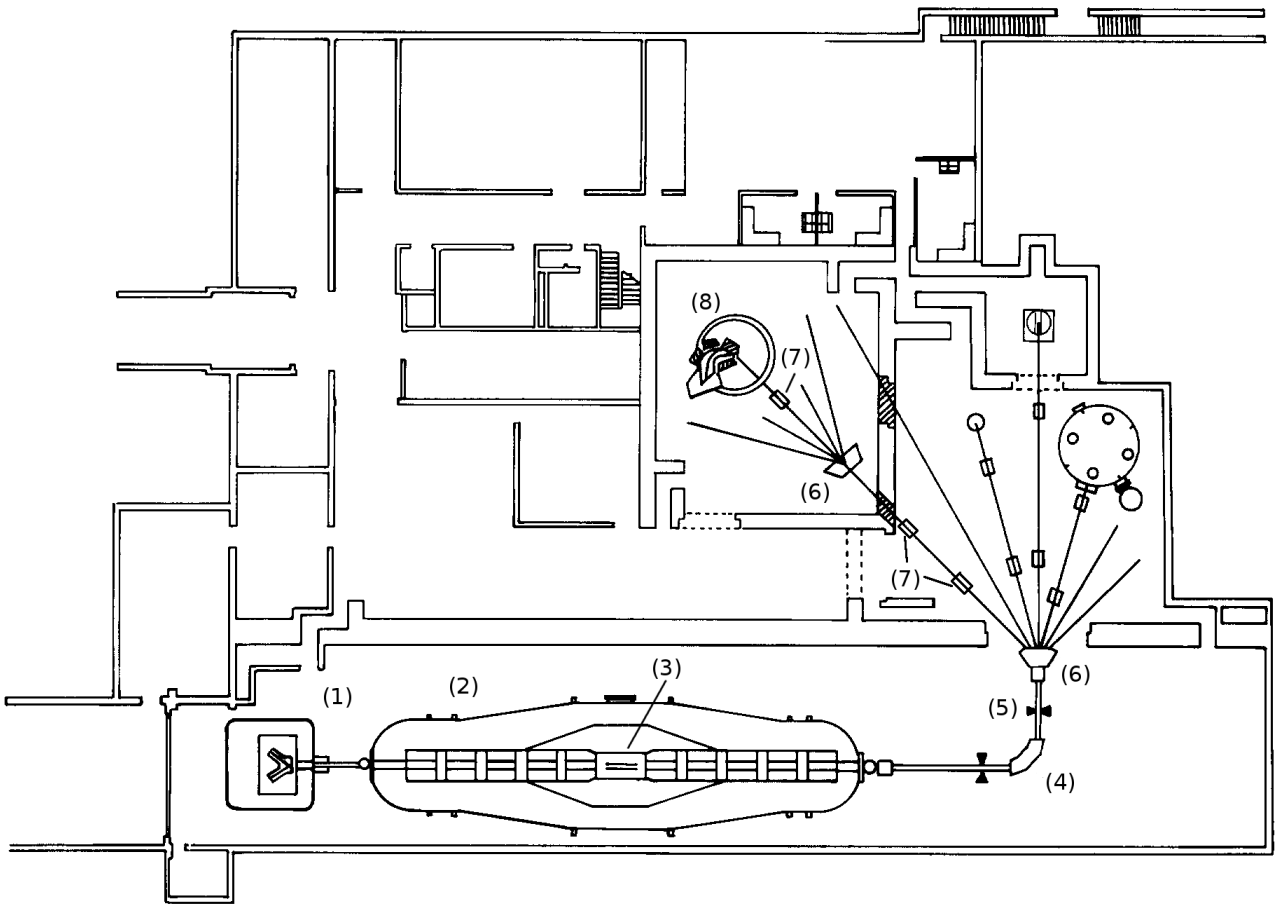

Figure 3.1: Plan of WNSL including a simple schematic of the tandem accelerator. 1) Ion source, 2) tandem, 3) high-voltage terminal, 4) analyser magnet, 5) image slits, 6) dipole switcher magnets, 7) quadrupole magnets, 8) Enge split-pole spectrograph. Figure modified from Ref. [28].

evaporated onto carbon backing foils for support and mounted in frames. Details of each target are presented in Table 3.1. The target thicknesses were measured using low-energy α-particle scattering, details of which are in Chapter 4.

Table 3.1: Details of the targets used during the 2009 experiment. Each target was mounted onto a carbon backing for support.

Target	Pre-evaporation composition	Thickness (μg cm^{-2})	Isotopic enrichment (%)
^{138}Ba	$BaCO_3$	101.3 (5)	99.8 (1)
^{140}Ce	CeO_2	144.8 (7)	99.9 (1)
^{142}Nd	Nd_2O_3	149.9 (6)	99.0 (1)
^{144}Sm	Sm_2O_3	41.6 (2)	93.8 (1)

The targets were mounted on a ladder within the scattering chamber. A schematic diagram is shown in Fig. 3.2. A "Faraday cup", formed from a strip of tantalum, was mounted behind the target ladder. This was connected to a Brookhaven current integrator (BCI) which provided a logic pulse for every 2×10^{-10} C of charge collected. This allows the total number of ions delivered on target to be measured.

To prevent the sputtering of electrons from the targets and Faraday cup, which would affect the measured beam current, a bias of +300 V was applied to both using separate batteries. The target chamber was held at ground potential.

A 2-mm diameter collimator was mounted on the target ladder. For a good beam tune, no current is measured at the collimator indicating a maximum beam spot diameter of 2 mm.

A 1.5-mm thick silicon surface-barrier detector was mounted at 30° to the beam axis. The rate of elastically scattered beam incident on this detector was monitored and its ratio to the delivered beam current recorded. A change in this ratio would give an indication of a change in target thickness. The variation observed during this work was $< 3\%$ for each target used.

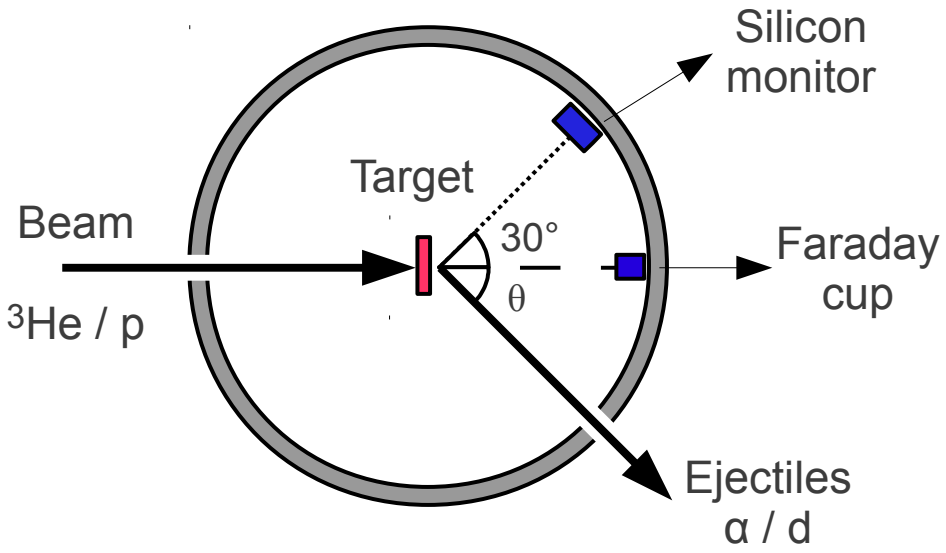

Figure 3.2: Schematic of the target chamber. A silicon surface-barrier detector is mounted at 30° to the beam axis and a Faraday cup positioned along the beam axis behind the target. A +300 V bias was applied to both the target ladder and Faraday cup in order to minimise electron sputtering. The entrance angle to the split-pole spectrograph, θ, may be adjusted.

3.3 Momentum analysis of outgoing ions

Given the beam energy provided by the tandem accelerator, and the masses of the nuclei involved, the Q-value of reactions taking place may be deduced from the energy and angle of ejectile emission. Defining the reaction as A(a,b)B, the relationship between reaction Q-value, ejectile energy and emission angle, θ, is written, non-relativistically, as [31]

$$Q = k_b T_b - k_a T_a - 2k_\theta (T_a T_b)^{\frac{1}{2}} \cos\theta, \tag{3.2}$$

where T is kinetic energy, M is mass and the constants k_i are given by

$$\begin{aligned} k_b &= 1 + \frac{M_b}{M_B}, \\ k_a &= 1 - \frac{M_a}{M_B}, \\ k_\theta &= \frac{(M_a M_b)^{\frac{1}{2}}}{M_B}. \end{aligned} \tag{3.3}$$

The correction to this from relativistic effects is of the order of 1 %, and is included in the later analysis.

Since all of the species involved in this work have well-determined masses, the reaction Q-value is directly related to the excitation of the recoil nucleus Ex_B,

$$\mathrm{Ex}_B = (M_a + M_A)c^2 - (M_b + M_B)c^2 - Q. \tag{3.4}$$

Thus an energy spectrum of the heavy nuclei populated is obtained through measurements of the energies and emission angles of outgoing light ejectiles.

Ion optics

A convenient method of measuring the ejectile momenta, and therefore their energy, is to use a magnetic spectrometer. Ions traversing the magnetic field will experience a force perpendicular to both their direction of motion and that of the field lines, as described by

$$\boldsymbol{F} = qe(\boldsymbol{v} \times \boldsymbol{B}), \tag{3.5}$$

where q is the ionic charge state, $\boldsymbol{v}$ is the ion velocity and $\boldsymbol{B}$ is the magnetic field. The ions will be deflected and, in the case of a field of uniform $\boldsymbol{B}$, follow a circular path along an axis parallel to the field lines. The radius of this path is described by the magnetic rigidity of the ion

$$B\rho = \frac{p}{qe}, \tag{3.6}$$

where p is the ion momentum and ρ the radius of curvature.

A simple magnetic spectrograph may be formed using a position-sensitive focal plane coupled with a magnetic field. It can be seen from Eqn. 3.6 that ions of different momenta will be spatially separated within the magnetic field by virtue of their differing curvatures. Their location on the focal plane will correspond to the reaction Q value, and therefore the state populated in the recoiling nucleus.

With reference to Eqn. 3.2, reactions of equal Q, but differing θ, will result in the emission of ejectiles of different energy. For a finite acceptance into the spectrometer, a broadening of peaks at the focal plane will be observed, this effect becoming more pronounced as the acceptance is widened. This is referred to as kinematic broadening and must be corrected for in order to allow for reasonable rates of data collection without degradation of the resulting spectra. This was achieved using a split-pole spectrograph, which is described below. Further detail on the general principles of magnetic spectrography may be found in, for example, Ref. [32].

The split-pole spectrograph

An Enge split-pole spectrograph was used to momentum analyse the outgoing ions, a schematic diagram of which is shown in Figure 3.3. The spectrograph consists of two pole pieces, each of which maintains a uniform magnetic field between its plates, encompassed by a single coil. In the regions between pole plates the motion of ions is as described by Eqn. 3.5.

Fringe-field effects occur at the entrance and exit of both pole pieces; the construction of the pole boundaries is such that these fields provide first-order vertical focussing. This allows the spectrometer to be operated with a vertical acceptance of up to ± 160 mr. Through the curvature and relative positioning of the two pole pieces, and adjustment of the focal-plane position, the split-pole spectrograph is capable of correcting for kinematic broadening, thereby achieving second-order horizontal focussing. Higher-order aberrations still remain however and these limit the maximum acceptance at which the spectrometer may be used.

The position along the central-beam axis, z, at which the reaction products are brought to a focus is given by the semi-empirical relation

$$z = 56.7k + 55.5, \tag{3.7}$$

as determined by [33]. Here k is a kinematic parameter given by

$$k = -\frac{1}{p}\frac{dp}{d\theta}, \tag{3.8}$$

where p is the ejectile momentum and θ the angle of emission with respect to the beam axis. An expression for k may be found by substituting $T_b \propto p^2$ into Eqn. 3.2 and differentiating with respect to θ:

$$k = \frac{(M_a M_b E_a/E_b)^{1/2}\sin\theta}{M_b + M_B(M_a M_b E_a/E_b)^{1/2}\cos\theta}. \tag{3.9}$$

The value of z returned by Eqn. 3.7 is used to position the focal plane. A more detailed description of the split-pole spectrograph may be found in [31].

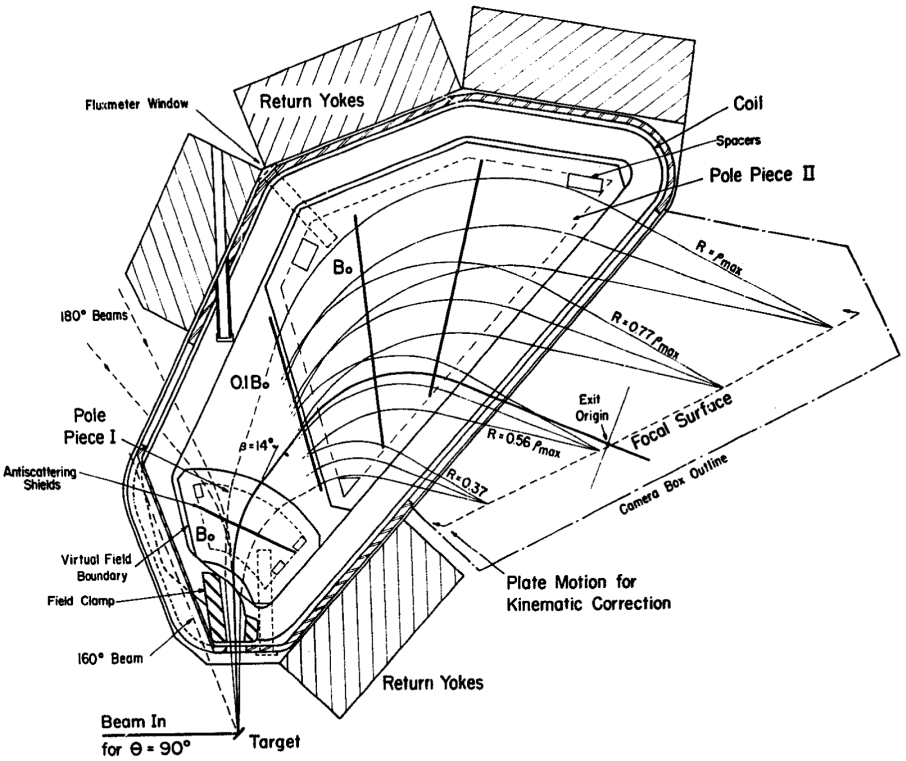

Figure 3.3: Schematic of an Enge split-pole spectrograph. At the entrance is an aperture with an acceptance of 2.8 msr. The focal plane position is set such that kinematic broadening is corrected. Figure from [32].

For this work an acceptance solid angle of 2.8 msr was used, previous tests having indicated that this results in optimal focal-plane resolution [34]. This

acceptance was set using two adjustable slits at the spectrometer entrance. The horizontal acceptance was set to be ±20 mrad and the vertical acceptance ±40 mrad. The larger vertical acceptance is acceptable since good focussing in the vertical plane is not required.

The design specifications of the Yale split-pole spectrograph are given in Table 3.2. Of particular interest is the resolving power which defines the fractional change in ion rigidity required to be able to distinguish states. To first order, the resolving power is defined as

$$R_1 = \frac{P}{\Delta P}, \tag{3.10}$$

where P is the ion momentum and ΔP is the resulting width of momentum spread. In practice, the quoted value for resolving power in Table 3.2 is only obtainable given an idealised focal-plane detector where position resolution does not contribute to overall momentum resolution. The actual value measured during this work was ~ 1000.

Table 3.2: Properties of the Yale split-pole spectrograph [34].

Property	Value
Orbital radius	$45 < \rho < 92$ cm
Resolving power	4290
Dispersion	1.96
Maximum B	16.3 kG

As the beam energy is increased the fractional shift in momentum corresponding to the population of neighbouring states in the recoil nucleus reduces. This results in a decrease in excitation-energy resolution at the focal plane.

The maximum field attainable in the spectrometer and the range of orbits allowed, as given in Table 3.2, dictate the maximum rigidity of ejectiles which may be transported to the focal plane. For the beam energies used here, field strengths of 9.70 and 12.59 kG were required for the (p,d) and (^{3}He,α) reactions respectively, both of which are comfortably inside these limits.

Contaminant species

The presence of contaminants in the target must be considered in terms of the rigidities of ejectiles resulting from reactions on them. If these rigidities are similar to those resulting from reactions on N=82 nuclei then they may obscure states of interest. With reference to Eqn. 3.9, the rate of change of p with θ increases as the contaminant mass decreases. Therefore shifting the angle at which the spectrometer is positioned will move contaminant states relative to those in the N=81 nuclei.

In addition, ions resulting from reactions on contaminant species of different mass will be brought to foci at different distances along the optic axis (see Eqn. 3.7). Under conditions for optimal focussing for the reactions of interest, ion groups from lighter species in the target will result in broader peaks at the focal plane. Broadened peaks that shift with angle relative to the states of interest are indicative of light contaminants within the target.

As the targets are manufactured from oxide material and mounted on carbon foils, the major contaminants will be carbon and oxygen. Calculations for the ejectile rigidity as a function of laboratory angle for the (p,d) and (^{3}He,α) reactions at 23 and 40 MeV, respectively, are shown in Fig. 3.4. The region of interest for this work corresponds to the range of rigidities between a maximum for the population of the ground state in ^{137}Ba through to a minimum for populating a 4 MeV state in ^{143}Sm.

With reference to Fig. 3.4, the primary contaminants of ^{12}C and ^{16}O are not expected to obscure any states of interest since the rigidities of the outgoing ions are too low. The expected presence of ^{13}C, which has 1.2 % natural abundance, will result in ions corresponding to the population of the ground and first excited (4.4 MeV) states in ^{12}C which do cross the region of interest in both reactions. The contaminant peaks produced will occur below 2 MeV in the N=81 excitation spectra produced, and so in a region of low level density. In addition they will shift sufficiently between angles that no individual peak will be affected by their presence at more than one angle.

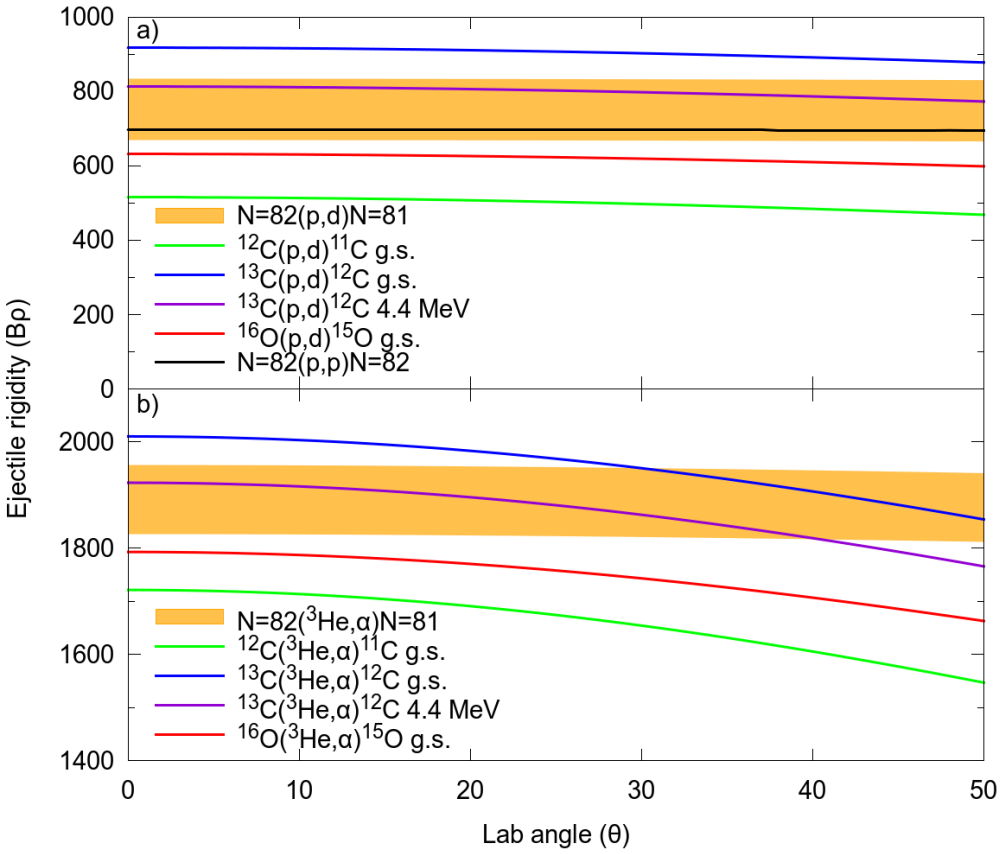

Figure 3.4: Ejectile rigidities as a function of laboratory angle, θ for a) (p,d) at 23 MeV, b) (^{3}He,α) at 34 MeV. The shaded region corresponds to the range of rigidities expected between populating the ground state of ^{137}Ba to populating a 4 MeV state in ^{143}Sm.

A more serious limitation is imposed for the (p,d) reaction due to elastically-scattered protons. The strength of this group is sufficient to mask all states in ^{143}Sm above 3 MeV in excitation. Therefore states above 3 MeV in ^{143}Sm were only observed in the (^{3}He,α) reaction. The impact of this is discussed in Chapter 4.

3.4 The focal-plane detector

The focal-plane assembly consists of a position-sensitive ionisation chamber (IC) and a plastic scintillator detector. The entire assembly moves freely along the optic axis and so may be positioned at the focal point, as given by Eqn. 3.7.

The IC provides position measurements for ions reaching the focal plane and, with the dispersion provided by the split-pole, the required measure of ejectile rigidity. It also provides a partial energy-loss measurement, with ions depositing their remaining energy in the scintillator. The combination of these two energy-loss measurements enables the separation of ion species traversing the assembly.

A blocker plate that may be moved across the the focal plane is also available. It is used to mask unwanted ion groups from the focal plane, reducing the rate in the detector thus minimising dead time and signal degradation due to pulse pile-up. A schematic diagram of the focal plane assembly is shown in Fig. 3.5.

Position-sensitive ionisation chamber

Ions enter and leave the IC through aluminised Mylar windows, of 0.25 mm thickness, located at the front and rear of the detector. Within the chamber there is a constant through-flow of isobutane gas at a pressure of 150 Torr. The ions traverse a region of uniform electric field, created by applying a 700-V potential difference between the cathode and Frisch grid. The uniformity of this field is maintained by ten evenly-spaced field-shaping wires connecting the cathode and Frisch grid through a chain of 10-MΩ resistors. Free electrons, resulting from ionisation of the gas, drift under the influence of this field towards the Frisch grid.

Two position-sensitive detectors running along the width of the IC sit above the Frisch grid. Photographs of the detectors are shown in Fig. 3.6. One of these is centred along the focal plane (the front wire), and the other

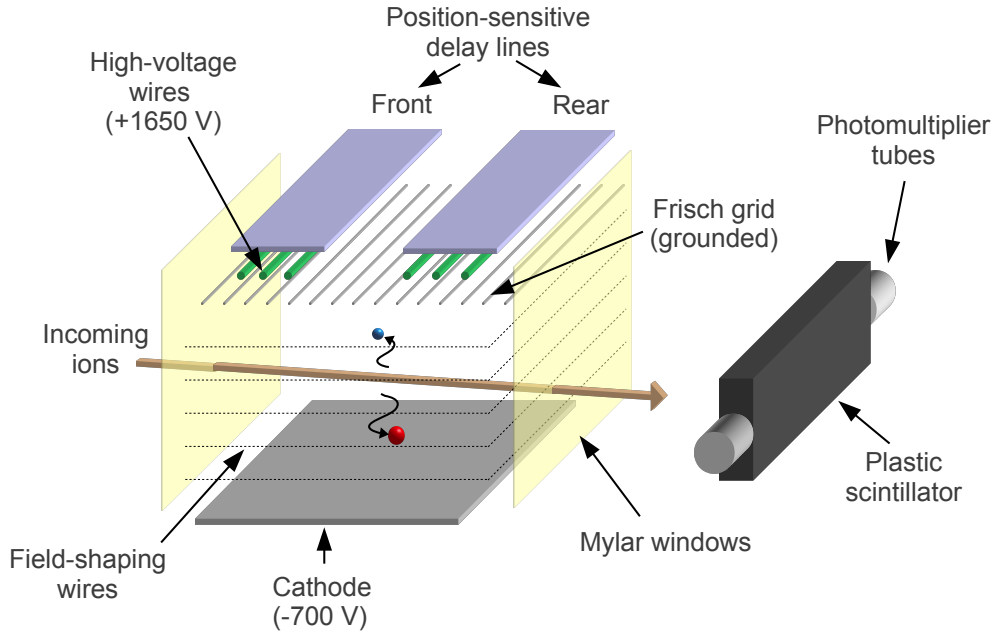

Figure 3.5: Simple schematic of the focal-plane detector assembly. The ions first pass through a position-sensitive ionisation chamber before being stopped within a plastic-scintillator detector.

several cm farther back (the rear wire). Their construction is identical: 220 copper pads are located along a delay line with a 5-ns delay between each pad, generated by 22 delay chips, each with ten taps. The pads are orientated at 45° to the entrance window such that they are parallel to the incoming ion trajectories.

Three high-voltage wires, held at +1650 V, lie between the Frisch grid and delay lines. Electrons drifting through the Frisch grid are accelerated towards the wires across this potential. The increase in field close to the wires leads to an electron avalanche and an induced signal in the pad lying above the avalanche site. The horizontal position at which an ion is detected is inferred using the relative timing of signals from either end of the delay lines.

Recording two position measurements for each ion allows a calculation of trajectories on an ion-by-ion basis to be made. This in turn enables offline corrections to be made to the ion focussing, details of which are discussed

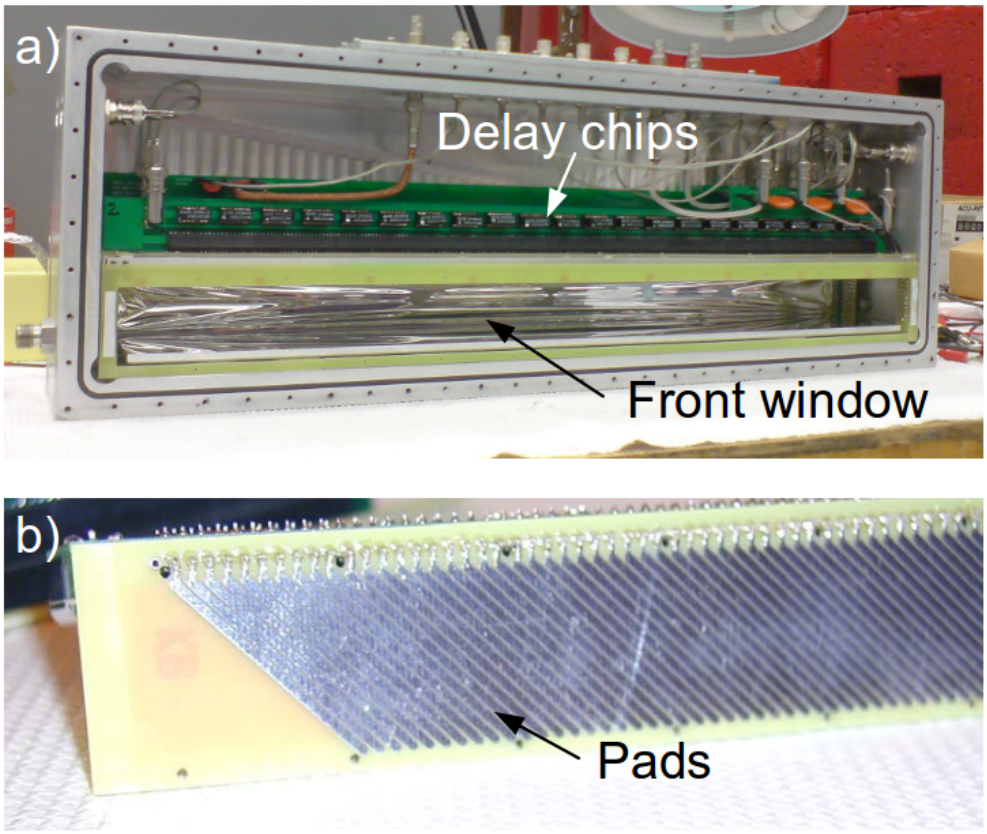

Figure 3.6: a) IC with the front panel and Mylar window removed. The lower third of the chamber comprises the region through which ions pass. The upper region houses the electronics for the delay lines and elements of the gas handling system. b) A close up of the underside of the front wire showing the 1-mm spaced pads, orientated at 45°. The time delay between adjacent pads is 5 ns, generated by the delay chips visible in a).

in Chapter 4. The position resolution of the focal-plane detector is limited to 1 mm by the spacing of pads on the delay line. This lowers the effective momentum resolution of the spectrometer from the value of $R_1 = 4000$ given in the design specifications to that measured of $R_1 \sim 1000$.

Scintillator

A 6.35-mm thick plastic scintillator detector is located immediately after the IC exit window. The light output from the scintillator is collected

by two photomultiplier tubes (PMTs), connected one at each end. Ions are completely stopped within the plastic and their residual energies measured through the combination of the photomultiplier outputs. The total energy deposited in the scintillator is given by

$$E = \sqrt{E_L E_R}, \tag{3.11}$$

where E_L and E_R are the PMT signals from the left and right sides respectively. This measurement is used in conjunction with the energy loss of the ions as they traverse the IC for particle identification. This procedure is discussed in Chapter 4.

3.5 Signal processing

Analogue signals from each of the detectors used were processed and digitised before being written to disk. A block diagram of the electronics used during this work is shown in Fig 3.7.

The energy deposited in each of the scintillator PMTs, the silicon monitor detector and the IC cathode are proportional to their outputs. These signals were amplified and passed to a 32-channel analogue-to-digital converter (ADC) to be digitised and buffered.

Position measurements from the front and rear delay lines were constructed from the relative time difference between signals from their left- and right-hand sides. For both lines, the right-hand signal was used as the start trigger in a time-to-analogue converter (TAC). The left signal was delayed by 50 ns, to ensure arrival after the start trigger, and used as the TAC stop. The amplitude of output signal is directly proportional to the position from which the signal originated along the delay line. The front and rear TAC signals were both fed into ADC channels.

A 16-channel scaler was used to monitor rates within the individual detectors and the beam current on target. The output from each detector was

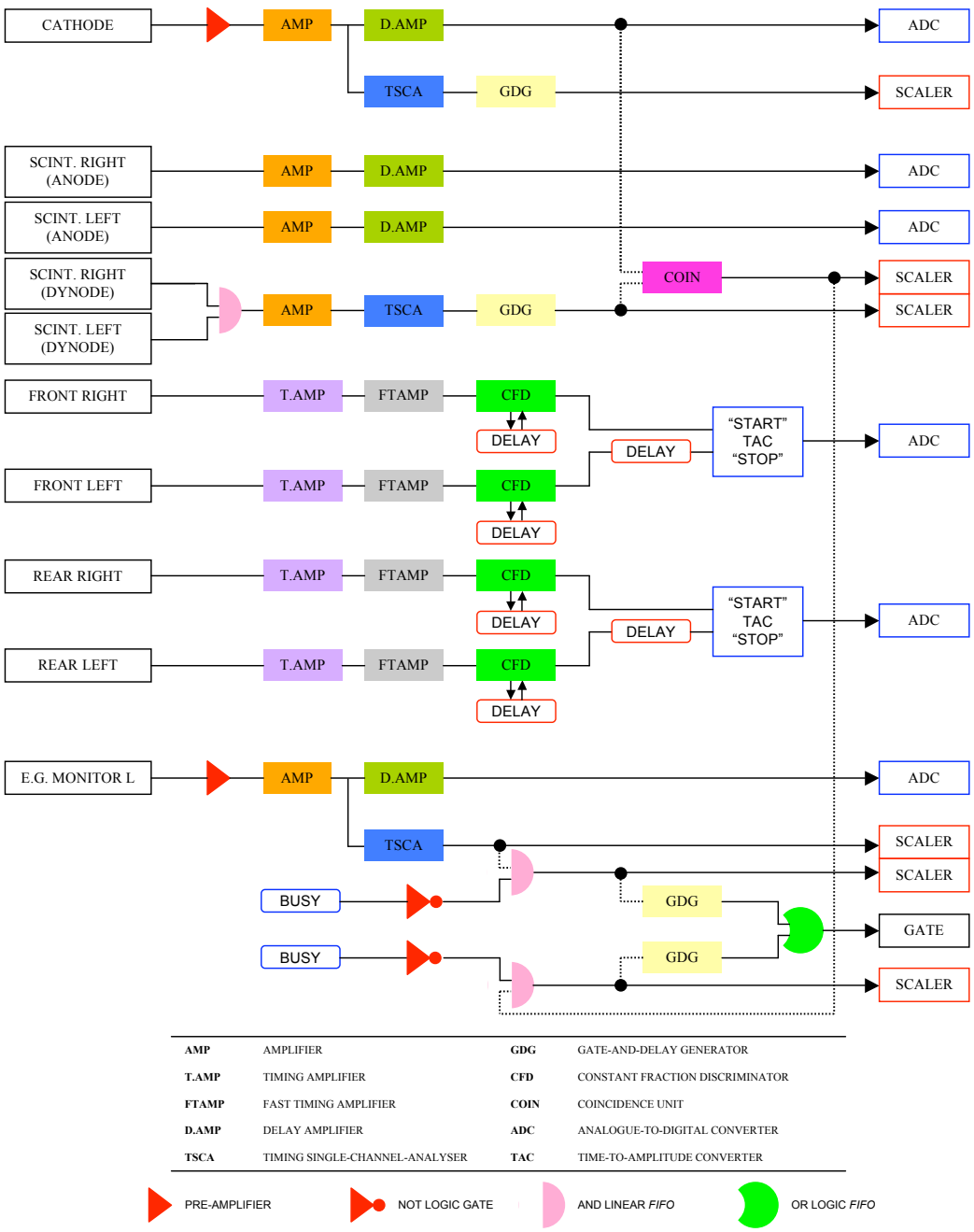

Figure 3.7: Schematic of the electronics setup at WNSL. Figure from [11]

passed through a timing single-channel analyser (TSCA), to obtain a logic pulse, and fed into a scaler channel, which was incremented for each pulse received. The BCI was also connected to a scaler channel, the value of which represented the amount of charge collected on the Faraday cup, as described in Section 3.2.

The trigger condition for events being accepted was taken as either an IC cathode or monitor signal above a threshold set on the relevant CFD. All events not satisfying this condition were discarded. For events satisfying the trigger, the ADC buffer was sent to the data-acquisition system to be packaged into the event format and written to disk.

A busy signal was generated by the ADC crate whilst writing data. This was used as a veto, with triggers occurring in coincidence being rejected. The dead-time associated with these rejected triggers was recorded using two scalers; the raw scaler was incremented by every cathode trigger generated, the live scaler only by triggers not in coincidence with a veto. A ratio of these gives the fractional live time of the acquisition system.

The following chapter will discuss the procedure involved in extracting the desired physical information from the collected data.

CHAPTER

FOUR

ANALYSIS

As with the experimental procedure, the data analysis was performed in a consistent manner to minimise systematic errors. The first step was to select from the data only those events corresponding to the reactions of interest. The data were then calibrated and the states observed in the recoiling nuclei identified. The cross sections for the population of these states were measured using their yields at the focal plane. The angular-momentum transfer involved in populating each state was found through a comparison of cross sections at different spectrometer angles and between different reactions populating the same final states. Spectroscopic factors were extracted using a DWBA analysis.

4.1 Particle identification

In addition to the single-neutron removal reactions of interest in this work, other competing reaction channels are energetically allowed. These add background to the data which it is desirable to remove. This is achieved in part by the transmission of the split-pole spectrograph, since only ions within a limited range of rigidities are transmitted to the focal plane. For ejectiles within this range, the energy-loss characteristics of the ions are used

for identification. A partial energy loss is taken from the cathode of the IC and the remaining contribution from the plastic-scintillator detector. For the light-ion groups of interest in this work, this procedure is sufficient to separate cleanly the species transmitted to the focal plane. Plots of E_{Cath} vs E_{Scint} from both the (p,d) and (^{3}He,α) data are shown in Figure 4.1. Highlighted are events corresponding to the reactions of interest.

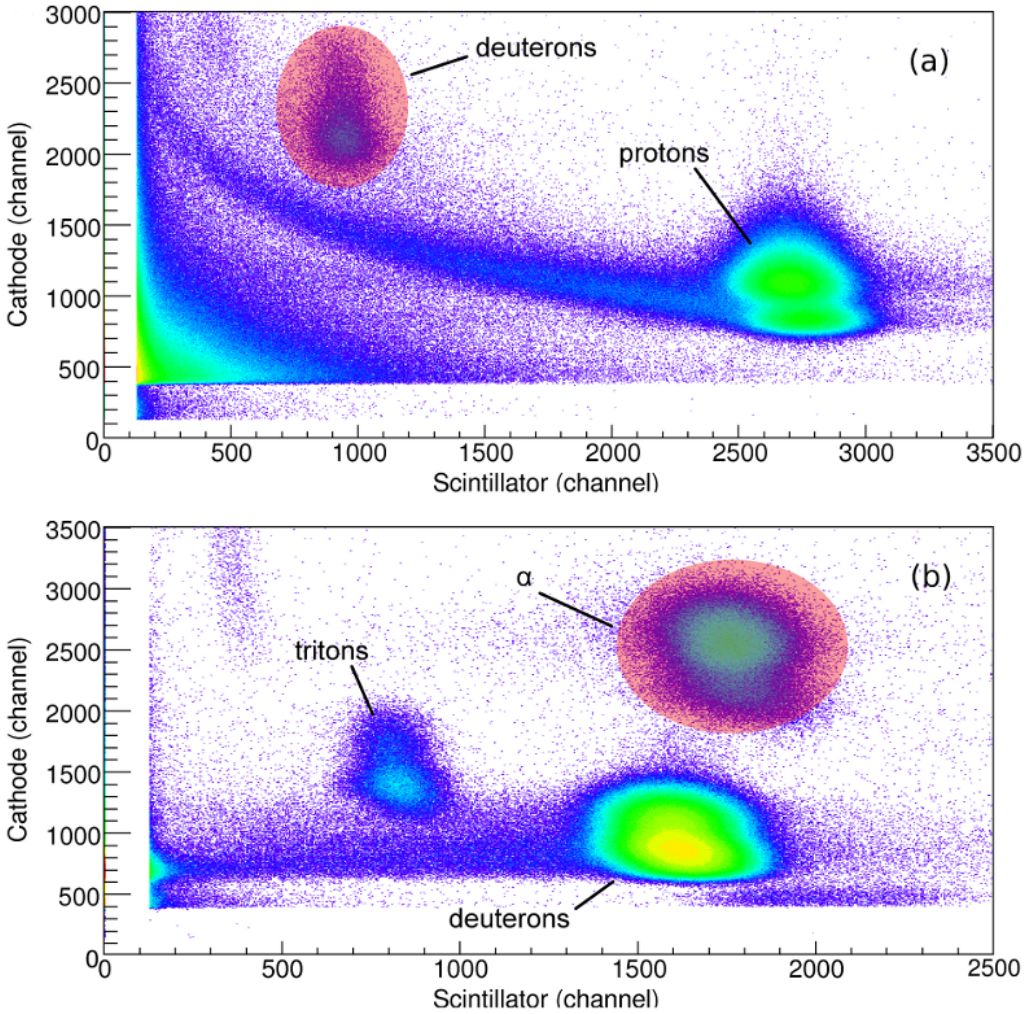

Figure 4.1: ΔE vs E plots showing the separation of particle groups at the focal plane for a) (p,d) at 23 MeV, b) (^{3}He,α) at 34 MeV. The highlighted regions correspond to the particle gates set.

An exception occurs for elastically scattered protons observed in the (p,d) reaction data. Although this group is distinct (as marked on Fig. 4.1), it has a significant tail which impinges on the deuteron group. This constitutes

a major contaminant within the gate set. As discussed in Chapter 3, the rigidities of elastically-scattered protons mean they only obscure states populated above 3 MeV excitation-energy in ^{143}Sm, and so the impact on this work is limited.

Kinematic correction

After selecting events within the particle identification gates shown in Fig. 4.1, the front-wire position gives a spectrum of ejectile rigidities, and hence an excitation spectrum of the recoiling N=81 nucleus. The positioning of the focal plane to correct for kinematic broadening can be verified using the additional position data from the IC rear-wire. The combination of the two positions gives the angle of incidence for each ion, ϕ. For good kinematic correction, the front-wire position should be independent of ϕ for ejectiles resulting from the population of a given state. A plot of ϕ against focal-plane position is shown in Figure 4.2. It is apparent that the kinematic correction in this case is good. The diagonal groups are due to target contaminants and elastically scattered protons, for which the focal-plane position is not optimal. This results in these groups appearing broader in focal-plane spectra.

It should be noted that no gate-conditions were set involving the rear-wire as it was missing in ∼5% of events. The probability of missing rear-wire signal was found to be dependent on focal-plane position, and is believed to be caused by a faulty pre-amplifier at one end of the rear-wire assembly.

4.2 Identification of states

The states populated in the recoiling N=81 nuclei were identified using a calibration of the focal-plane position with respect to ejectile rigidity. During each experiment the spectrometer field was kept at the same value throughout, therefore a single calibration between position and rigidity was required in each case. Both calibrations were performed initially using the

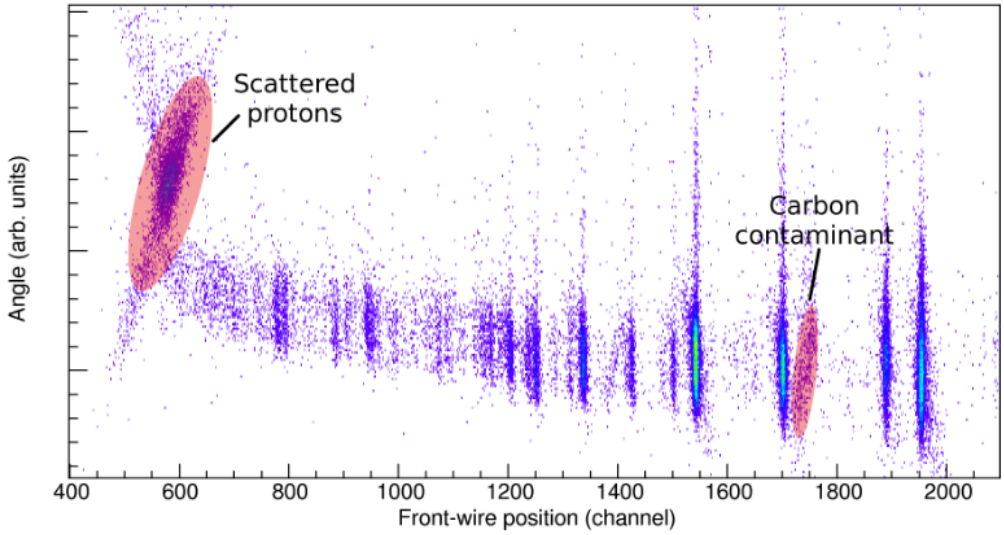

Figure 4.2: The angle of incidence of ions on the focal plane, ϕ, as a function of position. The vertical groups correspond to ions originating in the N=82(p,d)N=81 reaction and demonstrate the good kinematic correction achieved. The diagonal groups are due to the presence of light contaminants in the targets and elastically scattered protons.

known strong, low-lying states present in all four isotones. These calibrations were refined by the inclusion of additional states with known energies and the process iterated several times. The energies used in these calibrations were taken from the evaluations found in Refs. [35–38]. A comparison of the energies reported in the separate studies reported reveals a variation of $\lesssim 1$ % in the measured energies. The energies of previously unknown states were measured with an additional uncertainty of ∼5 keV.

States resulting from light contaminants in the target were identified by the large rate of change of ejectile rigidity with angle; these states shift across the focal-plane with angle relative to those in the N=81 isotones due to the difference in kinematic shift with different masses. In addition, plots such as that in Fig. 4.2 give an indication where a contaminant state overlaps with states of interest as the focus conditions are optimal for N=81 targets so ejectiles from light contaminants display a dependence of position with ejectile energy. In this work, the only such states observed are those expected, associated with ^{13}C and ^{18}O.

Spectra collected for all four isotones using the (p,d) reaction at 42° and the (^{3}He,α) reaction at 15° are shown in Section 4.4. The spectra have been calibrated in terms of the excitation of the N=81 recoil. The consistency of the two calibrations obtained is confirmed by the agreement in excitation energy measured in the two reactions.

4.3 Extraction of cross sections

The differential cross section for the population of each state is determined by the yield of the corresponding peak at the focal-plane, Y. The relationship is

$$\frac{d\sigma}{d\Omega} = \frac{Y}{N_b N_t \Delta\Omega \epsilon}, \tag{4.1}$$

where N_b is the number of beam ions impinging on the target, N_t the target areal density or thickness, $\Delta\Omega$ the entrance solid-angle of the split-pole and ϵ the detection efficiency. N_b is provided by the BCI, which integrates the charge deposited on the Faraday cup, Q. For a beam charge state of q, the number of beam ions delivered is

$$N_b = \frac{Q}{qe}. \tag{4.2}$$

The detector efficiency is given by the fractional live-time of the acquisition system. As described in Chapter 3 this is the ratio of the 'accept' and 'raw' scalers

$$\epsilon = \frac{\text{Accept}}{\text{Raw}}. \tag{4.3}$$

In practice the value of ϵ was found to be a minor correction, staying constant at $\sim$0.995.

The acceptance of the spectrometer was manually set to a nominal 2.8 mb/sr using an adjustable aperture at the entrance to the first dipole magnet. This has been calibrated previously using an α source [39]. Systematic errors due to the calibration of the entrance aperture were eliminated by combining a

measurement of this with the target thickness, described below. The aperture was not adjusted during any of the experimental runs after the initial setting.

Target thickness

Target thickness measurements were made using the elastic scattering of α particles from each target at an energy of 15 MeV and a laboratory angle of 20°. Under these conditions, the cross section for elastic scattering is within < 0.5 % of the value for Rutherford scattering, as demonstrated in Fig. 4.3. The cross section for Rutherford scattering, in the centre-of-mass frame, is given by the relation

$$\frac{d\sigma}{d\Omega} = 1.296 \left(\frac{Z_b Z_t}{E} \right)^2 \frac{1}{\sin^4(\theta/2)}, \tag{4.4}$$

where Z_b and Z_t are the atomic numbers of the beam and target, respectively, and E the beam energy in units of MeV. The resulting cross section is expressed in mb/sr.

Combining Eqns. 4.1 and 4.4, the target thickness can be determined. The yield for α-scattering was taken as the integrated counts in the elastic scatter peak at the focal plane, shown in Fig. 4.4, after the setting of a particle ID gate as described in Section 4.1. The measured target thicknesses presented in Table 3.1 are based upon the nominal spectrometer solid-angle of 2.8 mb/sr. For the cross section determination, however, only the combined quantity $N_t \Delta\Omega$ is required. This product is obtained without needing the value $\Delta\Omega$, effectively calibrating both target thickness and spectrometer aperture.

During the (^{3}He,α) data collection the target thicknesses were monitored using the ratio of beam charge delivered to counts in the silicon monitor detector mounted in the target chamber. The results of these measurements are shown in Figure 4.5. No trends in these ratios greater than the few-% level are observed that could indicate a change in target thickness.

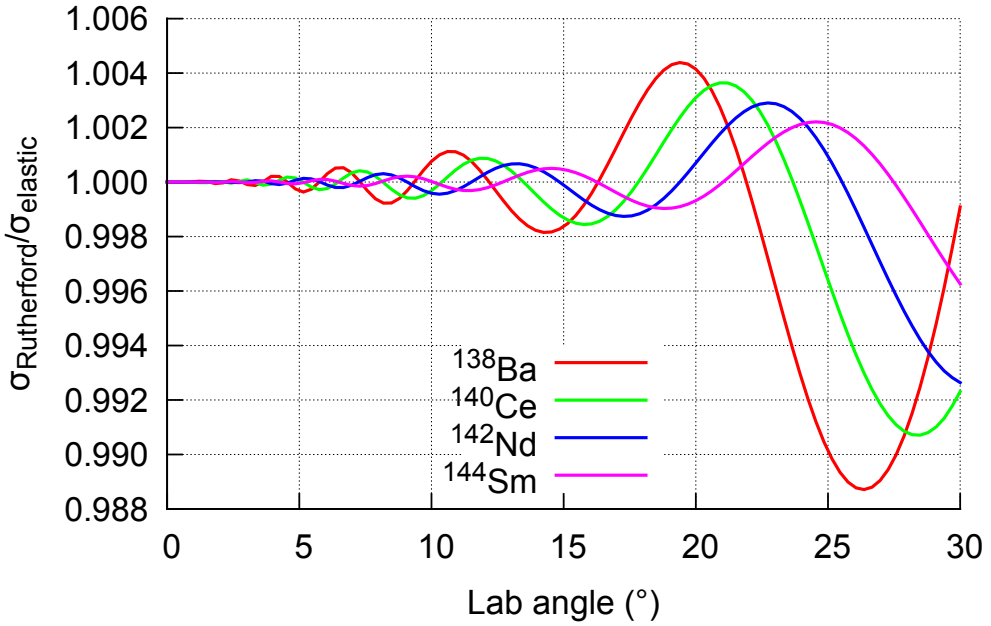

Figure 4.3: Cross section for Rutherford scattering as a fraction of the total elastic-scattering cross section for 15-MeV α particles. The optical potentials used are those quoted in Section 4.4

During the (p,d) data collection the monitor detector failed and so these data are not available. It is unlikely that the targets would be thinned through proton bombardment given the greater energy deposition expected from the ^{3}He beam. Where multiple measurements were taken at the same angle, there is no indication of a change in the ratio of beam-current to ground-state yield above the $\sim$ 2% level. It is therefore assumed that the target thicknesses were unchanged throughout both parts of the experiment.

The product $N_t\Delta\Omega$ was corrected for the known isotopic enrichments of the target material. This gives an effective target thickness with a value of

$$N_t' = N_t P, \tag{4.5}$$

where P is the fractional enrichment of N=82 isotone, as given in Table 3.1.

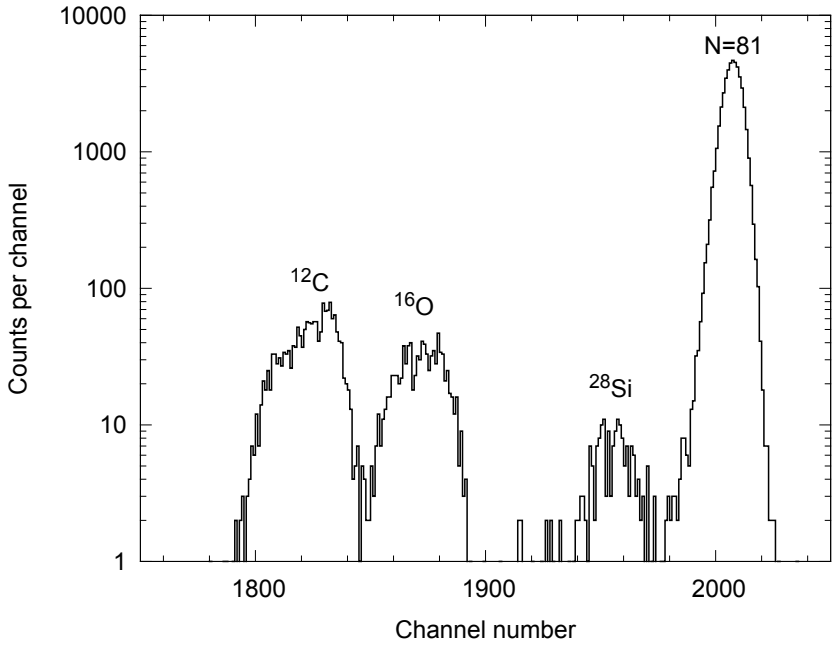

Figure 4.4: Typical focal-plane spectrum obtained from the elastic scattering of α-particles from the N=82 targets at a beam energy of 15 MeV and a spectrometer angle of 20°. Peaks due to scattering from both N=82 nuclei and light contaminants are labelled.

Peak fitting

The yield Y associated with each state was found by fitting Gaussian functions to the data. The widths of the fitted peaks were fixed using strong, well-resolved states in each isotone. The energy calibration was used to fix the centroids when fitting states of known excitation energy. Expressed as the first-order resolving power of the spectrograph (see Chapter 3), the measured peak widths in (p,d) gave R_1=1231±14, and in (^{3}He,α) R_1=1020±13. The lower resolving power with (^{3}He,α) is attributed to increased straggling of the He ions in the targets. These resolving powers translate into energy resolutions of $\sim$ 25 keV for (p,d) and $\sim$ 85 keV for (^{3}He,α). The lower resolution for (^{3}He,α) is a consequence of the large, positive reaction Q-value and high beam energy, which result in ^{3}He ions with energies of $\sim$ 45 MeV, compared to the $\sim$ 10-MeV deuterons resulting from the (p,d) reaction.

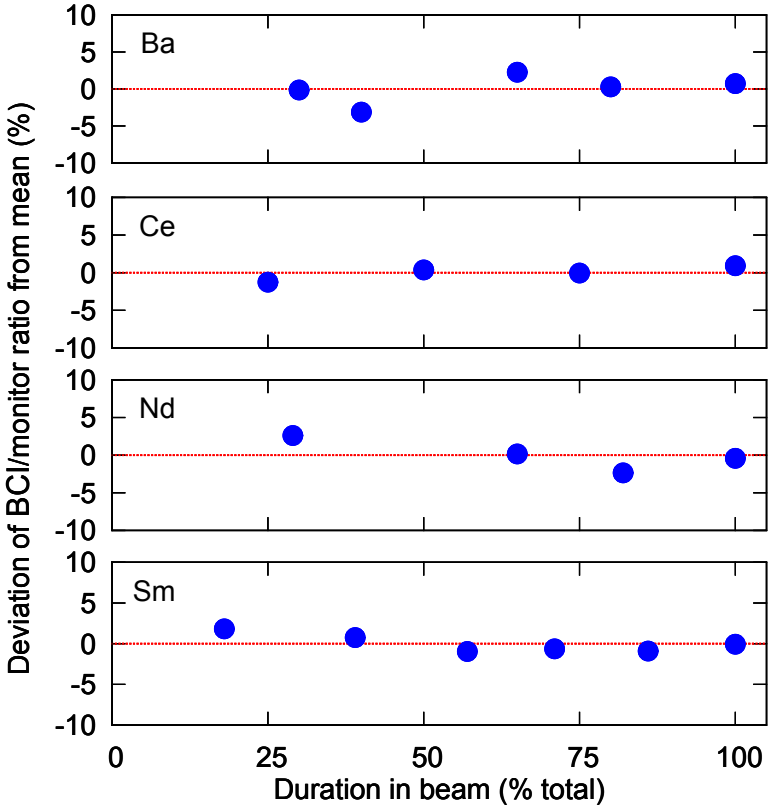

Figure 4.5: Monitoring of target thickness during the 2008 experiment. The percentage deviation of the ratio of beam current to monitor yield is plotted against the time each target was exposed to the beam, as a percentage of the total duration. There is no indication of target degradation. The statistical errors on the data are smaller than the points plotted.

Uncertainties in cross sections

The statistical uncertainties associated with the measured cross sections are $\gtrsim$1% and are dependent on the focal plane yield. There are additional sources of uncertainty which are more difficult to quantify. Of these, some are systematic uncertainties and will not alter the relative cross sections reported.

- The spectrograph angle is estimated to be known to within 0.2°. Due to the strong θ dependence of Rutherford scattering (see Eqn. 4.4), this introduces an error on the values of $N_t\Delta\Omega$ measured. The end result is a systematic uncertainty in the cross sections of $\sim$4%.

- The uncertainty in $N_t\Delta\Omega$ due to deviations from Rutherford scattering are <1%.

- A $\sim$ 2 % systematic uncertainty is introduced through the fixing of peak widths due to the error in the measurements of R_1.

- The systematic uncertainty due to changing the BIC full scale was assessed to be $\lesssim$ 2 %. The full scale was only altered to allow thickness-aperture calibration where significantly lower beam currents were used. The uncertainty associated with the absolute BCI value is $\sim$ 2 %.

- A 5° uncertainty in the orientation of the target ladder relative to the beam axis results in a $\sim$ 0.5 % uncertainty in cross section due to the change in target thickness.

- The isotopic enrichment of the targets have an uncertainty of 0.1 % associated with them.

Combining these gives an estimated uncertainty of $\sim$ 2 % in the relative cross sections and $\sim$ 5 % in the absolute cross sections. The measured cross sections for all states observed are tabulated in Appendix A.

4.4 Measuring L transfer

The spins of states populated are determined through the angular momentum transferred in the reaction, ℓ. All target nuclei have ground-state spins of 0^+, and therefore the transfer of a nucleon carrying L units of angular momentum leaves the recoil nucleus with a spin of $L \pm 1/2$. The parity change of the recoiling nucleus wave function is $\Delta\pi = (-1)^\ell$. Reactions populating single-particle orbitals in the N=50-82 shell are expected to involve ℓ=0 for $s_{1/2}$, ℓ=2 for $d_{3/2}$ and $d_{5/2}$, ℓ=4 for $g_{7/2}$ and ℓ=5 for $h_{11/2}$. It is generally assumed that the ℓ assignment fixes the j value, where a single spin-orbit state is expected close to the Fermi surface. However, without

polarisation measurements, there are no experimental observables that can be used to firmly assign j.

Reactions transferring different ℓ are characterised by the angular distribution of cross sections produced, the origins of which are discussed in Chapter 2. The relative cross section between reactions also depends strongly on ℓ due to the different reaction Q-values (again, see Chapter 2). Through comparison with DWBA calculations, and aided by observations of states with previous firm spin assignments, these features provide a means to identify the fragments of single-particle strength. The potentials used in the DWBA calculations are discussed below.

^{139}Ce, ^{141}Nd and ^{143}Sm have been studied previously using the (p,d), (d,t) and (^{3}He,α) reactions [16–20]. The combination of these data give a rather complete set of ℓ assignments for those states reported. By comparison, the structure of ^{137}Ba is poorly known. Only (p,d) transfer data are reported in the literature, hence the knowledge of high-j states is very limited. For example, ℓ=4 transitions are expected to be populated weakly in (p,d) and in fact the lowest $7/2^+$ state was not observed in these older works [14, 40]. The data collected during this work are sufficient to make independent ℓ assignments for the states observed. The robustness of these assignments may be verified by comparison with well-known states in ^{139}Ce, ^{141}Nd and ^{143}Sm.

Methodology

The choice of angles at which cross sections are measured is discussed in Chapter 2. To recap, measurements are made at 5°, 20°, 35° and 42° for (p,d) and at 5° and 15° for (^{3}He,α), with one additional measurement at 10° for ^{137}Ba. These angles are chosen as they highlight the differences between the distributions, and therefore provide discrimination between different ℓ. A consistent methodology was developed to make ℓ assignments using these data, and is described below.

States with ℓ=0 are identified using the ratio of (p,d) cross sections at 5° and 42°. These data are shown in Fig. 4.6, along with DWBA calculations. The distinctively forward peaked ℓ=0 distribution results in a far larger value for this ratio than for other ℓ values. In practice, any state for which this ratio is $\gtrsim$10 is assigned to be ℓ=0.

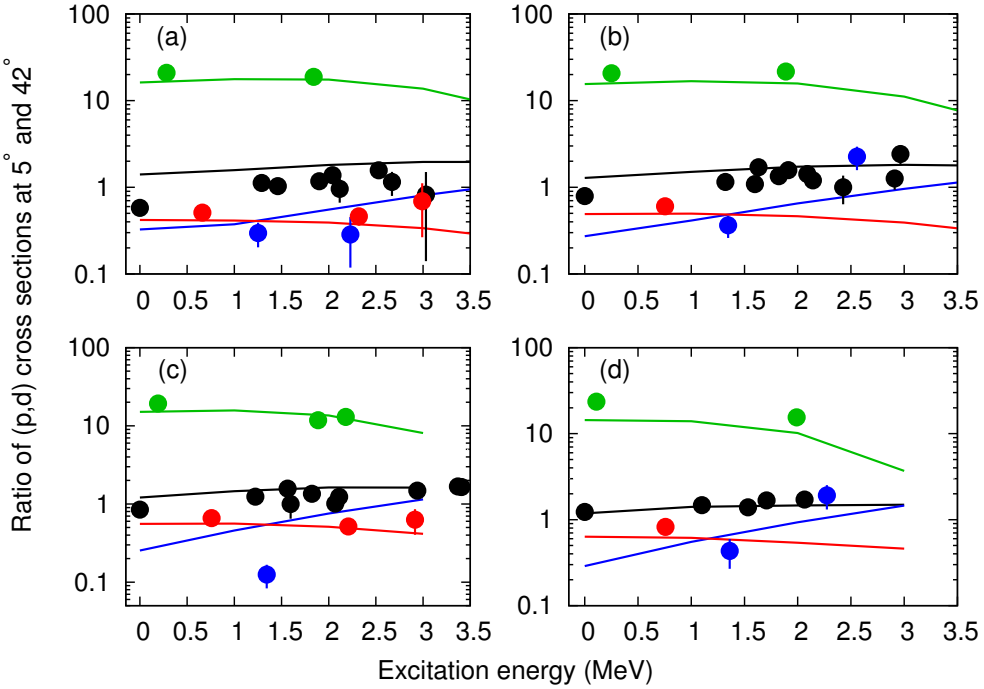

Figure 4.6: The ratio of measured cross sections at 5° and 42° in the (p,d) reaction for states observed in (a) ^{137}Ba, (b) ^{139}Ce, (c) ^{141}Nd and (d) ^{143}Sm. The data are coloured according to the ℓ assignment made with 0 in green, 2 in black, 4 in blue and 5 in red. States for which the cross section was not measured at 5° are not shown. The solid lines are from DWBA calculations (see text for details).

Transitions with ℓ=2 are identified using the ratio of cross sections between the (^{3}He,α) and (p,d) reactions. Figure 4.7 shows the ratio of cross sections at 15° in (^{3}He,α) and 42° in (p,d). In general this ratio is $\lesssim$1 for ℓ=2 transitions and >1 for ℓ=4 and ℓ=5 transitions, although as illustrated in Fig. 4.7 this is somewhat energy dependent. It is assumed that all states with ℓ=0 have already been identified using the procedure above, and so are not included here.

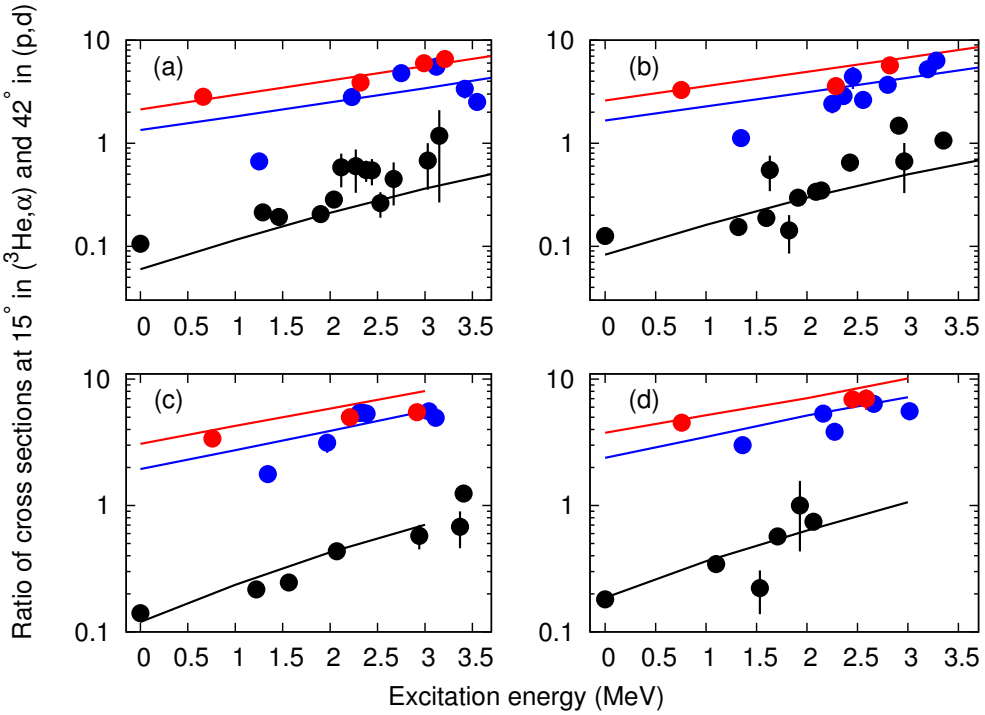

Figure 4.7: The ratio of measured cross sections at 15° in the (^{3}He,α) reaction and 42° in the (p,d) reaction for states observed in (a) ^{137}Ba, (b) ^{139}Ce, (c) ^{141}Nd and (d) ^{143}Sm. The data are coloured according to the ℓ assignment made with 2 in black, 4 in blue and 5 in red. The solid lines are from DWBA calculations (see text for details).

Distinguishing between the remaining ℓ=4 and ℓ=5 states is more challenging. They are both weakly populated in the (p,d) reaction, particularly at forward angles where the distributions would be expected to differ most. Although populated strongly in the (^{3}He,α) reaction, the distributions are very similar. The measurement angles of 5° and 15° were chosen as they provide the maximum discrimination between these two ℓ. The ratio of cross sections between these angles is shown in Fig. 4.8. Where the statistical errors result in an ambiguous assignment using this data, the rationale for the assignments is discussed in detail in later sections.

Where it was possible to obtain cross sections at several angles, the assignments made are confirmed by fitting DWBA distributions to the data. These fits are shown in Figs. 4.11-4.21 for (p,d), and in Fig. 4.10 for the three-point (^{3}He,α) measurements made in ^{137}Ba.

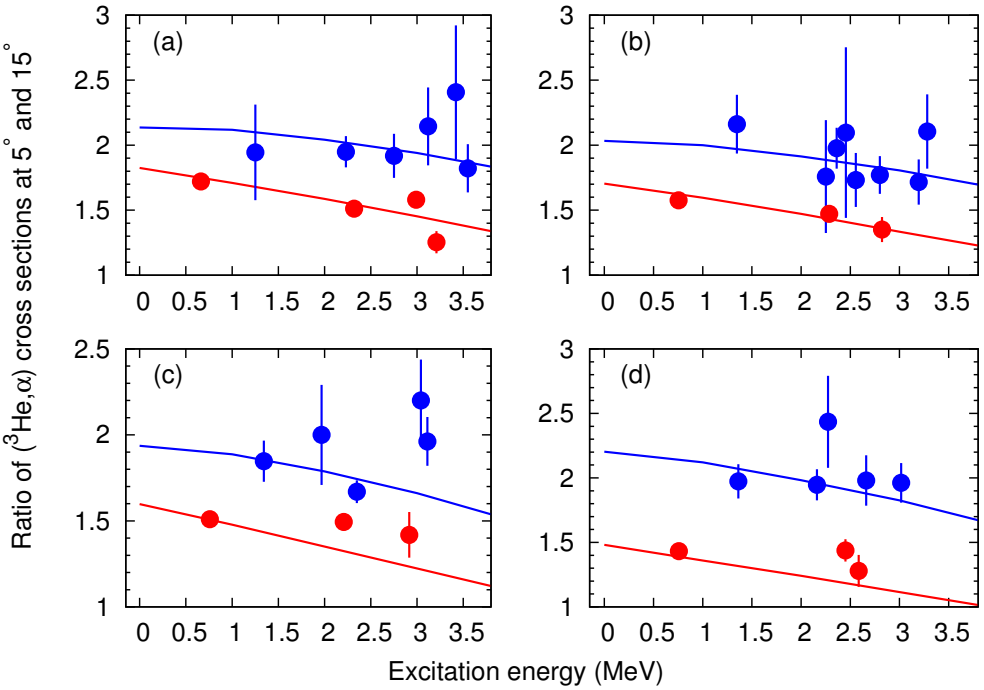

Figure 4.8: The ratio of measured cross sections at 5° and 15° in the (^{3}He,α) reaction for states observed in (a) ^{137}Ba, (b) ^{139}Ce, (c) ^{141}Nd and (d) ^{143}Sm. The data are coloured according to the ℓ assignment made with 4 in blue and 5 in red. For Nd the data for peaks 15-17 (∼2.35 MeV) are combined, see Section 4.4 for details. The solid lines are from DWBA calculations (see text for details).

DWBA calculations

DWBA calculations serve two purposes in this work. Comparing the output angular distributions with those measured gives information on the L-transfer, while comparisons of the calculated and measured cross sections yield spectroscopic factors. The first of these points is illustrated in the ratio plots and angular distributions. The second point is apparent with reference to Eqn. 2.13, which relates the measured and DWBA cross sections to the target and projectile spectroscopic factors.

The light projectiles used in this work posses a simple structure, which is reflected in a spectroscopic contribution S^p which is common for all states populated in the recoil nucleus. These contributions can be contained within a normalisation coefficient B that is constant for each reaction. Convention-

ally this constant is chosen such that the sum rules for spectroscopic factors associated with a particular single-particle orbital associate full occupancy over low-lying states. In this work, the $2j+1$ factor for 'pickup' reactions is divided out to aid comparisons of strengths between different j states. The expression for the normalised target spectroscopic factor is written

$$S_{n,j,\ell} = B\frac{\left(\frac{d\sigma}{d\Omega}\right)_{exp}}{(2j+1)\left(\frac{d\sigma}{d\Omega}.\right)_{DWBA}}. \tag{4.6}$$

All DWBA calculations in this work were performed using the computer code PTOLMEY. As input this requires optical-model potentials for both the initial and final partitions, as well as nucleon bound-state potentials for the target and projectile systems. The parameters used for this work are in Table 4.1. It should be noted that the optical potentials chosen are physically plausible, with well depths $\sim 50A$ MeV, which are fitted to data sets which include reaction conditions similar to those encountered here, and reproduce the observed angular distributions (see figures in the following sections). Similarly, the bound-state potentials have parameters which are physically sensible in their magnitudes, and also consistent with previous, similar analyses. The uncertainty introduced through the choice of these potentials is discussed in the following chapter.

Details of all states observed, together with spin assignments and spectroscopic factors are presented in the following sections. Normalisation factors of $B_{(\mathrm{p,d})}$=1.72±0.06 and $B_{(^3\mathrm{He},\alpha)}$=1.08±0.06 are found for the two sets of reaction data.

These are chosen to give the full strength of $s_{1/2}$ in (p,d) and $h_{11/2}$ in (^{3}He,α), reflecting the states for which each reaction is best matched. The near factor of two difference between these values is physically consistent with the expected projectile spectroscopic factors for the $s_{1/2}$ orbital in the deuteron and α-particle of 1.0 and 2.0 respectively.

Table 4.1: Optical and bound-state potentials used in this work. Parameters marked ⋆ were adjusted to reproduce the measured binding energies.

	Real			Spin-orbit			Vol. imag.			Surf. imag.				
System	V	r_0	a_0	V_{SO}	r_{SO}	a_{SO}	W	r_W	a_W	W_D	r_D	a_D	r_C	source
p	49.75	1.25	0.65	7.5	1.25	0.47	-	-	-	13.5	1.25	0.47	1.25	[41]
d	100.89	1.15	0.81	-	-	-	-	-	-	17.85	1.34	0.68	1.15	[42]
^{3}He	152	1.24	0.69	-	-	-	23	1.43	0.87	-	-	-	1.3	[43]
α	207	1.3	0.65	-	-	-	28	1.3	0.52	-	-	-	1.3	[44]
N=81+n	⋆	1.25	0.63	7.0	1.10	0.50	-	-	-	-	-	-	1.2	[45]
p+n	⋆	1.2	0.65	-	-	-	-	-	-	-	-	-	1.2	[46, 47]
^{3}He+n	⋆	1.2	0.65	-	-	-	-	-	-	-	-	-	1.2	[48]

^{137}Ba

Of the four isotones studied, ^{137}Ba is the least well known. Twenty-eight states are observed in the data (see Fig. 4.9), of which nine were not seen in previous work. A further five were observed previously but lacked spin assignments. Following this analysis only two states remain unassigned, both observed in (p,d) with cross sections <1% of the ground state. The assigned ℓ and measured spectroscopic factors from both sets of data are in Table 4.2. Measured angular distributions are presented in Figs. 4.10, 4.11 and 4.12.

The assignments given for Peaks 1-3 and 5-9 are in agreements with those in Refs. [14, 40]. The non-observation of Peak 4 in those studies is likely due to it being masked by its more intense neighbour. A peak at this energy has been observed in Coulomb excitation studies and assigned spin $7/2^+$ [49]. This is consistent with both the data collected here and the systematics of the lowest lying ℓ=4 states across N=81, hence this assignment is retained.

The remaining nineteen peaks were assigned ℓ values based upon the methodology presented earlier. Of the five states with previous assignments, two are altered. Peak 16, reported as ℓ=4 in Ref. [40], is populated weakly in (^{3}He,α) (see Fig. 4.7) and so reassigned as ℓ=2. Peak 22 is assigned ℓ=5 based upon the three-point (^{3}He,α) distribution.

States populated with ℓ=2 may correspond to either $d_{3/2}$ or $d_{5/2}$ strength. In previous studies it has been argued that the full $d_{3/2}$ strength is exhausted by the ground state, and therefore all other ℓ=2 states carry $d_{5/2}$ strength. Due to the lack of discriminating data, the same treatment is used, tentatively, in this work. The validity of this assumption is discussed in the following chapter, together with a more general discussion of the fragmentation of strength observed.

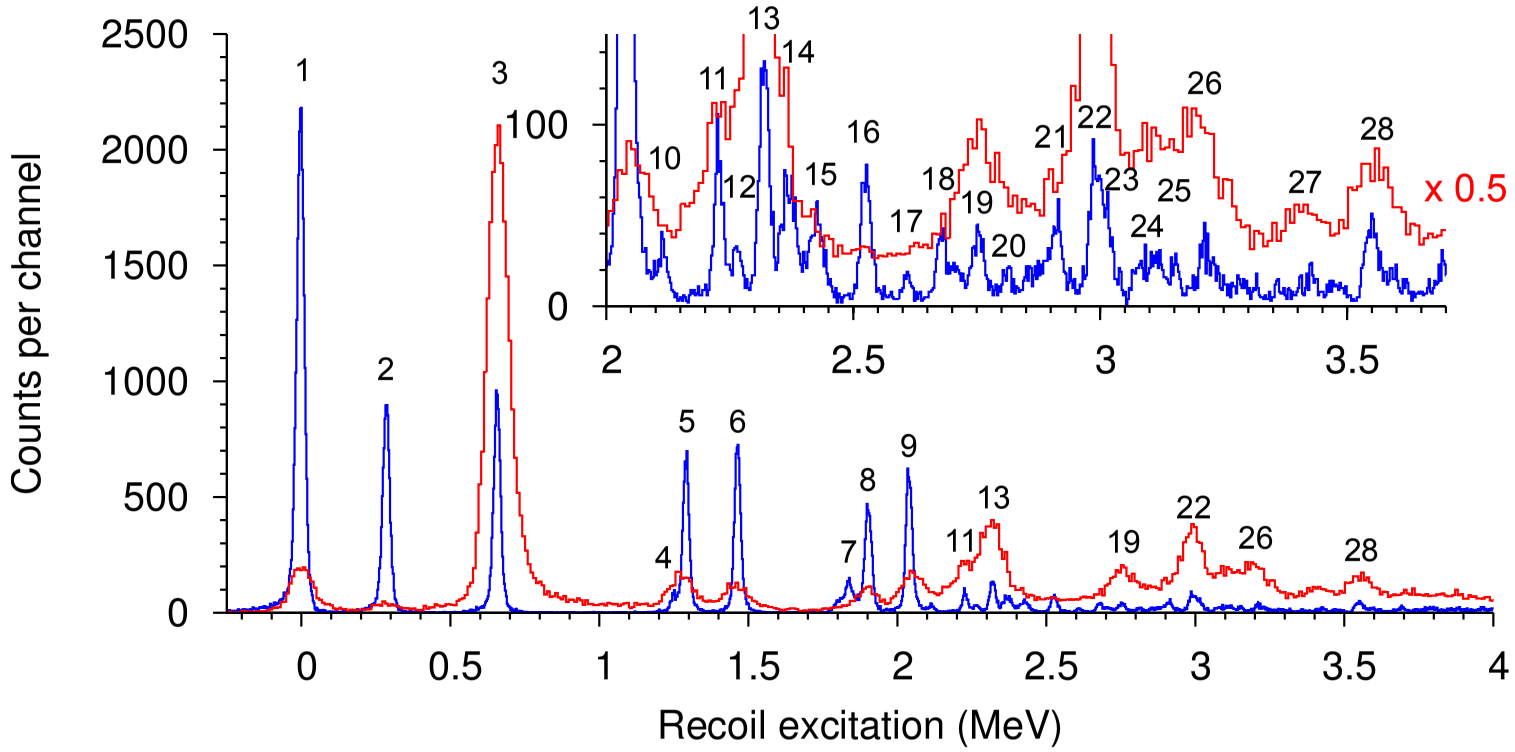

Figure 4.9: Spectra corresponding to the (p,d) reaction at 42° (blue) and (^{3}He,α) reaction at 15° (red) populating states in ^{137}Ba. The peaks are labelled according to their entry in Table 4.2. The (^{3}He,α) data have been scaled by a factor of 0.5 in the inset plot.

Table 4.2: States observed in ^{137}Ba, populated using the (p,d) and (^{3}He,α) reactions, and normalised spectroscopic factors. Results marked * represent upper limits.

				S	
Peak	E (MeV)	L	J	(p,d)	(^{3}He,α)
1	0.000	2	$3/2^+$	0.678 6	1.64 3
2	0.281	0	$1/2^+$	0.749 7	8.9* 7
3	0.662	5	$11/2^-$	0.494 7	0.792 5
4	1.252	4	$7/2^+$	0.102 5	0.044 4
5	1.290	2	$5/2^+$	0.153 3	0.32 2
6	1.460	2	$(5/2^+)$	0.177 3	0.308 9
7	1.840	0	$1/2^+$	0.137 4	0.5* 3
8	1.900	2	$(5/2^+)$	0.126 2	0.211 7
9	2.040	2	$(5/2^+)$	0.167 3	0.31 1
10	2.117	2	$(5/2^+)$	0.010 1	0.04 1
11	2.230	4	$7/2^+$	0.106 6	0.128 4
12	2.271	(2)	$(5/2^+)$	0.009 1	0.08* 2
13	2.320	5	$11/2^-$	0.107 4	0.112 2
14	2.380	(2)	$(5/2^+)$	0.021 1	0.095* 6
15	2.440	2	$(5/2^+)$	0.019 1	0.048 7
16	2.530	2	$(5/2^+)$	0.020 1	0.031 5
17	2.610	-	-	-	-
18	2.670	2	$(5/2^+)$	0.011 1	0.029 9
19	2.750	4	$7/2^+$	0.061 5	0.114 5
20	2.810	-	-	-	-
21	2.890	2	$(5/2^+)$	0.013 1	0.107 9
22	2.990	5	$11/2^-$	0.073 5	0.098 2
23	3.030	2	$(5/2^+)$	0.015 1	0.05* 1
24	3.120	4	$7/2^+$	0.037 5	0.088 7
25	3.150	(2)	$(5/2^+)$	0.007 1	0.03* 1
26	3.210	5	$11/2^-$	0.032 3	0.046 2
27	3.420	4	$7/2^+$	0.024 4	0.029 3
28	3.550	4	$7/2^+$	0.080 6	0.070 4

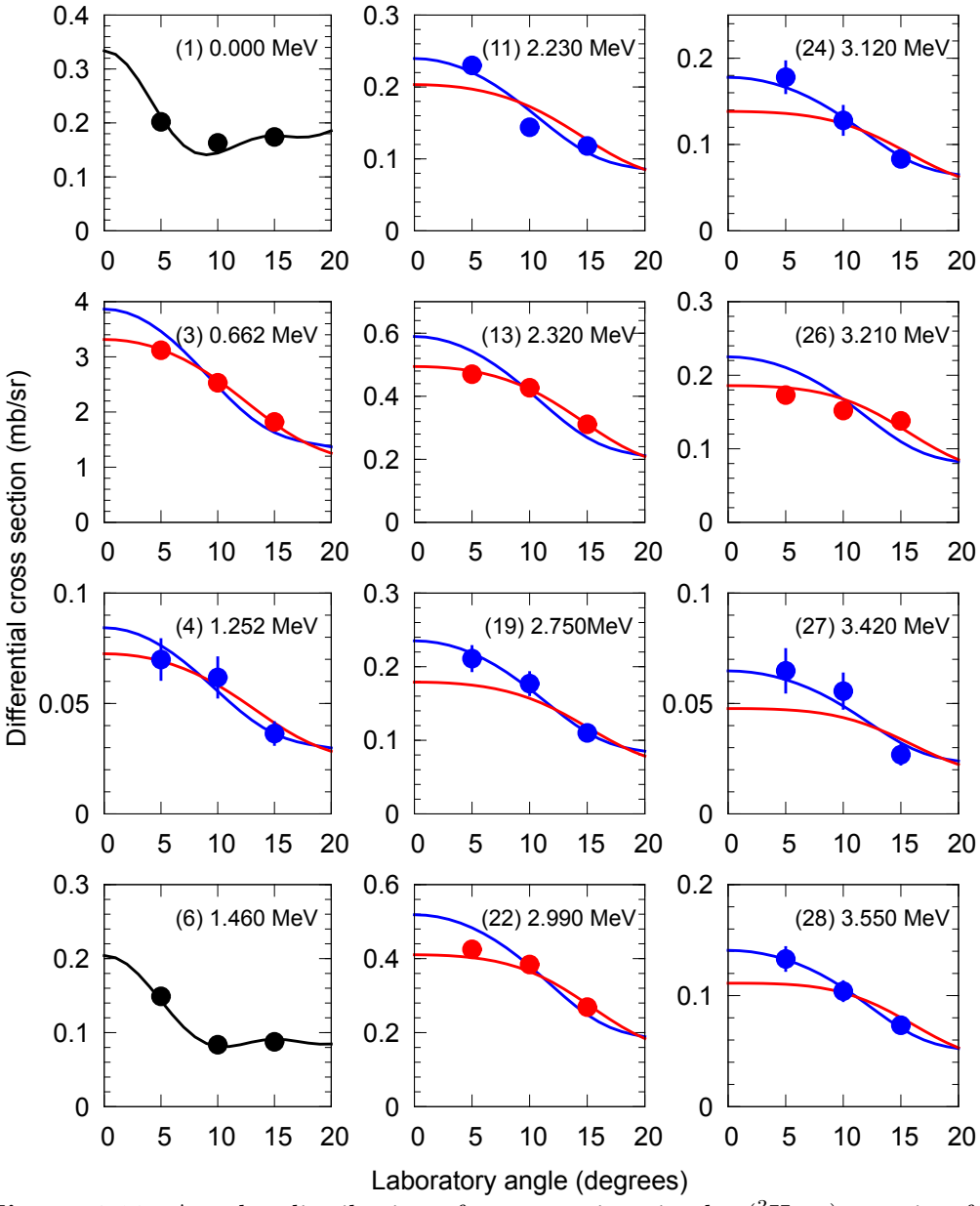

Figure 4.10: Angular distribution of cross sections in the (^{3}He,α) reaction for all states assigned ℓ=4 or 5 strength in ^{137}Ba. Distributions for the lowest two $\ell = 2$ states are also shown. DWBA calculations are shown for ℓ=2 in black, ℓ=4 in blue and ℓ=5 in red. The data points are coloured according to the assignment made. All cross sections are in the lab frame.

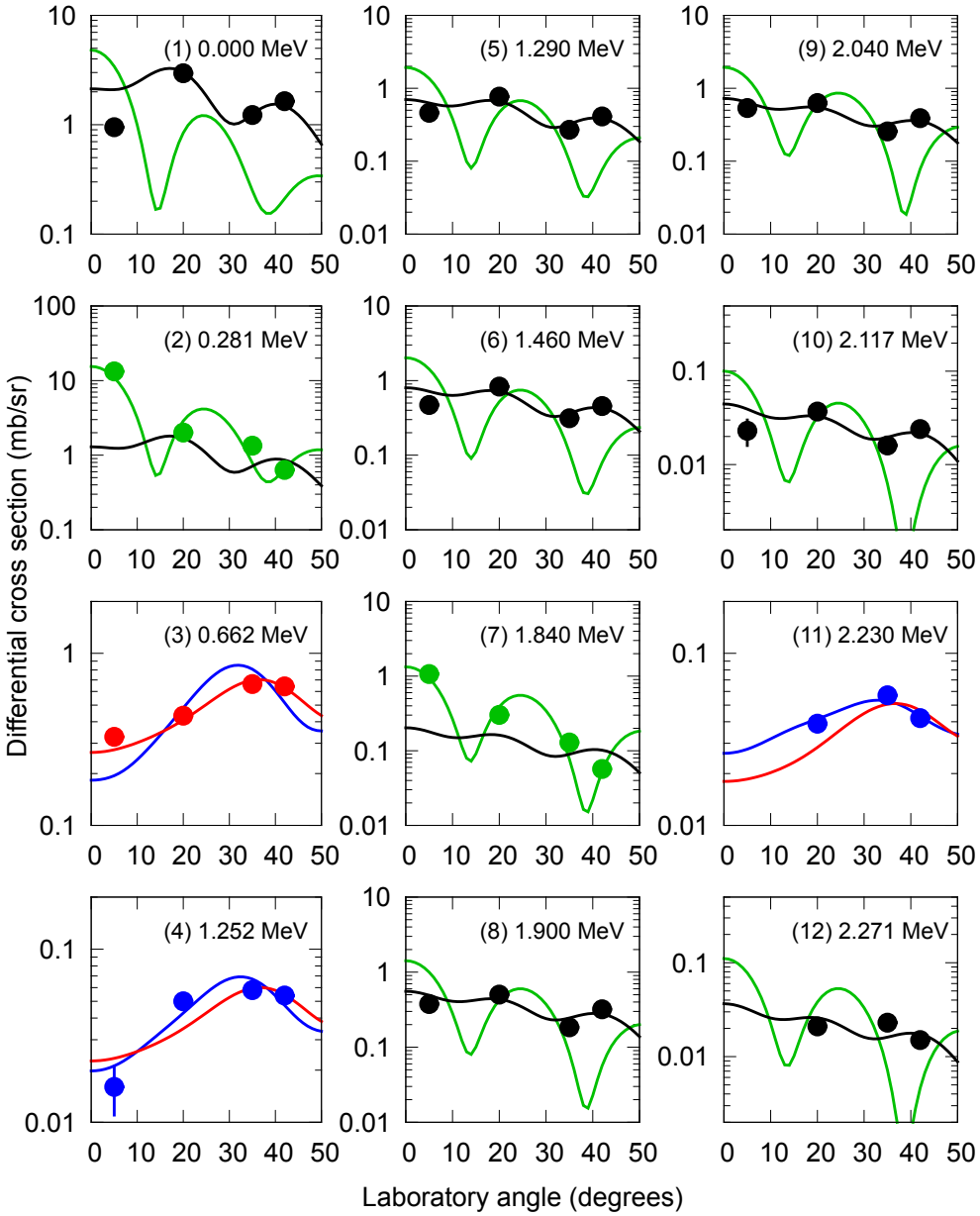

Figure 4.11: Angular distribution of cross sections in the (p,d) reaction for states 1 to 12 observed in ^{137}Ba. DWBA calculations are shown for ℓ=0 in green, ℓ=2 in black, ℓ=4 in blue and ℓ=5 in red. The data points are coloured according to the assignment made. All cross sections are in the lab frame.

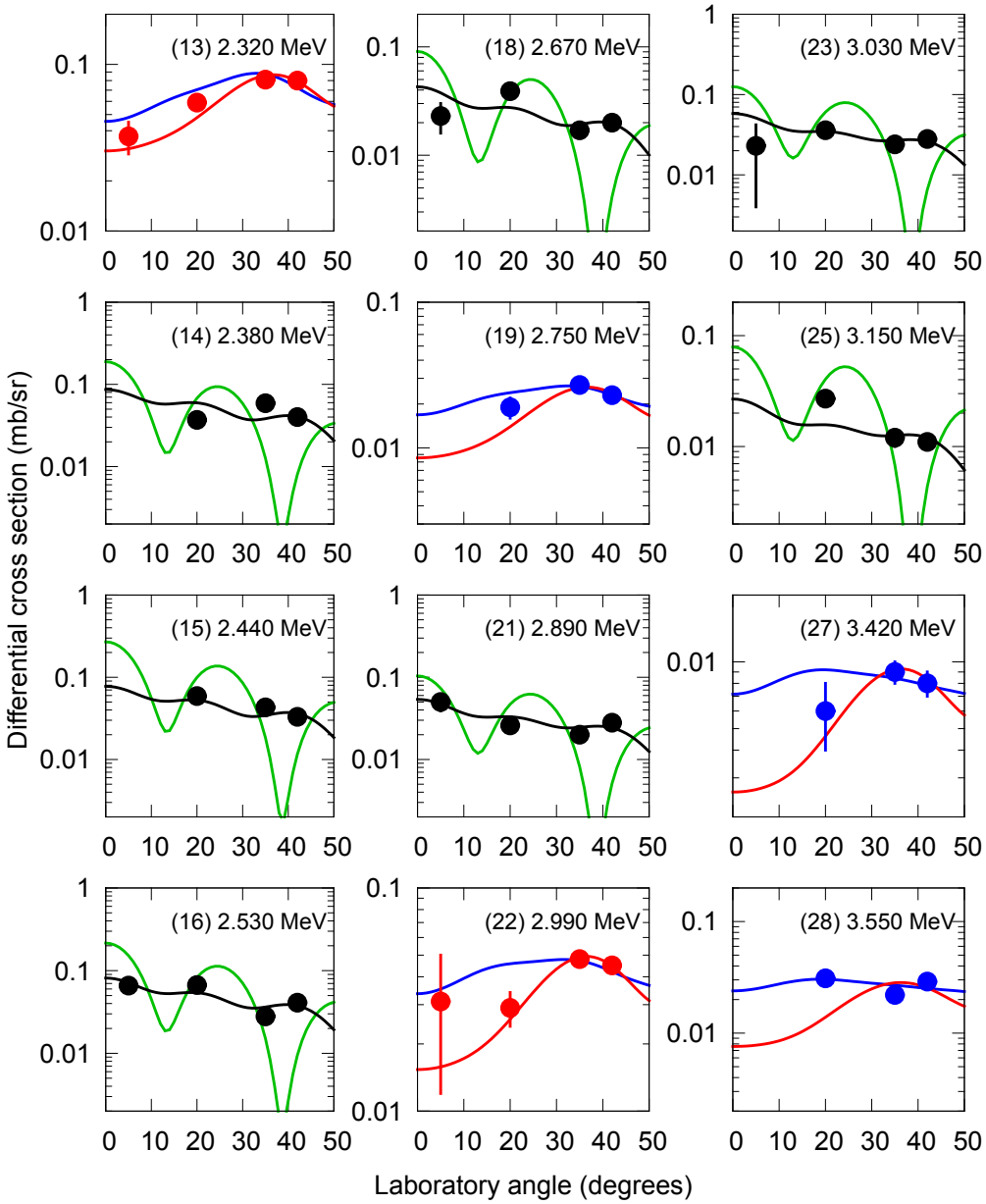

Figure 4.12: Angular distribution of cross sections in the (p,d) reaction for states 13 to 28 observed in ^{137}Ba. DWBA calculations are shown for ℓ=0 in green, ℓ=2 in black, ℓ=4 in blue and ℓ=5 in red. The data points are coloured according to the assignment made. All cross sections are in the lab frame.

^{139}Ce

Twenty-nine states are observed in ^{139}Ce (see Fig. 4.13), all of which are reported in the literature. Some changes are made to the previously assigned ℓ values. Four states remain unassigned after this analysis, all of which are populated in (p,d) with cross sections <1% of the ground state. As discussed for ^{137}Ba, all excited ℓ=2 strength is tentatively assigned as $d_{5/2}$. The assigned ℓ and measured spectroscopic factors from both sets of data are in Table 4.3. Measured angular distributions are presented in Figs. 4.14 and 4.15.

Peak 19 is assigned ℓ=4 strength based upon the cross sections measured in (^{3}He,α) and at 35° and 42° in (p,d). The large cross sections measured at 5° and 20° in (p,d) indicate ℓ=0 strength and so a doublet assignment is made. The spectroscopic factor for each component in (p,d) is taken from the fit of the summed distributions to the data, shown in Fig. 4.15. In (^{3}He,α), the entire strength is taken to be ℓ=4, since the expected cross section for a ℓ=0 state at this excitation is very small.

Peaks 22 and 23 are separated by 22 keV and could not be fitted as independent states using the (^{3}He,α) data. The ratio of the combined yields at 5° and 15° indicate a mixture of ℓ=4 and ℓ=5 strength. The (p,d) data indicates Peak 23 is ℓ=5 and so Peak 22 is assigned ℓ=4. This is in agreement with the assignments in Reference [17]. The cross section for both states in (^{3}He,α) was found by considering the fraction of the total cross section required in each peak to reproduce the 5° to 15° ratio measured.

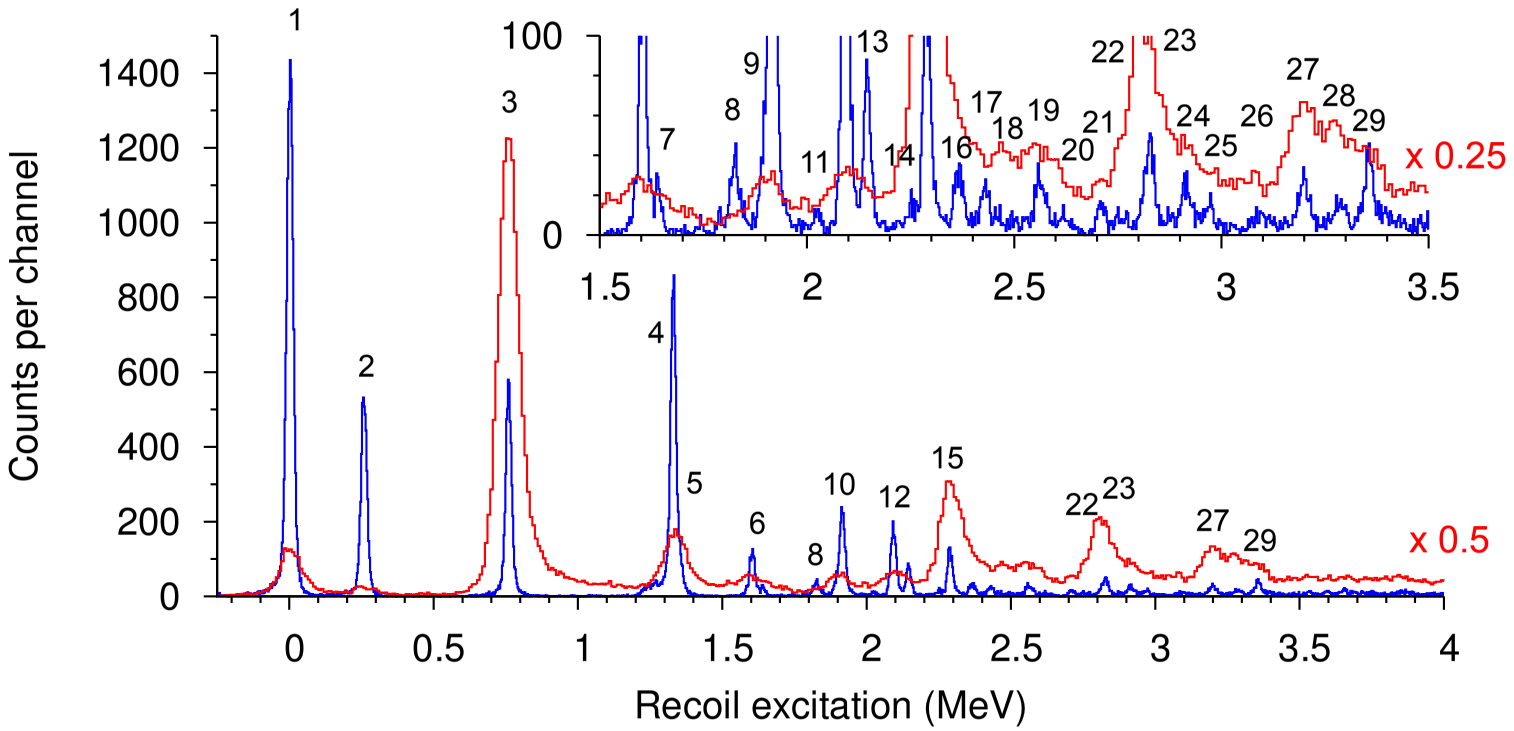

Figure 4.13: Spectra corresponding to the (p,d) reaction at 42° (blue) and (^{3}He,α) reaction at 15° (red) populating states in ^{139}Ce. The peaks are labelled according to their entry in Table 4.3. The (^{3}He,α) data have been scaled by a factor of 0.5 in the main plot and 0.25 in the inset plot.

Table 4.3: States observed in ^{139}Ce, populated using the (p,d) and (^{3}He,α) reactions, and measured spectroscopic factors. Results marked * represent upper limits.

				S	
Peak	E (MeV)	L	J	(p,d)	(^{3}He,α)
1	0.000	2	$3/2^+$	0.683 7	1.4 3
2	0.252	0	$1/2^+$	0.867 9	7.2* 8
3	0.755	5	$11/2^-$	0.540 9	0.725 5
4	1.321	2	$5/2^+$	0.299 5	0.34 2
5	1.347	4	$7/2^+$	0.193 11	0.146 8
6	1.598	2	$(5/2^+)$	0.048 2	0.013 1
7	1.632	2	$(5/2^+)$	0.010 1	0.003 1
8	1.823	2	$(5/2^+)$	0.019 2	0.013 5
9	1.889	0	$1/2^+$	0.019 2	-
10	1.911	2	$(5/2^+)$	0.135 6	0.147 6
11	2.018	-	-	-	-
12	2.090	2	$(5/2^+)$	0.075 2	0.131 9
13	2.143	2	$(5/2^+)$	0.033 2	0.060 7
14	2.251	(4)	$(7/2^+)$	0.033 4	0.031 4
15	2.286	5	$11/2^-$	0.135 6	0.137 3
16	2.362	4	$7/2^+$	0.087 6	0.098 4
17	2.426	2	$(5/2^+)$	0.011 1	0.030* 5
18	2.455	(4)	$(7/2^+)$	0.024 4	0.036 6
19	2.556	4+(0)	$7/2^+$	0.071 7	0.150 8
			$(1/2^+)$	017 7	-
20	2.610	-	-	-	-
21	2.701	-	-	-	-
22	2.800	4	$7/2^+$	0.042 7	0.051 2
23	2.822	5	$11/2^-$	0.058 4	0.065 2
24	2.910	2	$(5/2^+)$	0.015 1	0.072* 5
25	2.964	2	$(5/2^+)$	0.008 1	0.013 6
26	3.082	-		-	-
27	3.196	4	$7/2^+$	0.075 7	0.123 5
28	3.282	4	$7/2^+$	0.042 6	0.079 4
29	3.352	2	$(5/2^+)$	0.019 2	0.063 7

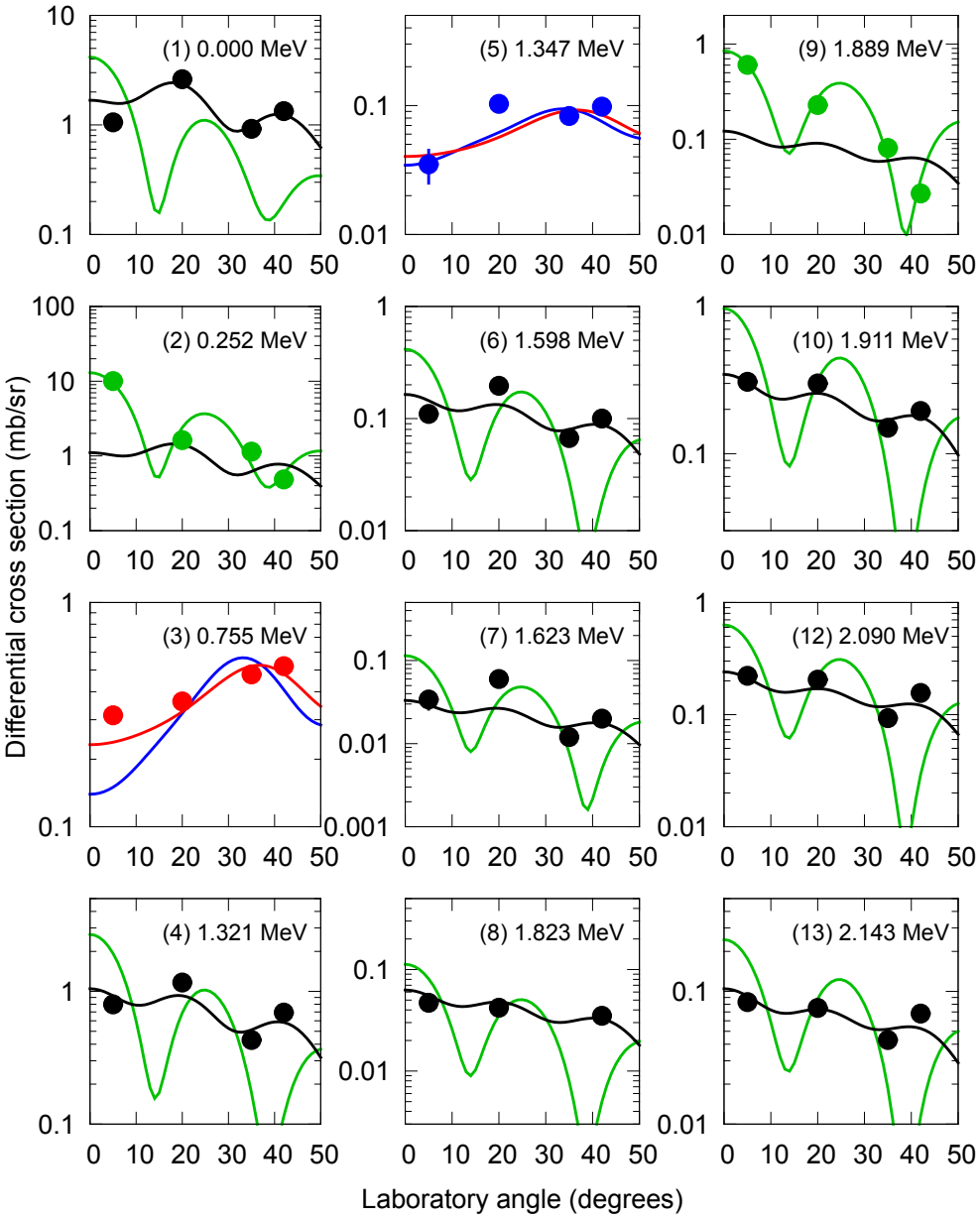

Figure 4.14: Angular distribution of cross sections in the (p,d) reaction for states 1 to 13 observed in ^{139}Ce. DWBA calculations are shown for ℓ=0 in green, ℓ=2 in black, ℓ=4 in blue and ℓ=5 in red. The data points are coloured according to the assignment made. All cross sections are in the lab frame.

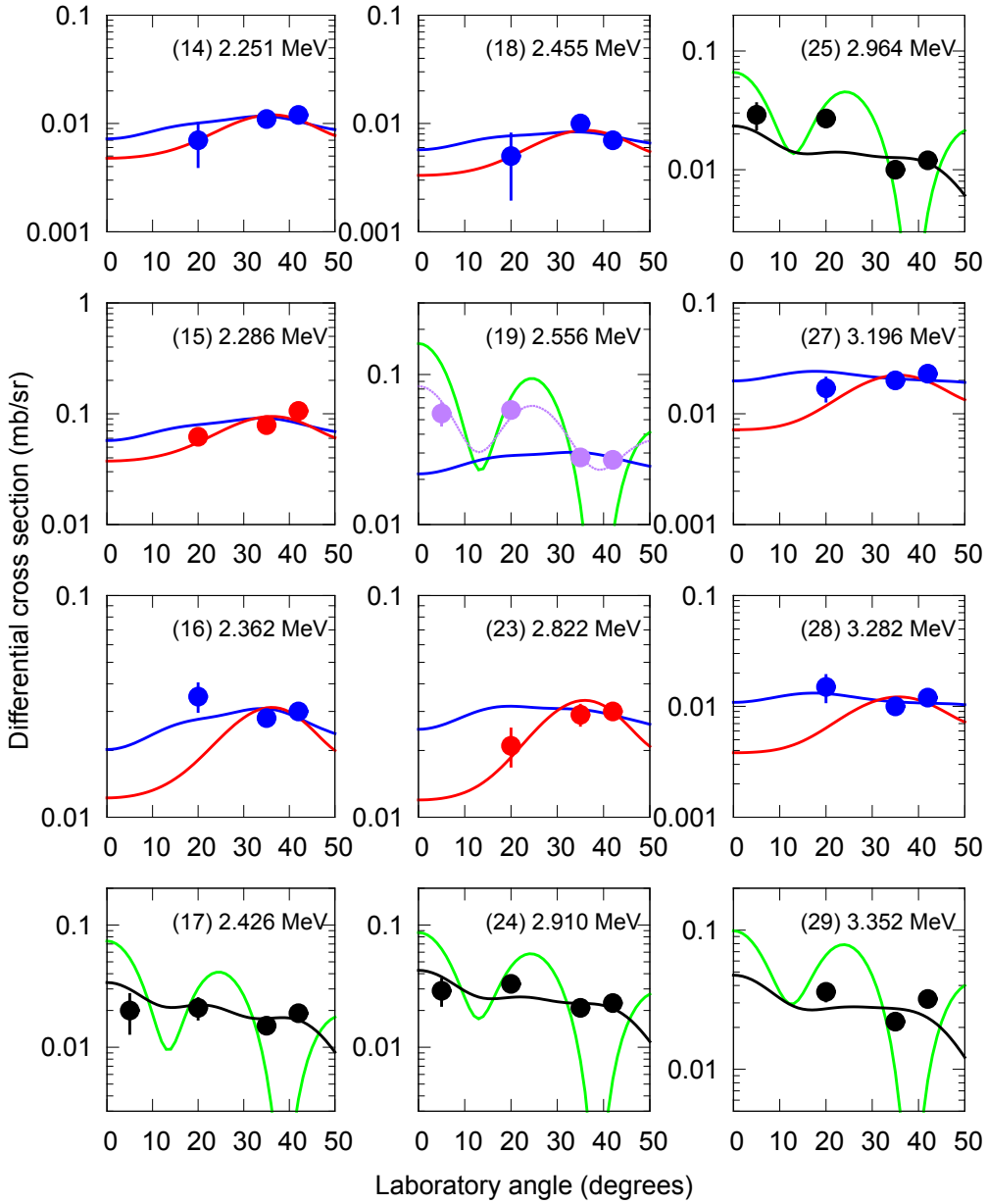

Figure 4.15: Angular distribution of cross sections in the (p,d) reaction for states 14-29 observed in ^{139}Ce. DWBA calculations are shown for ℓ=0 in green, ℓ=2 in black, ℓ=4 in blue and ℓ=5 in red. The data points are coloured according to the assignment made. See the text for details regarding Peak 19. All cross sections are in the lab frame.

Nd

In total twenty-nine states were observed in ^{141}Nd (see fig 4.16), all of which are reported in previous studies. No changes are made to the existing ℓ assignments. Four states remain unassigned after this analysis, each observed in (p,d) with a cross section <1% of the ground state. Again, all high lying ℓ=2 strength is given tentative $d_{5/2}$ assignment (see Section 4.4). The assigned ℓ and measured spectroscopic factors from both sets of data are in Table 4.4. Angular distributions are presented in Figs. 4.17 and 4.18.

Peaks 15, 16 and 17 form a triplet in (^{3}He,α) which can not be reliably fitted as separate states. The ratio of combined cross section between 5° and 15° indicates pure ℓ=4 strength (see Fig. 4.8). This is consistent with the individual (p,d) distributions and also assignments from previous work. To obtain (^{3}He,α) cross sections, the combined yield was divided amongst the three states in proportion to their measured yields in the (p,d) reaction.

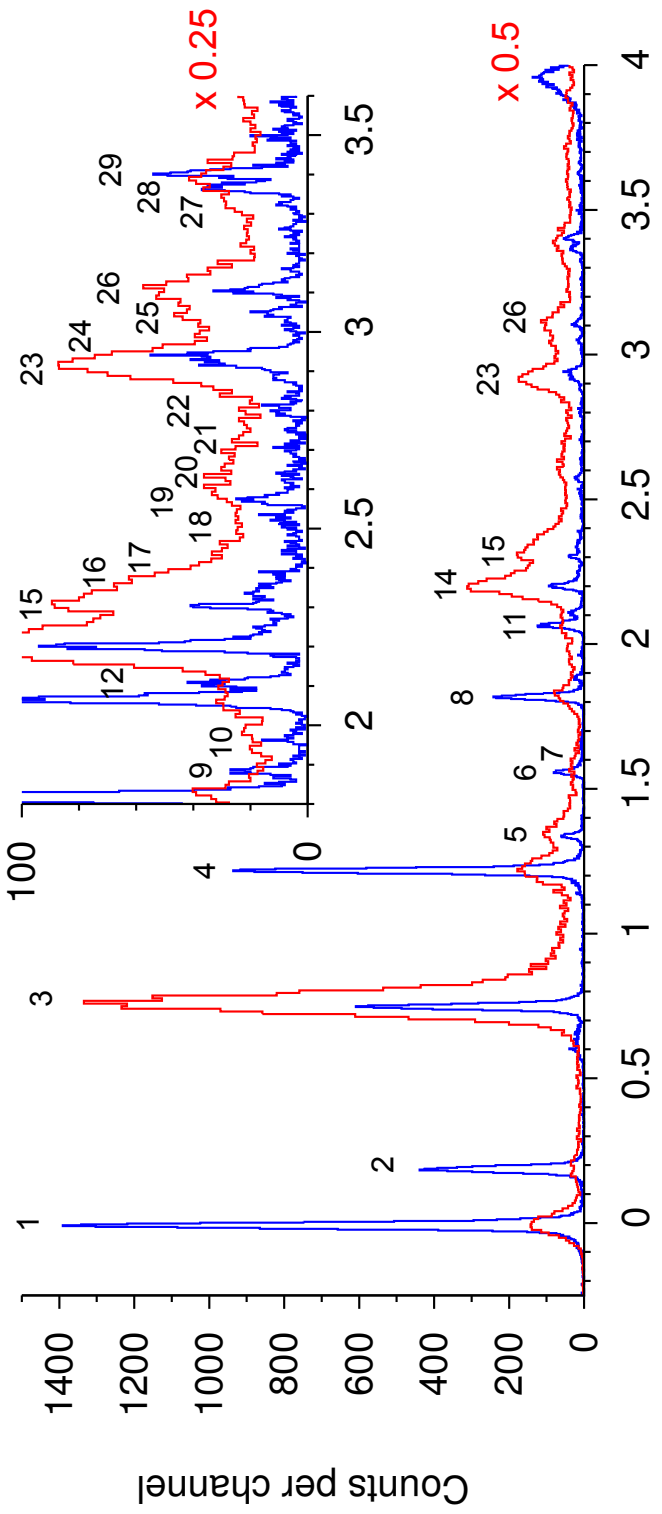

Figure 4.16: Spectra corresponding to the (p,d) reaction at 42° (blue) and (^{3}He,α) reaction at 15° (red) populating states in ^{141}Nd. The peaks are labelled according to their entry in Table 4.4. The (^{3}He,α) data have been scaled by a factor of 0.5 in the main plot and 0.25 in the inset plot.

Table 4.4: States observed in ^{141}Nd, populated using the (p,d) and (^{3}He,α) reactions, and measured spectroscopic factors. Results marked * represent upper limits.

				S	
Peak	E (MeV)	L	J	(p,d)	(^{3}He,α)
1	0.000	2	$3/2^+$	0.770 8	1.21 2
2	0.192	0	$1/2^+$	0.869 9	8.2* 5
3	0.759	5	$11/2^-$	0.667 11	0.755 5
4	1.222	2	$5/2^+$	0.446 6	0.52 1
5	1.343	4	$7/2^+$	0.128 7	0.110 4
6	1.565	2	$(5/2^+)$	0.038 2	0.046 5
7	1.597	2	$(5/2^+)$	0.007 1	0.012 8
8	1.822	2	$(5/2^+)$	0.125 3	0.181 7
9	1.888	0	$1/2^+$	0.107 5	0.2* 2
10	1.968	(4)	$(7/2^+)$	0.028 4	0.028 2
11	2.070	2	$(5/2^+)$	0.069 3	0.113 5
12	2.111	2	$(5/2^+)$	0.024 2	0.011 5
13	2.180	0	$1/2^+$	0.026 3	-
14	2.208	5	$11/2^-$	0.138 8	0.148 2
15	2.310	4	$7/2^+$	0.096 9	0.153 3
16	2.349	4	$7/2^+$	0.064 7	0.092 2
17	2.384	4	$7/2^+$	0.032 6	0.036 1
18	2.512	-	-	-	-
19	2.581	(2)	$(5/2^+)$	0.013 1	0.049* 6
20	2.616	-	-	-	-
21	2.705	-	-	-	-
22	2.809	(2)	$(5/2^+)$	0.008 1	0.004 2
23	2.915	5	$11/2^-$	0.070 6	0.065 3
24	2.939	2	$(5/2^+)$	0.032 2	0.037 7
25	3.042	4	$7/2^+$	0.037 7	0.061 3
26	3.112	4	$7/2^+$	0.083 12	0.092 4
27	3.315	-	-	-	-
28	3.369	2	$(5/2^+)$	0.028 2	0.029 9
29	3.407	2	$(5/2^+)$	0.039 2	0.078 9

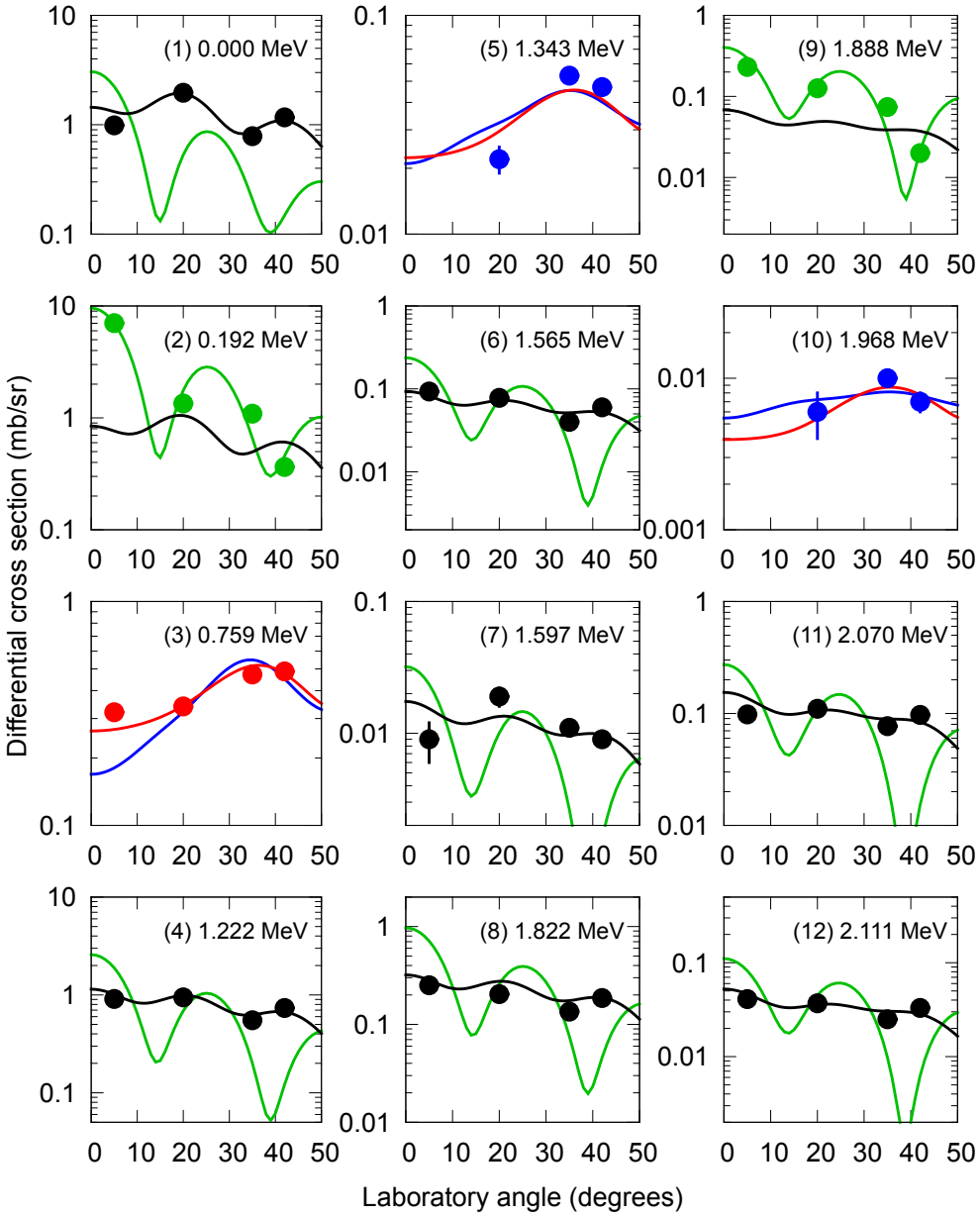

Figure 4.17: Angular distribution of cross sections in the (p,d) reaction for states 1 to 12 observed in ^{141}Nd. DWBA calculations are shown for ℓ=0 in green, ℓ=2 in black, ℓ=4 in blue and ℓ=5 in red. The data points are coloured according to the assignment made. All cross sections are in the lab frame.

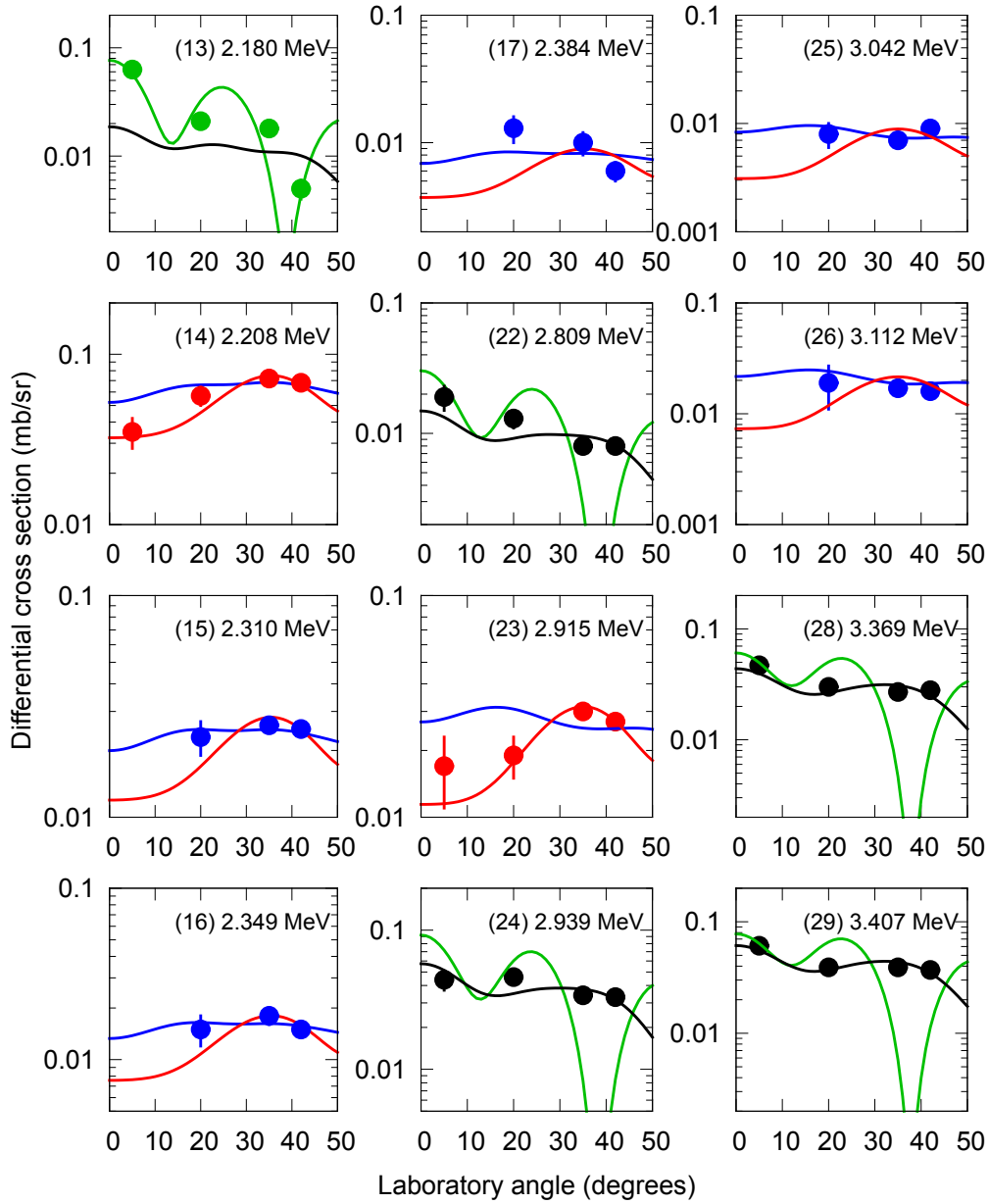

Figure 4.18: Angular distribution of cross sections in the (p,d) reaction for states 13 to 29 observed in ^{141}Nd. DWBA calculations are shown for ℓ=0 in green, ℓ=2 in black, ℓ=4 in blue and ℓ=5 in red. The data points are coloured according to the assignment made. All cross sections are in the lab frame.

^{143}Sm

Data from the ^{144}Sm(p,d)^{143}Sm reaction has a cut-off at ∼3.1 MeV excitation due to the elastic scattering of protons onto the focal plane. Seventeen states are observed below this cut-off (see Fig. 4.19), all of which are known from previous work. The ℓ assignments made are consistent with those in Ref. [17]. Only one state is left without assignment after this analysis, observed only tentatively in (p,d) and with a cross section <1% of the strongest state in (^{3}He,α). The same procedure of assigning all excited ℓ=2 as $d_{5/2}$ strength is adopted, as discussed in Section 4.4. The assigned ℓ and measured spectroscopic factors are in Table 4.5. Angular distributions are presented in Figs. 4.20 and 4.21.

The (^{3}He,α) data is not subject to the same cut-off at 3.1 MeV as (p,d) and two additional states are observed above this excitation. These states are in previous studies and have existing ℓ assignments. As the data from (^{3}He,α) alone are not sufficient to make independent assignments, those given in Ref. [17] are adopted.

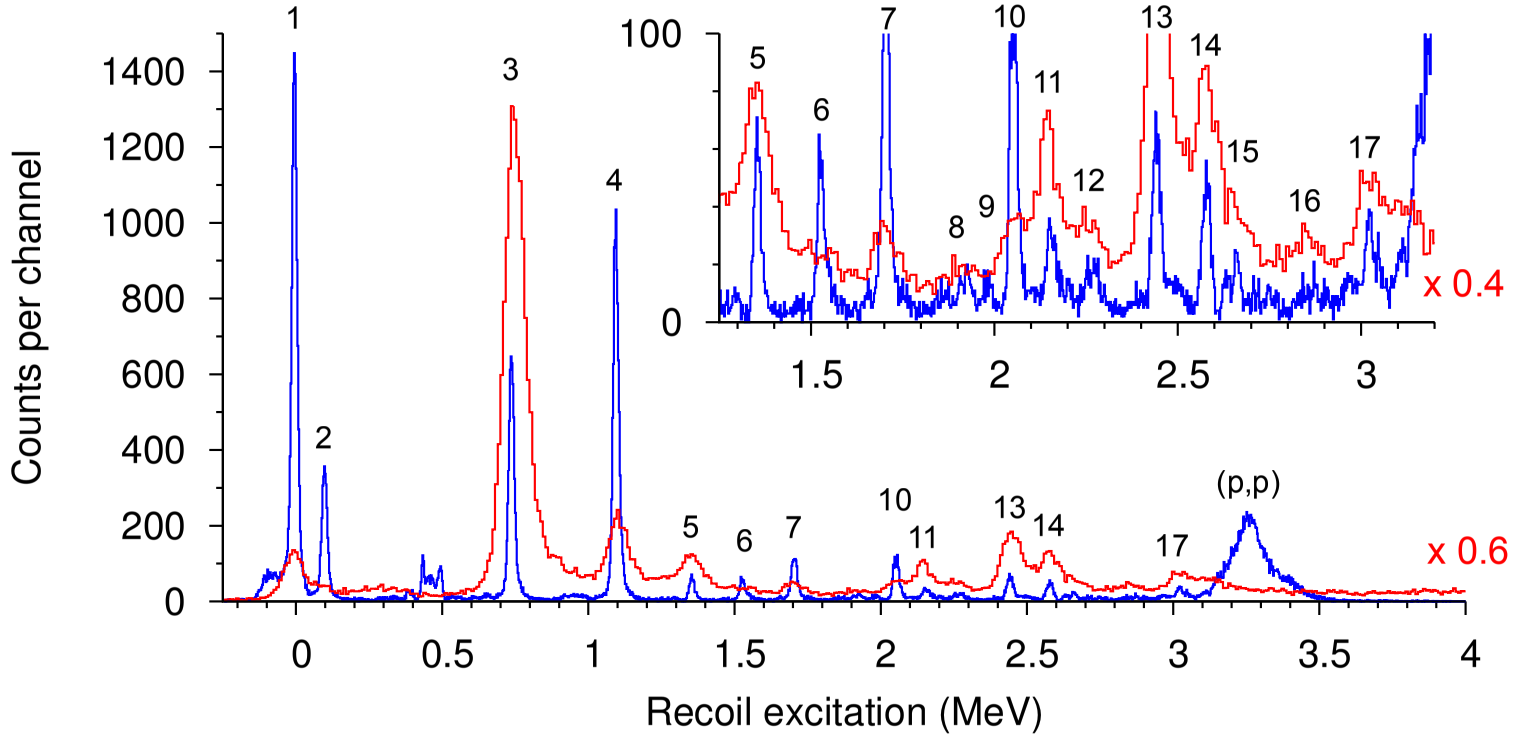

Figure 4.19: Spectra corresponding to the (p,d) reaction at 42° (blue) and (^{3}He,α) reaction at 15° (red) populating states in ^{143}Sm. The peaks are labelled according to their entry in Table 4.5. The (^{3}He,α) data have been scaled by a factor of 0.6 in the main plot and 0.4 in the inset plot.

Table 4.5: States observed in ^{143}Sm, populated using the (p,d) and (^{3}He,α) reactions, and measured spectroscopic factors. Results marked * represent upper limits.

				S	
Peak	E (MeV)	L	J	(p,d)	(^{3}He,α)
1	0.000	2	$3/2^+$	0.813 10	1.05 3
2	0.110	0	$1/2^+$	0.903 12	7.9* 7
3	0.758	5	$11/2^-$	0.731 13	0.878 6
4	1.100	2	$5/2^+$	0.533 8	0.66 2
5	1.362	4	$7/2^+$	0.144 9	0.155 5
6	1.533	2	$(5/2^+)$	0.031 2	0.019 6
7	1.708	2	$(5/2^+)$	0.065 3	0.085 7
8	1.930	2	$(5/2^+)$	0.010 1	0.029 5
9	1.990	0	$1/2^+$	0.091 7	-
10	2.064	2	$(5/2^+)$	0.079 3	0.116 6
11	2.161	4	$7/2^+$	0.111 10	0.145 5
12	2.274	4	$7/2^+$	0.072 8	0.064 5
13	2.450	5	$11/2^-$	0.092 8	0.115 3
14	2.586	5	$11/2^-$	0.064 13	0.072 2
15	2.662	4	$7/2^+$	0.048 9	0.065 4
16	2.842	-	-	-	-
17	3.017	4	$7/2^+$	0.095 19	0.097 4
18	3.085	(2)	$(5/2^+)$	0.009* 4	0.110* 6
19	3.180	(2)	$(5/2^+)$	-	0.068* 5
20	3.245	(2)	$(5/2^+)$	-	0.035* 4

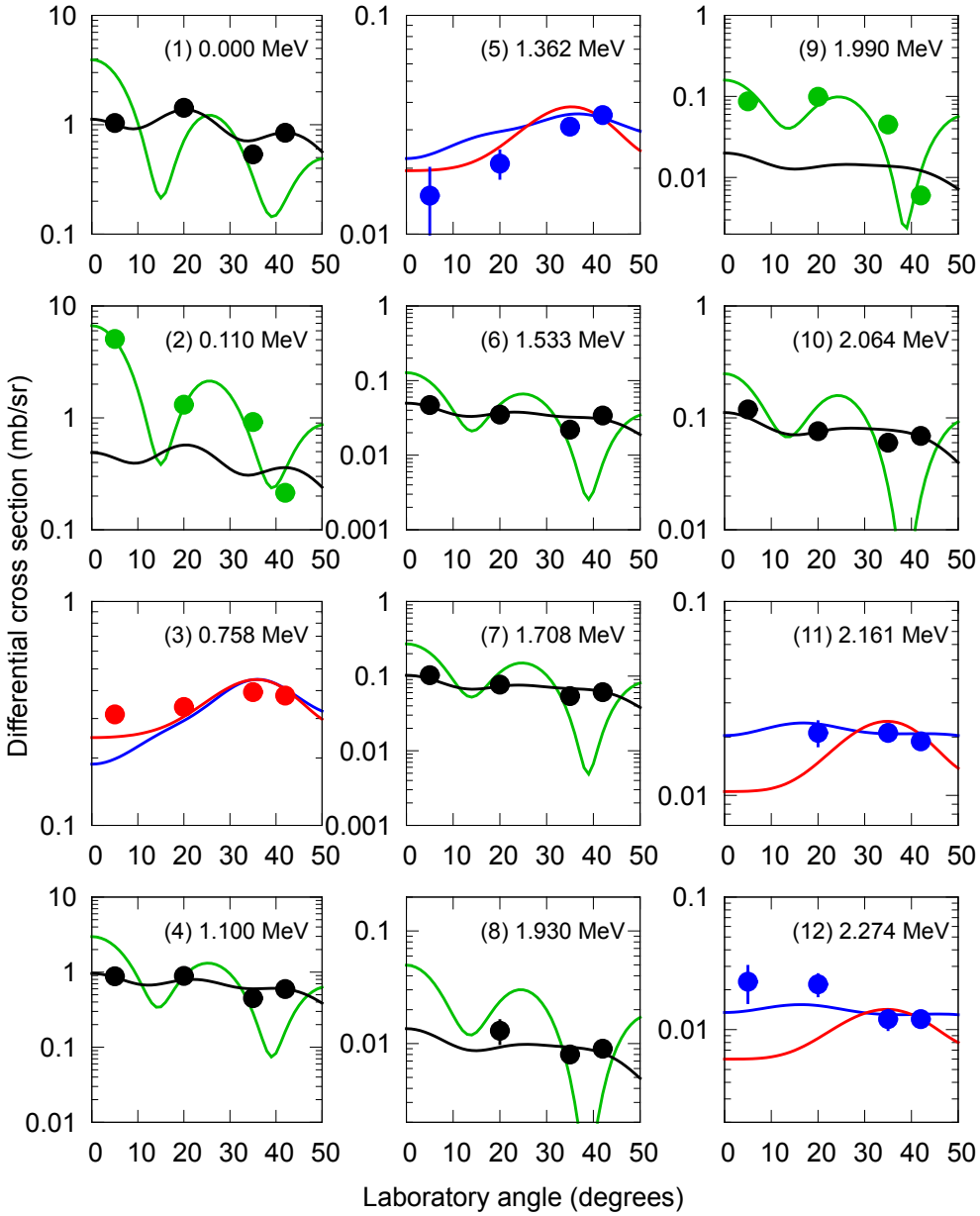

Figure 4.20: Angular distribution of cross sections in the (p,d) reaction for states 1 to 12 observed in ^{143}Sm. DWBA calculations are shown for ℓ=0 in green, ℓ=2 in black, ℓ=4 in blue and ℓ=5 in red. The data points are coloured according to the assignment made. All cross sections are in the lab frame.

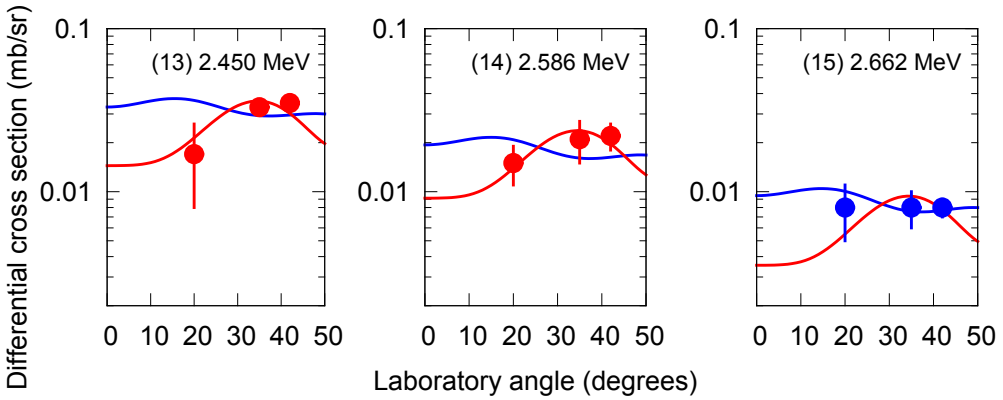

Figure 4.21: Angular distribution of cross sections in the (p,d) reaction for states 13 to 15 observed in ^{143}Sm. DWBA calculations are shown for ℓ=0 in green, ℓ=2 in black, ℓ=4 in blue and ℓ=5 in red. The data points are coloured according to the assignment made. All cross sections are in the lab frame.

CHAPTER

FIVE

THE N=81 ISOTONES

The purpose of this chapter is to interpret the results presented in the previous chapter, with the aim of determining single-particle properties. Before continuing, however, it is informative to first consider both the reliability of the measured spectroscopic factors and the uncertainties associated with them.

The relative spectroscopic factors from the two reactions studied are found to be largely consistent, although there are some discrepancies. Many of these can be attributed to either uncertainties introduced through the DWBA analysis, discussed below, or to states being masked in one reaction by more strongly populated states at similar excitation. In cases where neither of these explanations is satisfactory, the differences may be a result of the approximations made in the DWBA becoming invalid.

There is nearly an order of magnitude difference in the spectroscopic factors between reactions for the lowest $s_{1/2}$ state in all four isotones. This is likely a result of the (^{3}He,α) reaction being poorly matched for the population of these $\ell = 0$ states (see Chapter 2 for details), which results in a small DWBA cross section (see Fig. 2.5). If the measured cross section is dominated by non-direct processes, not considered in the DWBA, the resulting spectroscopic value is physically meaningless. In these circumstances a poor

reproduction of the angular distribution would be expected, however $\ell = 0$ were not observed in (^{3}He,α) at angles other than 15° so this check cannot be made. Distributions were obtained in (p,d) and these were accurately reproduced by DWBA calculations (see Chapter 4 for example plots), as would be expected for a well-matched reaction.

The (^{3}He,α) reaction is also poorly matched for $\ell = 2$ transfer, although to a lesser extent than for $\ell = 0$. The mismatch is greatest at large reaction Q-values and results in a factor of more than two difference in spectroscopic factors for the ^{137}Ba ground state ($Q \simeq 12$ MeV). At lower Q this agreement improves and the values for the ^{143}Sm ground state ($Q \simeq 10$ MeV) are found to differ by only ∼20%. Spectroscopic factors from the (p,d) reaction are used in all subsequent discussion of states populated through $\ell = 0$ and $\ell = 2$.

The spectroscopic factors for states populated through $\ell = 4$ and $\ell = 5$ transfer are generally found to be in agreement to within ∼20%, and most discrepancies can be attributed to the masking of states in (p,d) by stronger low-ℓ states. The momentum mismatch in (p,d) becomes apparent for low-lying states in ^{137}Ba, where the reaction Q-value is least negative, and a factor of ∼2 is found in spectroscopic factors. It is noted that the values from the better-matched (^{3}He,α) reaction are expected to be the more robust for all high-ℓ states, and hence they are given greater weight in the discussion below.

5.1 Uncertainties in spectroscopic factors

The uncertainties in measured cross sections, discussed in Section 4.3, translate directly into uncertainties in the spectroscopic factors. It is worth noting that if relative spectroscopic factors are used, only the relative error in cross sections is relevant since any systematic contributions are absorbed in the normalisation coefficient. Additional uncertainties arise from the choice of both optical and bound-state potentials used in the DWBA analysis. Associating a value with these uncertainties is non-trivial; there exist a large number of potentials in the literature fitted to different subsets of the avail-

able reaction data.

An attempt has been made to quantify these uncertainties by repeating the DWBA analysis with alternate potentials, fitted to data including reaction conditions similar in mass and energy to those used here. The optical potentials considered are given in Table 5.1.

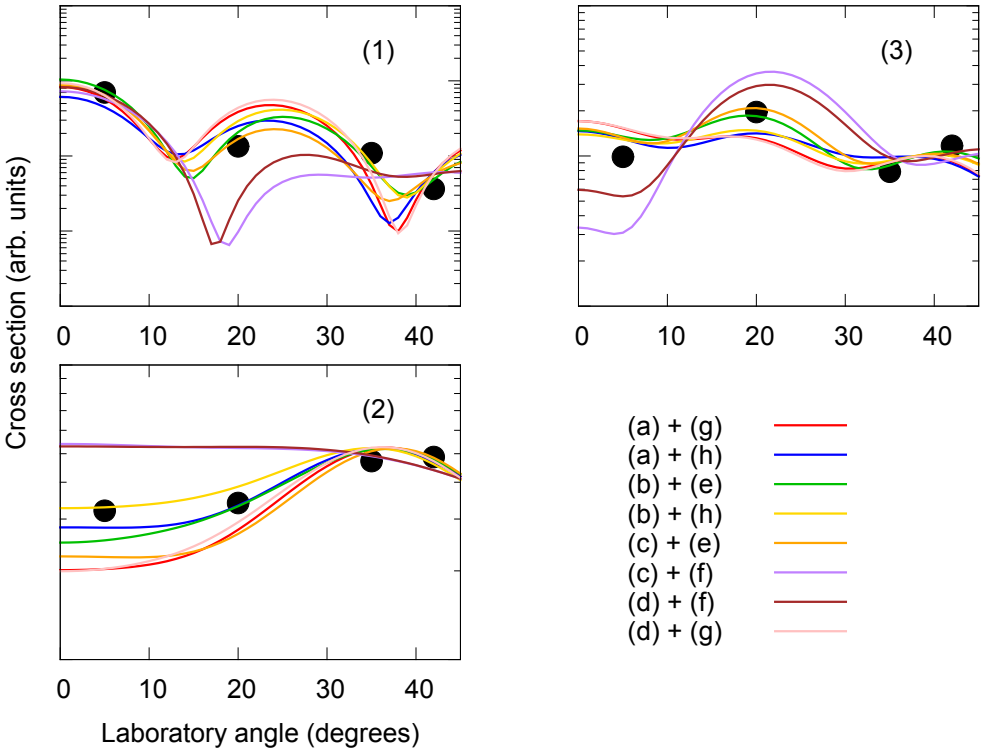

Figure 5.1: Fits of DWBA calculations using various optical-model potentials to the data for low lying transitions in ^{141}Nd. The data show (1) ℓ=0, (2) ℓ=2 and (3) ℓ=5. The potentials used are given in Table 5.1.

To assess the validity of the potentials tested, calculated angular distributions were compared to strong states of known L-transfer. Examples of these fits are shown for (p,d) in Fig. 5.1 and for (^{3}He,α) in Fig. 5.2. With reference to Fig. 5.1 it is apparent that calculations using deuteron potential (f) do not reproduce the observed distributions. On this basis it is is excluded from the subsequent analysis. The remaining potentials, including all those for (^{3}He,α), reproduce the data adequately and so are included.

For both sets of reaction data, a variation of $\sim$20% in absolute spectro-

Table 5.1: Optical-model potentials from the literature for (a) - (d) protons, (e) - (h) deuterons, (A) - (D) ^{3}He and (E) - (H) α particles. Global potentials are evaluated for the population of a 1 MeV state in ^{141}Nd to aid comparison.

	Real			Spin-orbit			Vol. imag.			Surf. imag.				
Potential	V	r_0	a_0	V_{SO}	r_{SO}	a_{SO}	W	r_W	a_W	W_D	r_D	a_D	r_C	source
(a)	55.22	1.17	0.75	6.2	1.01	0.75	2.36	1.32	0.63	8.11	1.32	0.63	1.30	[50]
(b)	49.75	1.25	0.65	7.5	1.25	0.47	-	-	-	13.5	1.25	0.47	1.25	[41]
(c)	53.83	1.16	0.75	6.04	1.06	0.78	3.27	1.37	0.73	5.71	1.37	0.72	1.25	[51]
(d)	52.84	1.21	0.69	5.9	1.1	0.63	1.2	1.25	0.69	8.93	1.25	0.69	1.26	[52]
(e)	100.89	1.15	0.81	-	-	-	-	-	-	17.85	1.34	0.68	1.15	[42]
(f)	116.49	1.05	0.86	7	0.75	0.5	-	-	-	8.05	1.43	0.35	1.30	[53]
(g)	94.95	1.17	0.73	3.21	1.07	0.66	0.25	1.33	0.84	12.32	1.33	0.84	1.30	[54]
(h)	94.04	1.2	0.56	-	-	-	-	-	-	11.24	1.34	0.82	1.30	[55]
(A)	135	1.38	0.58	-	-	-	21	1.38	0.58	-	-	-	1.3	[45]
(B)	156	1.36	0.72	-	-	-	40	1.43	0.84	-	-	-	1.4	[56]
(C)	170.5	1.14	0.72	-	-	-	17.5	1.6	0.86	-	-	-	1.25	[57]
(D)	152	1.24	0.69	-	-	-	23	1.43	0.87	-	-	-	1.3	[43]
(E)	207	1.3	0.65	-	-	-	28	1.3	0.52	-	-	-	1.3	[44]
(F)	181.1	1.32	0.62	-	-	-	15.13	1.35	0.85	-	-	-	1.3	[58]
(G)	189.1	1.31	0.62	-	-	-	24.2	1.44	0.62	-	-	-	1.4	[59]
(H)	185	1.4	0.52	-	-	-	25.8	1.33	0.49	-	-	-	1.4	[60]

scopic factors is found between the various combinations of optical potentials. The relative variation in spectroscopic factors is significantly lower at ∼5%. This illustrates both the problems associated with quoting absolute spectroscopic factors, and the dangers of making direct comparisons between results from different analyses. Relative values, on the other hand, are found to be less sensitive to the choice of potentials used.

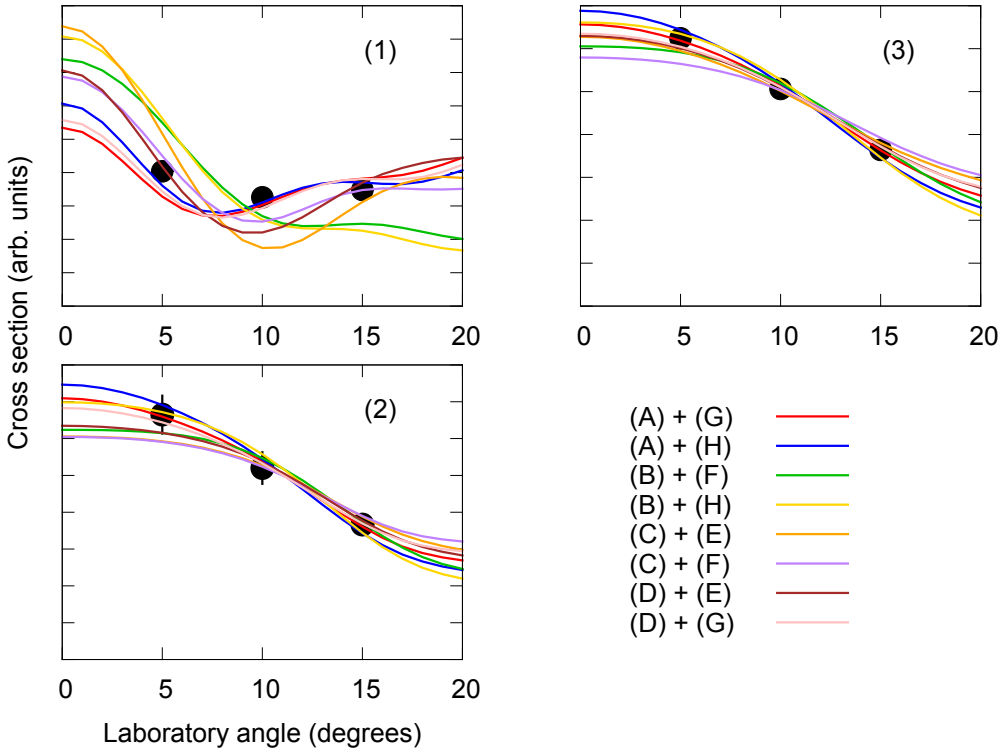

Figure 5.2: Fits of DWBA calculations using various optical-model potentials to the data for transitions in ^{137}Ba. The data show (1) ℓ=2, (2) ℓ=4 and (3) ℓ=5. The potentials used are given in Table 5.1.

A similar assessment was performed for the bound-state parameters (see Table 4.1). The nucleon bound state is assumed to be the eigenfunction of a Woods-Saxon potential with a spin-orbit contribution. The depth of this potential is adjusted such that the energy eigenvalue matches the experimentally-measured binding energy. As the form of the angular distribution is relatively insensitive to the remaining parameters, other experimental observables are required to fix their values.

The target bound-state radii and diffuseness are conventionally given values of ∼1.25 and ∼0.65, respectively, since these are found to give spectroscopic factors consistent with sum-rule limits near closed shells [61]. Given that these parameters control the extent of the nucleon wave function, and that transfer reactions are surface-dominated processes, it is unsurprising that the DWBA cross section is strongly affected by their magnitudes. The dependence on bound-state radius is illustrated in Fig 5.3. An increase in r_0 of 5% results in a 50% increase in cross section, and hence an equivalent decrease in the spectroscopic factor. Meanwhile the relative cross sections vary by only ∼10% over the same range, again proving to be far less sensitive to such choices. With reference to Fig. 5.3, the variation due to the projectile bound-state parameters is small in comparison.

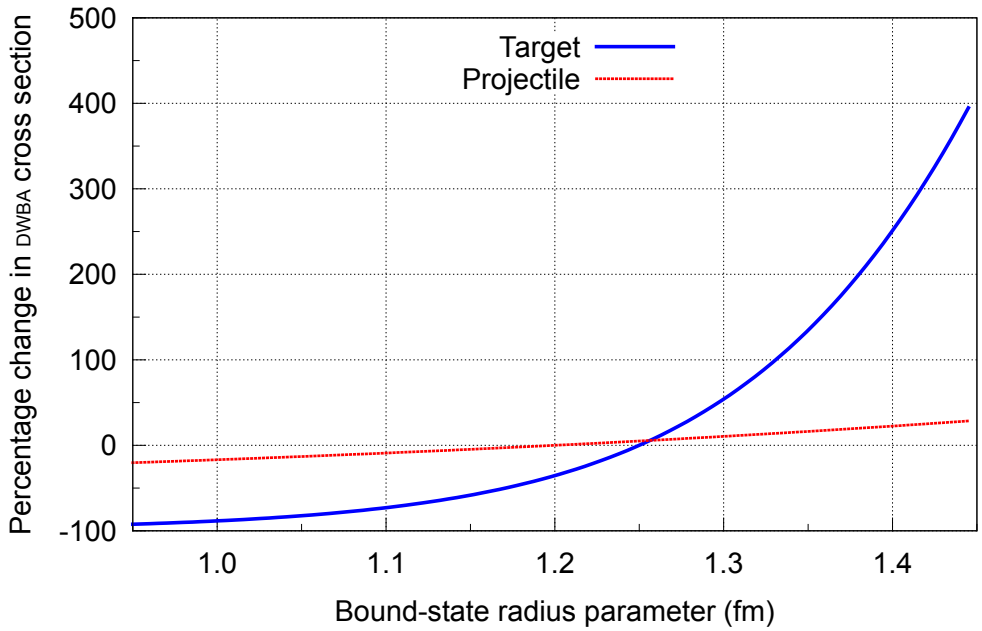

Figure 5.3: The percentage change in DWBA cross section for populating an $\ell = 4$ state in the (^{3}He,α) reaction as a function of the projectile and bound-state radius parameters (relative to the values given in Table 4.1).

The spin-orbit component of the bound-state potential has historically received somewhat haphazard treatment. The effect it has is opposite for states with $j = \ell + s$ and $j = \ell - s$, acting to increase the radial extent of the wave

function in the former case and decrease it in the latter, affecting the DWBA cross sections similarly. The magnitude of this change increases with ℓ, but is also a function of the spin-orbit geometry, and an often neglected feature is that the spin-orbit force peaks inside the radius of the central potential. The change in potential produced by instead using the same geometry for both components is shown in Fig. 5.4. As the radius and diffuseness of the spin-orbit force are increased, the potentials for $j_>$ and $j_<$ states become less distinct, quenching the effects of the interaction.

The parametrisation of the spin-orbit geometry used here (see Table 4.1) is based in part upon polarisation data from the elastic scattering of both protons [62–64] and ^{3}He ions [65]. These measure the nucleon optical-potentials, which should reflect the nucleon bound-state potentials. Although at low energies elastic scattering may not probe the nuclear interior, both nucleon-transfer and the spin-orbit force are surface-localised features. Fits of these data consistently yield values for $r_{SO} \gtrsim 10\%$ lower than the central equivalent.

Detailed analyses of relative high-ℓ $j_>$ and $j_<$ strengths around shell closures provide further insight. These include, for example, transfer data on ^{208}Pb [66], N=82 [12] and Z=50 [10]. In each case it is found that a reduction in the spin-orbit geometry of $\sim$10% relative to the central well gives consistent strength between orbitals. The bound-state parameters used here are the same as those in Ref [10] in which the $\pi g_{7/2}$ and $\pi h_{11/2}$ single-particle properties were measured. It should also be noted that this change in spin-orbit geometry has a robust theoretical underpinning, and is not introduced merely as a convenience. In Brueckner many-body theory the effect arises due to the strong density-dependence of the spin-orbit force, while the central force saturates at nuclear densities [67].

Relative spectroscopic factors are therefore sensitive to choices regarding the parametrisation of the spin-orbit component of the bound-state. An appreciation of this is gained by considering the DWBA cross section as a function of r_{SO}, shown in Fig. 5.5. As expected, the variation is greatest, and opposite, for the high-ℓ $g_{7/2}$ and $h_{11/2}$, and non-existent for the $\ell = 0$

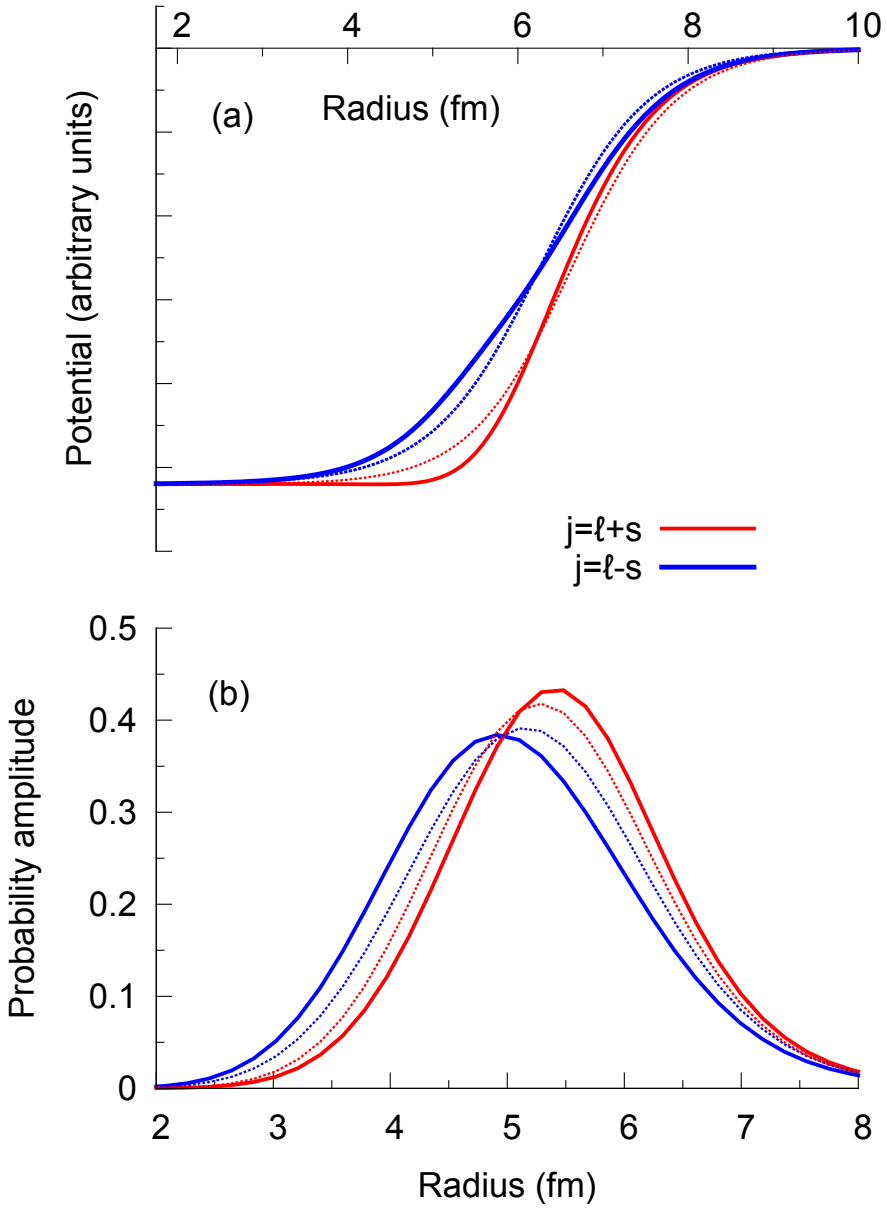

Figure 5.4: The form of the bound-state potential for $j = \ell + s$ ($h_{11/2}$) and $j = \ell - s$ ($g_{7/2}$) states is shown in (a) and the resulting wave functions are shown in (b). The solid lines indicate the potential when the spin-orbit radius and diffuseness parameters are reduced relative to the central well. The dashed lines give the potential when identical geometries are used.

$s_{1/2}$.

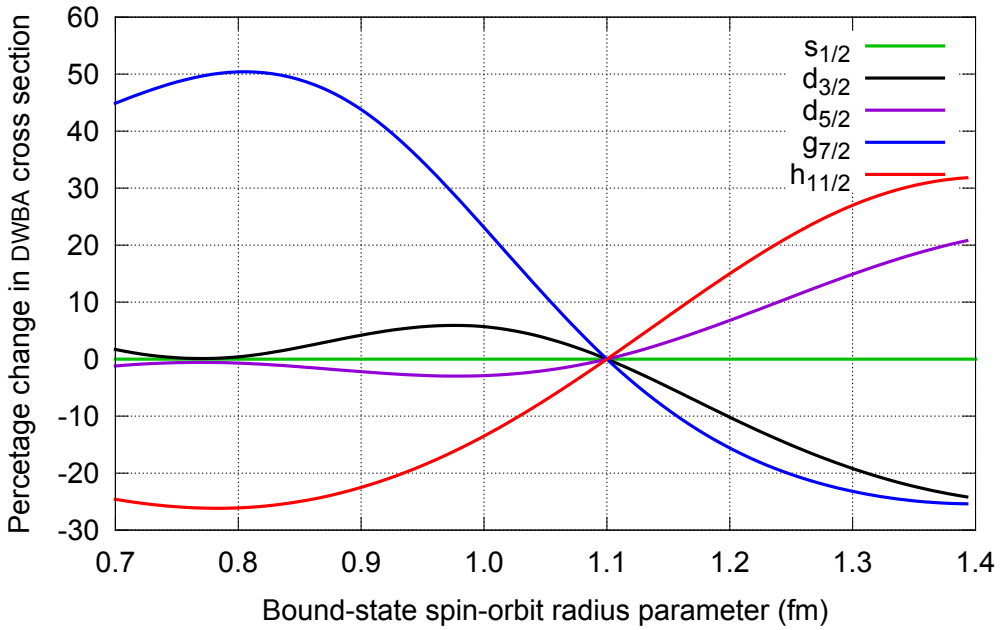

Figure 5.5: The percentage change in DWBA cross section due to changing the bound-state spin-orbit radius parameter r_{SO} from the adopted value of 1.10 fm (see Table 4.1).

In summary, the relative spectroscopic factors quoted have uncertainties of ∼15% associated with them as a result of both experimental uncertainties and the choice of parameter sets in the DWBA analysis. An additional uncertainty in relative $j_>$ and $j_<$ spectroscopic factors is introduced by the choice of bound-state spin-orbit geometry.

5.2 Observed single-particle strength

The spectroscopic sum-rules introduced in Chapter 2 provide a further consistency check. The major shell closure at N=82 produces a Fermi-surface with all orbitals beneath it fully occupied. This is confirmed by the non-observation of states corresponding to neutron-removal from levels above this shell gap. Furthermore, there is no indication of states below the N=82 shell closure being populated through neutron adding reactions on the same N=82 isotones [68,69]. Therefore while the low-lying structure may vary across the

isotones studied, the summed spectroscopic factors should not. These are plotted in Fig. 5.6(a) for (p,d) and Fig. 5.6(b) for (^{3}He,α). A combined sum is given for $d_{3/2}$ and $d_{5/2}$ since they are both populated through $\ell = 2$ and cannot be distinguished.

In each isotone there are ambiguous states which can not be assigned ℓ. Where these can also not be excluded from having a particular ℓ, they are included in Fig. 5.6 as the shaded regions. The uncertainty these introduce is largest for high-ℓ strength in (p,d), a consequence of the low DWBA cross sections. Taking instead high-ℓ results from the better-matched (^{3}He,α) reaction, the unassigned strength accounts for at most 10% of any single-particle total.

In both reactions the summed-strength is consistent across isotones to within 10%. The drop in high-ℓ strength towards ^{137}Ba in (p,d) is attributed to the reaction becoming less-well matched as the Q-value approaches zero. The trend is not mirrored in the (^{3}He,α) data. The variation between different j is greater, but excluding $g_{7/2}$ is at approximately the 15% level expected. The discrepancy in $g_{7/2}$ strength, observed in both reactions, suggests that either a systematic bias exists in the DWBA analysis or that not all strength is observed. The only aspect of the DWBA analysis found to significantly affect relative strength is the bound-state spin-orbit parametrisation. To reconcile the total $g_{7/2}$ and $h_{11/2}$ strength would require an increase in r_{SO} to $\sim$1.3 fm, beyond the radius of the central well. There is no basis for such a prescription and so the alternative, that not all strength is accounted for, must be considered.

'Missing' $g_{7/2}$ strength

Near shell-closures states of strong single-particle character are generally expected, and in the N=81 isotones they are found below 1 MeV for the $s_{1/2}$, $d_{3/2}$ and $h_{11/2}$ orbitals. However, the more deeply-bound $d_{5/2}$ and $g_{7/2}$ are found to be fragmented into numerous weak states. This is perhaps un-

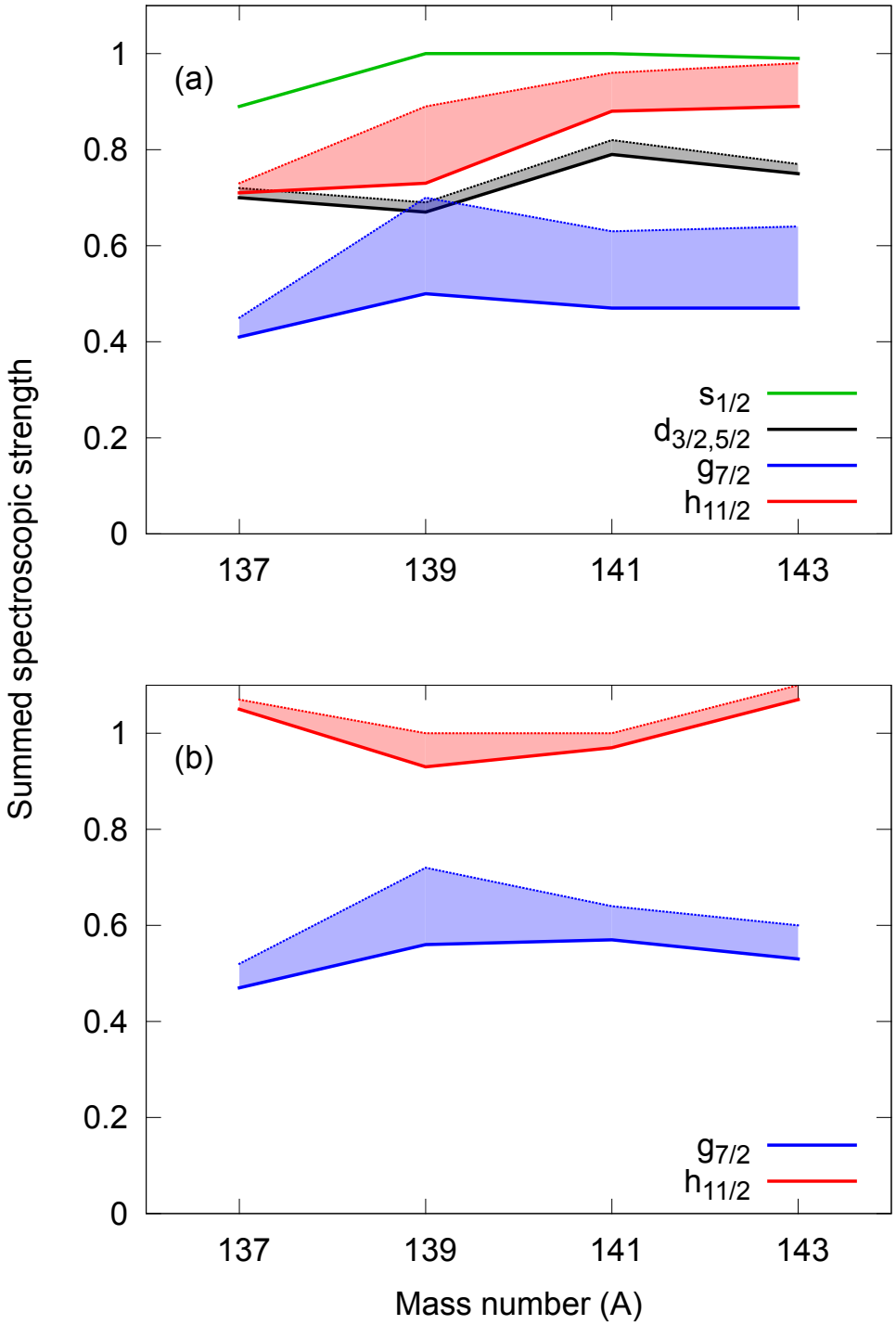

Figure 5.6: Summed spectroscopic strengths for transfer to each of the N=81 isotones studied using data from (a) (p,d) and (b) (^{3}He,α). The solid lines represent states of assigned ℓ and the shaded regions the effect of including additional unassigned, discrete states. The $\ell = 2$ strength is normalised using the total occupancy of both $d_{3/2}$ and $d_{5/2}$ orbitals.

surprising; they have natural-parity, low-medium spin and are in a region of higher level density resulting in a large number of states with which they can mix. The fragmentation has been attributed primarily to the coupling of neutron single-hole motion to surface-vibrations of the N=82 core. Unified-model calculations have been performed which include the effects of up to three quadrupole-phonon vibrations [70], and these are compared to the experimental results in Fig. 5.7.

With reference to Fig. 5.7, particle-vibration coupling does appear to be a potential mechanism for the fragmentation of single-particle strength in N=81 nuclei. There appears to be a generally reasonable description of the global features of the strength distribution by what are probably best described as schematic models. The complexity of the real situation is such that these models are unlikely to give a good state-by-state comparison since they concentrate on a subset of the real degrees of freedom, excluding octupole vibrations for example. It is noted that similar models including octupole degrees of freedom do a fairly good job of describing the fragmentation of single-particle strength in N=83 nuclei (see Ref. [12] and references therein), although the fragmentation of the high-j particle strengths is much less than in the present case.

A remaining question to be addressed is the location of the missing $g_{7/2}$ strength. One potential source is the 'background' under the discrete peaks in the ejectile-ion spectra (see Section 4.4). Since the identification of the individual ions groups is relatively good (see Fig. 4.1), the contribution to these counts from true background, in the form of ions of other species from different reactions, is likely to be low. It is likely that this background is actually composed of multiple, weak transfer peaks that form an unresolved smooth component under the discrete peaks. It might therefore be speculated that the missing $g_{7/2}$ strength is located, at least in part, in this background of states. To assesses the plausibility of this hypothesis, an analysis of the background in each spectrum was performed. The cross section was integrated in bins of 0.5 MeV width between 2 and 3.5 MeV, and that associated with dis-

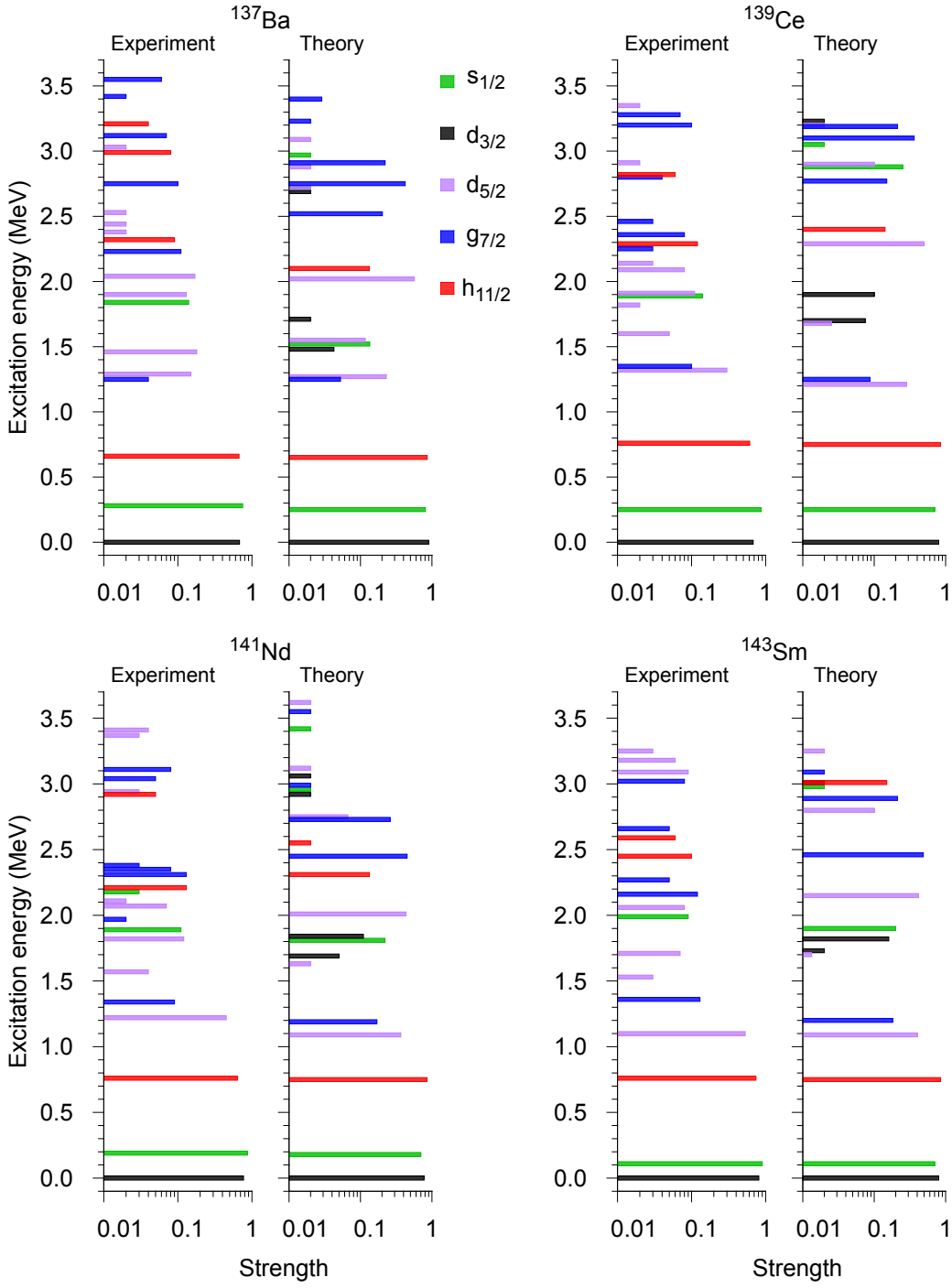

Figure 5.7: A comparison of the states measured experimentally with those calculated in Ref. [70].

crete states subtracted. An identical DWBA analysis to that described previously was used to determine the maximum single-particle strength contained in the background. The results are in Table 5.2. For (^{3}He,α) a weighted average over all angles is given. For (p,d) the value from 42° is used, since at more forward angles even some known states cannot be distinguished from the background.

Table 5.2: The relative spectroscopic factor of the background between 2 and 3.5 MeV at 42° in (p,d) and averaged over all angles in (^{3}He,α) assuming it to be pure single-particle strength.

	$d_{5/2}$		$g_{7/2}$		$h_{11/2}$	
Isotone	(p,d)	(^{3}He,α)	(p,d)	(^{3}He,α)	(p,d)	(^{3}He,α)
^{137}Ba	0.13 1	1.32 2	0.61 2	0.52 1	0.35 1	0.21 1
^{139}Ce	0.12 1	1.18 2	0.57 3	0.63 2	0.32 2	0.26 1
^{141}Nd	0.16 1	0.95 2	0.74 4	0.58 1	0.41 2	0.26 1
^{143}Sm	0.28 1	0.74 2	1.26 3	0.54 1	0.66 2	0.26 1

Table 5.2 gives estimates of the single particle strength of the underlying background of states, based on the assumption that they all arise from the same single-particle parentage. If $\ell = 2$, this continuum of states is only weakly populated in (p,d) and contributes little to the overall strength; but in (^{3}He,α), as low-ℓ strength is so mismatched, attribution to $\ell = 2$ would likely violate the overall sum rule. The strength on the assumption of high-ℓ transfer in (^{3}He,α) is likely to give enough strength for $\ell = 4$ to make up for the strength not observed in discrete states. It is noted that the values in Table 5.2 for the high-ℓ states in (p,d) are less reliable as these states are not only intrinsically weak, but also mismatched in this reaction; the assumption of direct population, upon which DWBA calculations rely, is easily questioned.

There does appear to be sufficient strength in the spectra outside of the main discrete peaks to account for the missing $\ell = 4$ strength in the background due to weak, unresolved states. Quantitative attribution of this strength between different ℓ is extremely difficult, but as an indication, the angular distribution of the background strength was constructed and is shown in Fig. 5.8, compared to predictions for $\ell = 2$, 4 and 5. Somewhat surpris-

ingly, given the difficult nature of the analysis, the resulting distribution appears to be reproduced best by an $\ell = 4$ distribution. $\ell = 2$ contributions appear to be small given the persistence of yield at 10°, with $\ell = 4$ favoured due to the gradient of the overall distribution. One might speculate that the background strength in the distribution may be dominated by $\ell = 4$, consistent with the hypothesis that unobserved $\ell = 4$ strength is contained in the underlying background of weaker states. It should be stressed that, given the uncertainties in the analysis of the background, such a conclusion should remain speculative.

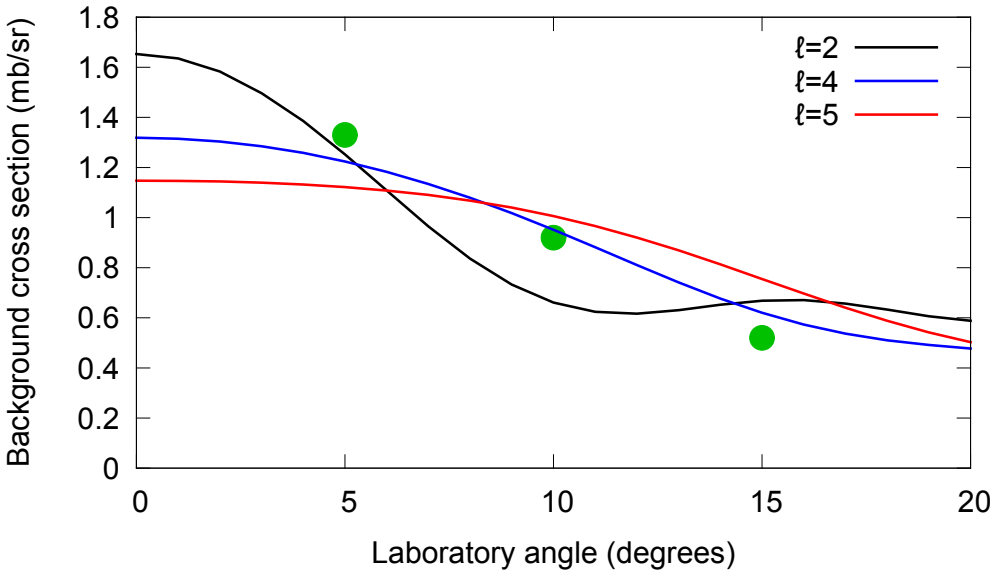

Figure 5.8: The total background cross section between 2 and 3.5 MeV excitation in the ^{138}Ba(^{3}He,α)^{137}Ba reaction compared to DWBA calculations for different ℓ. The errors on the data are smaller than the points drawn.

$\ell = 2$ strength

An additional feature of interest in the unified-model calculations shown in Fig. 5.7 are the excited $3/2^+$ states predicted. Previous studies of the N=81 isotones have followed the convention established in Ref. [14] that the entire $d_{3/2}$ strength is exhausted in the ground state, and therefore all other $\ell = 2$ states carry $d_{5/2}$ strength.

The analysis performed here, using a realistic bound-state spin-orbit geometry, suggests the ground state in fact accounts for between 70% and 80% of the $d_{3/2}$ strength. The uncertainties associated with the spectroscopic factors mean this does not necessarily exclude the ground-state carrying the full strength. Taken in conjunction with the unified-model calculations, however, it does suggest that a more careful treatment of the $\ell = 2$ strength is required. In the absence of ejectile polarisation measurements to distinguish $j_>$ and $j_<$ states, little more can be said on this matter at present.

Single-particle energies

The centroid of observed strength for each orbital gives an approximation of the underlying single-particle energy. Formally this is written as

$$E_{sp} = \frac{\sum E_i S_i}{\sum S_i}, \tag{5.1}$$

where E_i are the energies of each fragment and S_i the relative spectroscopic factors. The calculated energies are most robust when the full single-particle strength is accounted for. A summary of the spectroscopic-strength observed in each isotone and the calculated single-particle energies are given in Tables 5.3 and 5.4, respectively. The binding energy associated with each single-particle orbital is plotted in Fig. 5.9.

Table 5.3: Summed spectroscopic factors, normalised according to Eqn. 4.6. Values from (p,d) are given for the low-ℓ $s_{1/2}$ and $d_{3/2,5/2}$ and from (^{3}He,α) for the high-ℓ $g_{7/2}$ and $h_{11/2}$. The quoted uncertainties are statistical.

Isotone	$s_{1/2}$	$d_{3/2}$	$d_{5/2}$	$g_{7/2}$	$h_{11/2}$
^{137}Ba	0.89 1	0.68 1	0.71 2	0.47 3	1.05 1
^{139}Ce	1.00 2	0.68 1	0.66 2	0.56 3	0.93 1
^{141}Nd	1.00 2	0.77 1	0.81 2	0.57 2	0.97 1
^{143}Sm	0.99 2	0.81 1	0.71 2	0.53 2	1.07 1

Table 5.4: Single-particle energies, in units of MeV, calculated according to Eqn. 5.1 based upon the observed strength. The known $d_{3/2}$ strength in each isotone is taken to be entirely in the ground state, see text for details. The quoted uncertainties are statistical.

Isotone	$s_{1/2}$	$d_{5/2}$	$g_{7/2}$	$h_{11/2}$
^{137}Ba	0.52 1	1.72 6	2.70 16	1.17 2
^{139}Ce	0.47 1	1.75 10	2.34 14	1.13 2
^{141}Nd	0.43 1	1.68 7	2.33 8	1.12 2
^{143}Sm	0.28 1	1.35 5	2.16 9	1.06 2

5.3 Discussion

The aim of this work has been to investigate the single-particle properties of the high-j neutron strength below the N=82 shell closure. The motivation comes from recent theoretical work which has highlighted the important role played by the tensor force in shell-evolution. Its properties have been described and are proposed to be both a general and robust feature of nuclear structure. In particular it is predicted to generate localised, relative shifts between high-ℓ $j_>$ $j_<$ partners coinciding with the filling of high j orbitals of opposite isospin.

Proton transfer data shows the $\pi g_{7/2}$ orbital increasing in occupancy across the N=81 isotones (see Fig. 1.7). This should result in an increasingly attractive tensor interaction with the $\nu h_{11/2}$ orbital, pulling it down in energy, and an increasingly repulsive interaction with $\nu g_{7/2}$, making it relatively less bound. It is noted that there is a parallel increase in $\pi d_{5/2}$ occupancy measured, the effect of which is opposite to that just described. The interaction is expected to be considerably weaker in this case however as a result of both reduced radial overlap (see Fig. 1.9) and lower ℓ.

It is assumed that the similarity in radial shape between the $g_{7/2}$ and $h_{11/2}$ orbitals mean that global energy-trends resulting from the changes in nuclear radius and the central component of the nucleon-nucleon interaction largely cancel between them. Changes in their energy separation can therefore be attributed to the effects of the tensor interaction. The energy difference

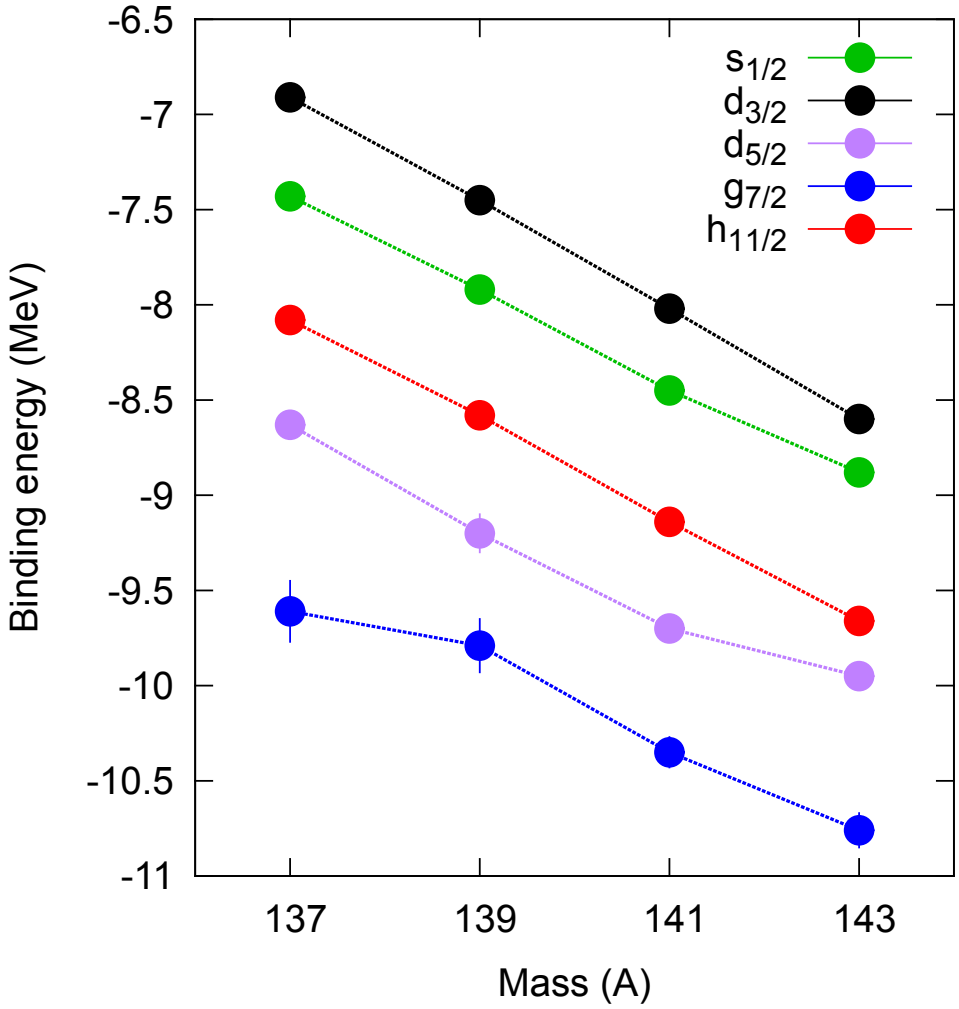

Figure 5.9: Neutron single-particle binding energies based upon the centroids of observed strength.

between the centroids of observed strength $E(\nu g_{7/2}) - E(\nu h_{11/2})$ is shown in Fig. 5.10. The trend observed, whilst not conclusive, is in *qualitative* agreement with the expected action of the tensor force.

In comparing the $g_{7/2}$ and $h_{11/2}$ energies an implicit assumption has been made that the energy centroid of the 'missing' $g_{7/2}$ strength does not change. This assumption is somewhat strengthened by the observation that the same fraction is missing in each isotone, and that this same fraction can be accounted for by 'background' strength up to 3.5 MeV. Without directly observing this missing strength, however, it cannot be confirmed that this as-

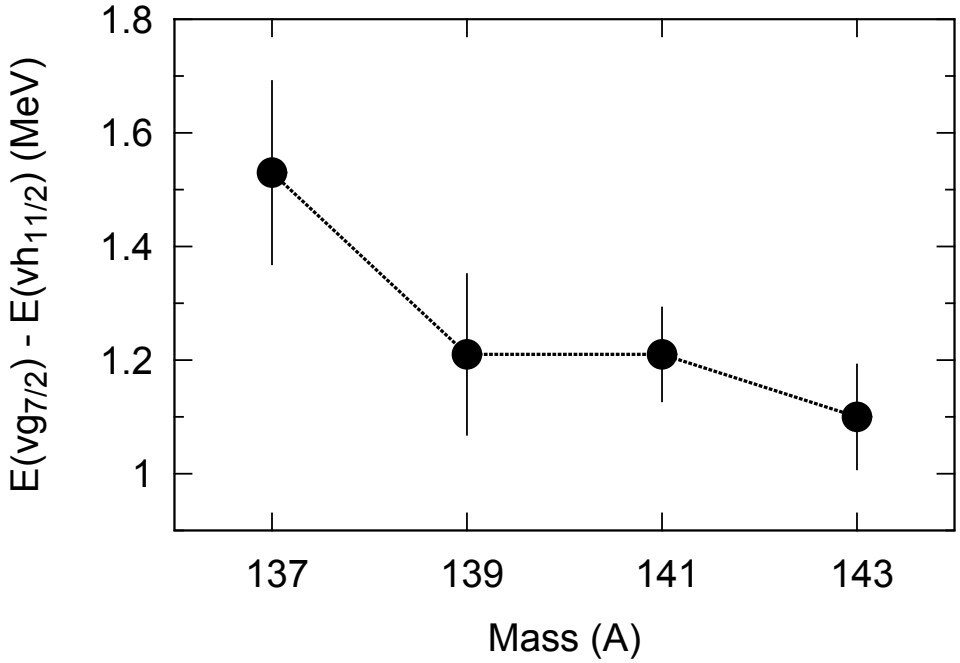

Figure 5.10: The difference in centroid energies of $\nu g_{7/2}$ and $\nu h_{11/2}$ strength.

sumption is valid and so any discussion of the observed trends must remain speculative.

CHAPTER

SIX

CONCLUSIONS

The neutron-removal reactions (p,d) and (^{3}He,α) have been used to study single-hole strength in the N=81 isotones ^{137}Ba, ^{139}Ce, ^{141}Nd and ^{143}Sm. States populated were observed through a momentum analysis of the ejectile ions. Careful cross section measurements have been made at multiple angles, chosen to be sensitive to the transferred angular momentum. The identities of states populated were deduced by comparing angular distributions and cross-reaction ratios to DWBA calculations. A DWBA analysis was performed to determine the relative spectroscopic strength carried by each state.

The motivating interest for this work has been the study of high-j strength, and the residual monopole-shifts arising from changing nuclear forces as valence protons are added. Of particular interest is the effect of the tensor force, which has been isolated as driving localised shifts in high-j centroids [6, 8]. A summary of the relevant results is presented in Fig. 6.1. A discrepancy between the total $g_{7/2}$ and $h_{11/2}$ strength has been observed, shown in Fig. 6.1(a). It has been speculated that the $g_{7/2}$ strength has become sufficiently fragmented for a large fraction (up to 50%) to form an unresolved background continuum. The behaviour of the background strength between 2 and 3.5 MeV in each isotone does not contradict this hypothesis.

A speculative interpretation has been made under the assumption that

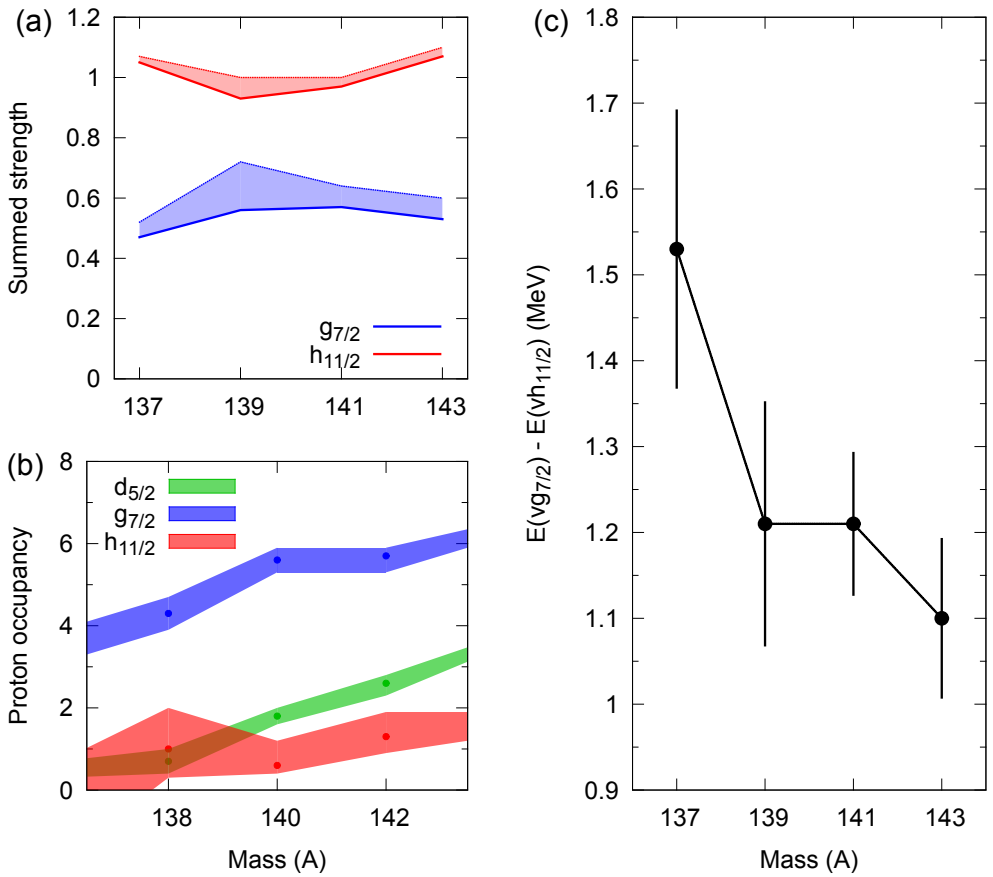

Figure 6.1: A summary of results concerning high-j strength in the N=81 isotones. (a) The summed strength observed in (^{3}He,α), (b) proton occupancies across N=82 [13] and (c) the energy splitting of the $g_{7/2}$ and $h_{11/2}$ neutron orbitals based upon the observed strength.

the observed centroids of $g_{7/2}$ strength reflect, at least on a relative scale, the real centroids. The proton occupancies in the N=82 nuclei are known through single-proton transfer studies [13], and are shown in Fig. 6.1(b). The filling of the $\pi g_{7/2}$ orbital is expected to give rise to opposing tensor forces for the neutron $g_{7/2}$ and $h_{11/2}$ orbitals [6, 8], leading to a relative increase in binding for the isospin-flip $\nu h_{11/2}$. The reverse trend is expected due to the filling also of $\pi d_{5/2}$, however the dependence on radial overlap leads to the expectation that the effect due to the $\pi g_{7/2}$ will dominate for the nodeless high-j states (see Fig. 1.9). A comparison of the energy centroids is in Fig. 6.1(c), and the trend observed is in qualitative agreement with the expected action of the tensor force. However, we stress the speculative nature of this

part of the analysis.

6.1 Future work and outlook

To satisfactorily complete the study of N=81 strength a more careful examination of $g_{7/2}$ strength is required. In the present work the low resolution of (^{3}He,α) spectra, and inherently weak population of high-j strength through (p,d), have complicated the identification of weak $g_{7/2}$ fragments. It would be of interest to repeat the (^{3}He,α) measurements using a spectrometer offering greater resolving power. This should be possible using, for example, the Q3D spectrograph at TU München (see Fig. 6.2(a)), where an energy resolution $E/\Delta E = 6000$ is attainable, corresponding to resolution <10 keV for the reactions of interest [71]. In practice this resolution is likely to be limited by energy losses within the target, but nonetheless it should be sufficient to resolve individual states within the background, and hence confirm their $7/2^+$ character.

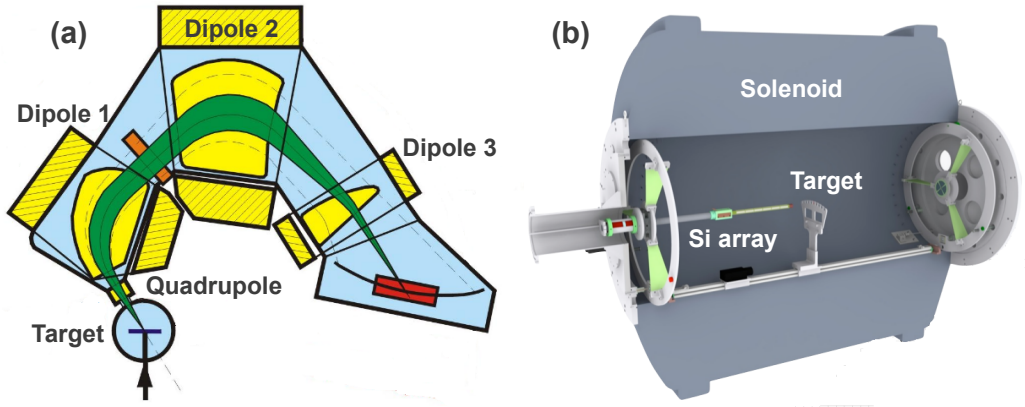

Figure 6.2: Two facilities with potential for expanding upon the present work. (a) The Q3D spectrometer at TU München has an energy resolution of $E/\Delta E \sim 6000$ in traditional light-ion reactions [72]. (b) The Helios spectrometer at Argonne National Laboratory for use in inverse kinematics, including with radioactive beams provided by the CARIBU fission source [73].

Another attractive feature of the Munich facility is the opportunity to produce polarised deuteron beams. The lack of excited $3/2^+$ states reported

in previous studies [14, 17] has been ascribed here to a haphazard treatment of bound-state spin-orbit parameters. The result is exaggerated $j_<$ strengths, which applies also to $g_{7/2}$. The asymmetry in angular distributions from (d,t) measurements using a polarised beam should enable unambiguous assignment of $3/2^+$ and $5/2^+$ states. It is expected from the results of the present analysis, and also the unified-model predictions shown in Fig. 5.7, that at least one additional $3/2^+$ state be identified at low excitation. The lower terminal voltage attainable with the Munich tandem, of 14 MV relative to 22 MV at Yale, is not an issue due to the Q-value for (d,t) also being some 4 MeV less negative than for (p,d). On a side note, the usefulness of published cross section data is stressed here, since the reliability of spectroscopic factors depends entirely on the DWBA prescription adopted.

The scope of the present work has been limited to those isotones produced from solid, stable targets, a restriction imposed by the experimental technique and facilities. The possibility to extend the study to lower Z now exists, for example using the HELIOS spectrometer recently commissioned at Argonne National Laboratory (ANL) (see Fig. 6.2(b)) [74]. This innovative instrument permits the study of transfer reactions in inverse kinematics inside the bore of a superconducting solenoid magnet. Coupled to the CARIBU fission source, also at ANL, measurements down to $Z = 50$ ought to be possible [75].

The recent interest in the effects of the tensor interaction has stimulated a large volume of experimental work regarding trends in, or orderings of, single-particle energy levels. Much of this work is based upon techniques insensitive to single-particle strength, which as demonstrated here can be quite severely fragmented, even in a system which might be naively expected to consist of a rather robust core. This perhaps serves as a cautionary note regarding the interpretation of single-particle behaviour in the absence of a detailed knowledge of single-particle strengths also.

CHAPTER

SEVEN

NUCLEAR STRUCTURE IN THE ^{132}SN REGION

This chapter describes an exploratory experiment carried out at Laboratori Nazionali di Legnaro (LNL) to determine the feasibility of studying nuclei in the ^{132}Sn region via multi-nucleon transfer reactions. A 926-MeV ^{136}Xe beam was used in conjunction with a ^{238}U target, and the high-resolution magnetic spectrometer PRISMA used to identify the beam-like species produced. Additional data on coincident γ-ray emissions were provided by the CLARA array of clover detectors.

Amongst the issues we wish to address in this study are the relative yields of nuclei produced and the quality of recoil-identification provided by PRISMA. These are both essential knowledge for planning future, more focussed studies. Of secondary interest are more general experimental concerns, for example the target robustness. In this chapter the motivation for studying the ^{132}Sn region is introduced and the relevant experimental details given. The analysis procedure is described in detail and the results presented. Finally, the outlook for further studies in this region, based upon the findings here, are discussed.

7.1 Motivation

Nuclei at double-shell closures are attractive from a nuclear structure perspective due to the highly robust core they possess. The doubly-magic ^{132}Sn nucleus is an excellent example, with no known excited states below 4 MeV excitation [76]. Its neighbouring nuclei provide powerful benchmarks of the spherical shell model. Nuclei with odd particle/hole states outside the core give information on single-particle energies, while those with nucleon/hole-pairs outside the core can help in determining particle-particle matrix elements. The region also lies on the neutron-rich side of stability, of interest with respect to the evolution of shell-structure at increasing isospin.

Of particular interest are shell-model states in the N=83 isotones and Sb isotopes. Studies of high-j strength in these systems are described in Chapter 1, both providing evidence for the action of the tensor force [10,12]. These high-j states are virtually unknown in the vicinity of ^{132}Sn. The $\nu i_{13/2}$ state, for example, is not reported in N=83 isotones below ^{139}Ba. Where transfer measurements have been made, the energy difference between the $i_{13/2}$ and $h_{9/2}$ neutron strength centroids has the same trend as the energy difference between the lowest $13/2^+$ and $9/2^-$ states, shown in Fig. 7.1 [11]. Even though the tracking of these two is not exact, the trend in the energy difference in the lowest states is useful information on which to base future transfer experiments when the relevant radioactive beams become available.

Preliminary lifetime measurements for the first 2^+ states across the Sn and Te isotopes have been reported with some surprising features observed [77]. The B(E2) value, normally a fingerprint of collective motion, is found to spike in ^{132}Sn, whilst it is anomalously low in ^{136}Te, as shown in Fig. 7.2. These results are reproduced in recent QPRA calculations under the assumption of significantly weakened neutron-pairing energies above N=82 [78]. This should affect also E2 transition rates from the lowest 6^+ and 4^+ states, and hence measurements of these are of current interest.

Multi-nucleon transfer is a more complex process then the single-nucleon

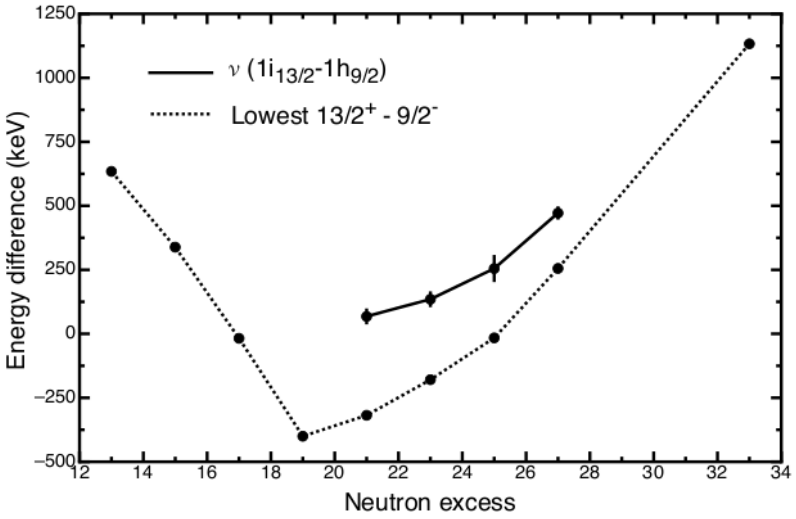

Figure 7.1: The energy splitting of $i_{13/2}$ and $h_{9/2}$ strength in the *N=83* isotones using both centroid energy and the lowest states. Figure from Ref. [11].

transfer mechanism discussed in previous chapters. High-lying states may be directly populated, which subsequently feed a succession of lower-lying states through γ-ray de-excitations (similar to the feeding found in fusion-evaporation reactions). The binary character of the initial system is still maintained, however, with both target and beam-like fragments found in the final system. Multi-nucleon transfer occurs when a 'neck' is formed between colliding nuclei as a result of surface attractions deforming their shapes. If the angular momentum and nuclear charge are sufficiently high, the neck is broken and the fragments separate. During the existence of the neck ($\sim 10^{-22}$ s) a flow of nuclear matter occurs which favours an equilibration of the N/Z ratio between nuclei. A more complete description of the reaction mechanism can be found in, for example, Refs. [79, 80].

These reactions may be exploited in the study of neutron-rich nuclei by selecting a high-mass target with large neutron excess and a beam as neutron-rich as possible in the region of interest. This is now a well established technique (see for example Refs. [81, 82] and references therein) and transfer channels of up to six-protons have been reported [83]. The expected production of nuclei has been calculated using the multi-nucleon transfer code

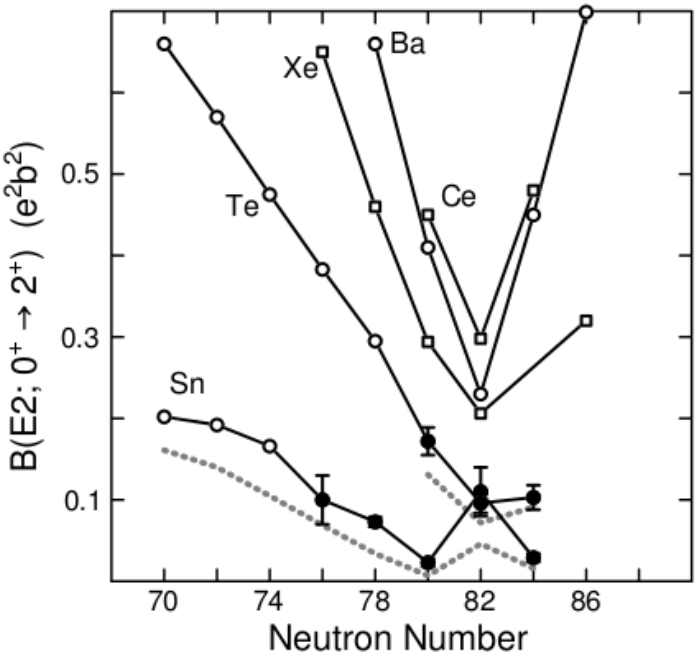

Figure 7.2: The trend in B(E2) values in the ^{132}Sn region. The dotted lines show QPRA calculations for Te and Sn which include a reduced neutron pairing energy above N=82. Figure from Ref. [77].

GRAZING [84], and the results are in Fig. 7.3 [85]. The estimated sensitivity-limit of PRISMA is ∼100 μb/sr, given the available beam-time. Based upon factors, we therefore expect to observe isotopes as neutron-rich as ^{138}Te and ^{136}Sb during this study.

7.2 Experimental details

A ^{136}Xe beam was produced by the PIAVE-ALPI superconducting accelerator at an energy of 926 MeV and beam-current of ∼2 pnA. The beam was focussed onto a ∼500 μg/cm^2 U foil mounted at the target-position of the CLARA array. Outgoing beam-like fragments were transmitted through the PRISMA spectrometer and stopped in a highly-segmented ionisation chamber. An image of the CLARA-PRISMA setup at LNL is shown in Fig. 7.4 with the relevant sections labelled.

The reaction yield for multi-nucleon transfer is maximal around the graz-

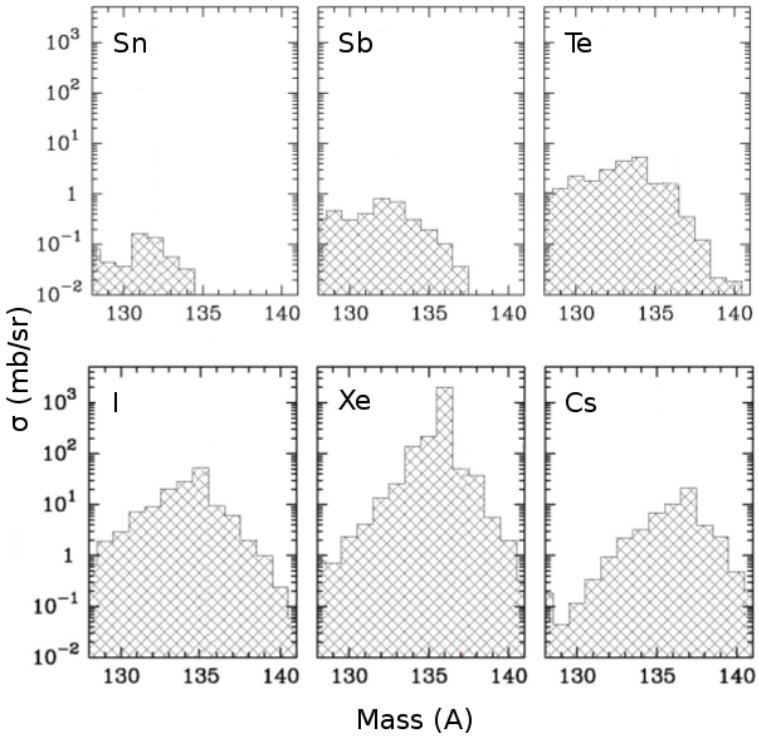

Figure 7.3: Reaction cross sections for ^{136}Xe + ^{238}U at 950 MeV and 52°, calculated using the multi-nucleon transfer code GRAZING [85].

ing angle θ_g of the reaction. This corresponds to the narrow range of impact parameters at which the two nuclei 'graze' each other, bounded by compound nuclear formation at low b and the finite nuclear radii at large b. Considering Coulomb scattering, the impact parameter can be written in terms of the atomic numbers of the beam and target nuclei, Z_b and Z_t respectively, and the emission angle of the beam-like fragment, θ_b [2]

$$b = \left(\frac{Z_b Z_t e^2}{4\pi\epsilon_0 E_k}\right)\left(1 + \mathrm{cosec}\frac{\theta_b}{2}\right). \tag{7.1}$$

If the impact parameter is taken as the sum of nuclear radii, θ_g is found. For the reaction used here $\theta_g \simeq 47°$, and consequently PRISMA was positioned at this angle. In addition to maximising the multi-nucleon transfer yield, this reduces background from competing fusion-evaporation processes which peak

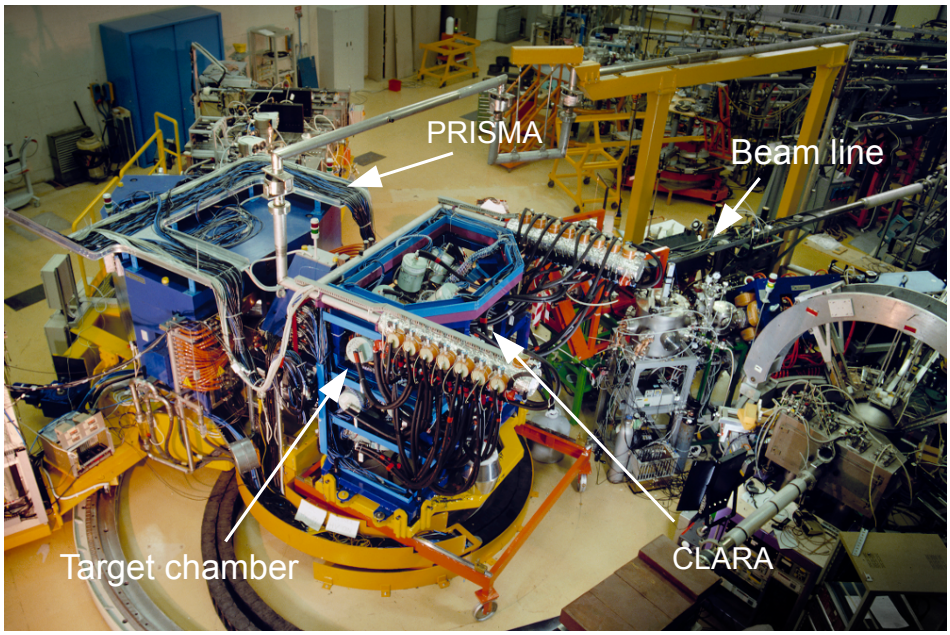

Figure 7.4: The CLARA-PRISMA setup at LNL. Sections of the apparatus relevant to the present work have been labelled.

at forward angles.

PRISMA

PRISMA is a large-acceptance magnetic spectrometer designed for the identification of heavy-ions resulting from nuclear reactions [86]. A schematic diagram of PRISMA is shown in Fig. 7.5.

A micro-channel plate (MCP) detector is at the spectrometer entrance, and covers the entire acceptance solid angle of ∼80 msr (see Ref. [88] for details). A schematic drawing is in Fig. 7.6. A 20 μg/cm^2 carbon foil is placed across the ion trajectories. The secondary electrons produced from ion interactions drift to the MCP plates under a 300-V potential, and are guided by a parallel magnetic field. Upon reaching the MCP the accelerated electrons undergo charge multiplication through grazing collisions with the channel walls. The charge is collected by a pair of orthogonal delay lines situated behind the MCP plates. These consist of 1 mm spaced tungsten

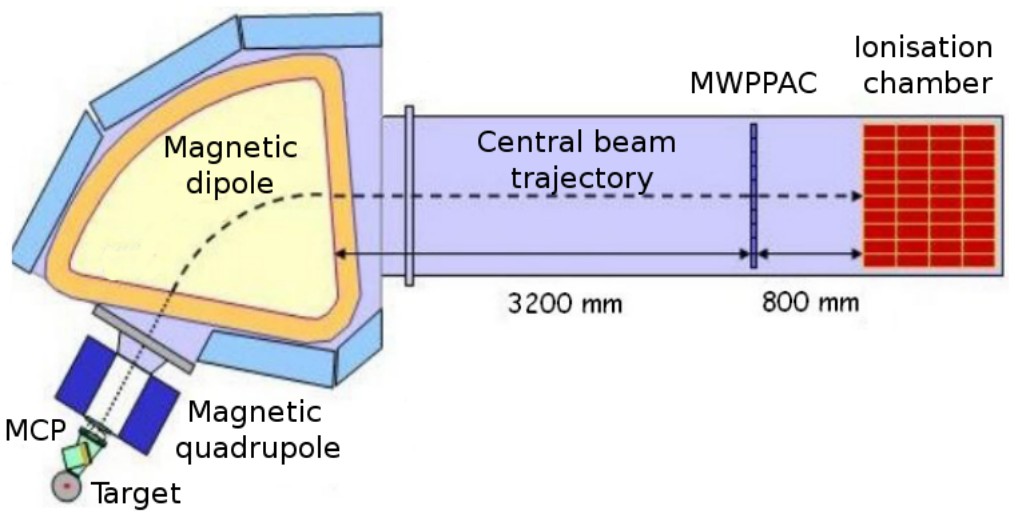

Figure 7.5: Schematic of the PRISMA spectrometer. The central beam trajectory from target to IC is shown. Figure adapted from Ref. [87].

wires wrapped around plexiglass cores.

A fast timing signal, with resolution <400 ps, is picked off the MCP plates themselves. This is passed into three TACS as a start reference, one for both x and y delay lines, and the third for the time-of-flight TOF. The stop reference of both position measurements is taken as the signal from one end of the respective delay lines. The position resolution achieved in both x and y is $\simeq$1 mm (the wire spacing). Assuming knowledge of the beam-spot position, this gives an initial trajectory for each ion.

The magnetic quadrupole following the MCP provides vertical focussing of reaction products. Without this the spectrometer acceptance is greatly reduced, as only ions close to the horizontal plane would be transmitted to the focal plane. The action of the quadrupole in the horizontal plane is to provide further dispersion. The ions are then momentum analysed in the dipole field, as described in Chapter 3, and dispersed according to their magnetic rigidities. The momentum acceptance of the dipole magnet is $\sim$10% either side of the central trajectory, and only ions within this range are transmitted to the focal-plane detector. It should be noted that PRISMA is operated as a tracking spectrometer and therefore does not require high-precision magnets.

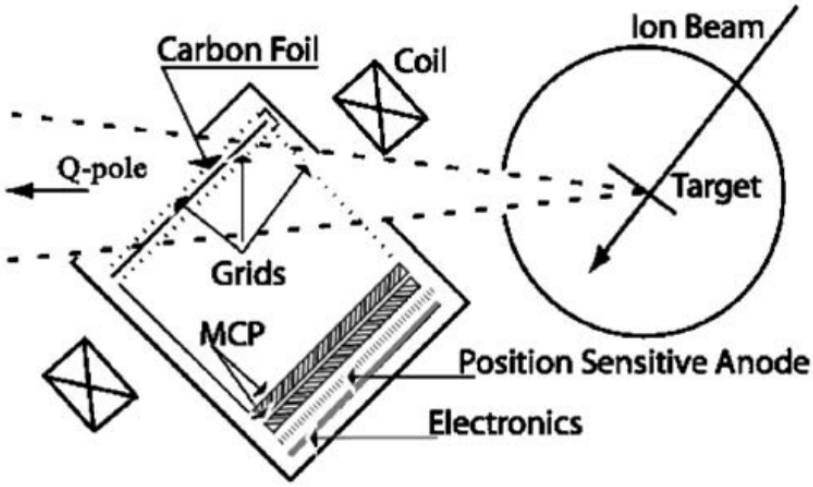

Figure 7.6: Schematic of the MCP detector at the entrance of PRISMA. Position measurements in x and y with resolution $\sim$1 mm are taken from the delay lines behind the MCP plates. A fast timing signal is taken from the plates themselves and used as a start reference for the ion time-of-flight. Figure from Ref. [88].

This is unlike the split-pole spectrograph, discussed in Chapter 3, where careful magnet design is used to overcome optical aberrations. For PRISMA detailed field-maps combined with x, y position measurements are instead used to reconstruct ion trajectories on an event-by-event basis.

At the focal-plane is a multi-wire parallel-plate avalanche counter (MWPPAC), segmented into ten equal sections (see Ref. [89]). A schematic drawing is in Fig. 7.7. The apparatus is filled with isobutane gas to a pressure of 7-8 mbar and sealed by 1.5-μm thick mylar foils at the entrance and exit windows. Inside the chamber are mounted two orthogonal delay lines arranged symmetrically either side of a cathode composed of 0.3 mm spaced tungsten wires and biased at a voltage of -500 V. Both delay lines are grounded, and their positioning either side of the cathode ensures there are no net forces on it which could lead to deformations. Both delay lines consist of evenly spaced gold-plated tungsten wires. In the x-plane a spacing of 1 mm is used and in the y-plane 2 mm. The wires in each plane are connected through a chain of delay chips, and the signals from either end are put through independent TACs, started by a fast signal picked off the cathode plane. This same

fast signal is used to stop the TOF TAC. The spatial resolution obtained is $\sim$1 mm in x and $\sim$2 mm in y, corresponding to the spacing of the respective delay-lines.

Together the MCP and MWPPAC positions define two points along the ion path through the optical elements. As detailed below, this permits the ion trajectory, and hence rigidity, to be determined. The hardware-trigger for recording events is defined as coincident MCP and MWPPAC timing signals.

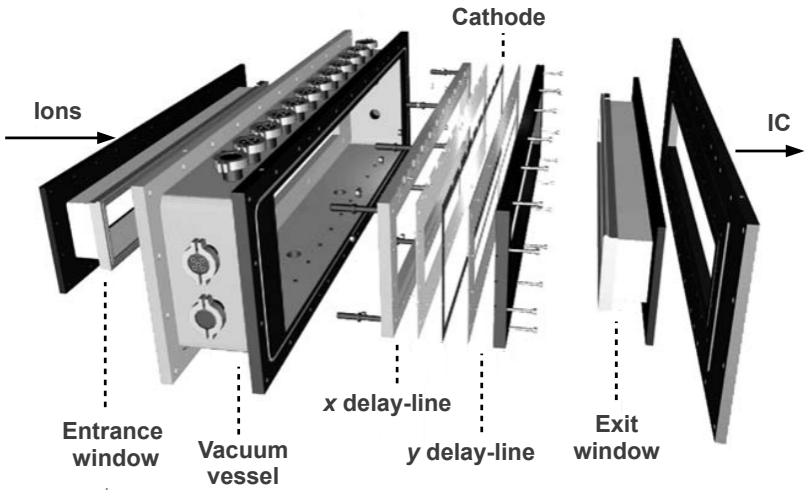

Figure 7.7: An exploded view of the focal-plane detector of PRISMA. Position measurements in x and y are made using a pair of perpendicular delay lines. These sandwich a central cathode which provides a fast timing signal used to stop the time-of-flight TAC. Figure adapted from Ref. [89].

The ions are finally stopped within the ionisation chamber (IC) immediately after the focal plane. For the present work this was filled with methane gas to a pressure of 75 mbar, sufficient to stop the most energetic ions expected. A Frisch grid, common to all segments, is positioned asymmetrically within the IC, 25 mm below the anode and 175 mm above the cathode. The cathodes are all held at ground voltage while a large positive bias ($\sim$ 1.6 kV) is applied to the anode plates. The Frisch grid is help at an intermediate potential ($\sim$ 0.8 kV) and acts to accelerate liberated electrons towards the anode whilst screening their charge from it. Upon passing the Frisch grid a

signal is induced on the anode plates which is independent of the grid-to-ion distance.

The energy loss within the IC gives Z identification and, together with the rigidity and TOF, completely defines the ion identity. The IC is forty-fold segmented, with four rows of ten sections each (see Fig.7.5). This granularity enables an estimate of the final ion-trajectory and range to be made by weighting the location of each segment with the energy deposited within it. Along each edge of the IC are additional 'side' detectors, operated as vetoes. Any ions entering these are assumed to have exited the IC without depositing their full energy and the event ignored.

CLARA

The CLARA array consists of 23 clover detectors subtending a one-π solid angle around the target [90]. Each individual detector consists of four high-purity germanium crystals, contained in the same cryogenic vacuum and clad in a BGO Compton shield. At 1.3 MeV the array has a photopeak efficiency of $\sim$3 % and a resolution of $\sim$1%, after correction for Doppler broadening, at recoil velocities up to 0.1 c. This impressive Doppler correction is made possible by the ion-velocity data provided by PRISMA on an event-by-event basis, discussed below. Given the physical location of individual crystals within the array, the photon energy in the nuclear rest frame is related to that observed by the relation

$$E_\gamma = E_{obs}\left(\frac{1-\frac{v}{c}\cos\theta}{1+\frac{v}{c}\cos\theta}\right)^{1/2}, \tag{7.2}$$

where v is the ion velocity and θ is the polar angle of the crystal relative to the target-PRISMA axis.

The primary role of CLARA in the present work was to confirm the mass assignments of the detected beam-like fragments through known γ-ray transitions. As fragments detected in PRISMA spend only a few ns within the

target chamber, decays from isomers with lifetimes greater than this cannot be observed using this method, nor those from states fed by the isomer. It should also be noted that an inherent problem with recoil-γ coincidence measurements is the background due to the binary partner. Since these have a different recoil velocity to the ion detected, the energies are not properly Doppler corrected and any states broadened.

7.3 Analysis

The analysing power of PRISMA is due primarily to its ion-tracking capability. This is dependent on both detailed mapping of the quadrupole and dipole fields, in addition to precise measurements of the ion entrance and exit positions, TOF and energy loss. For these measurements, accurate detector calibration is required.

Calibration

The image formed at the MCP is distorted by the presence of fringe fields and requires a deformation be applied before it is calibrated. Behind the foil is a mask which shields ions from travelling further downstream, and the resulting shadow can be seen in a x vs. y position matrix, shown in Fig. 7.8. On this shadow are several characteristic markings which can be used for both correction of the deformation and subsequently calibration. Given the location of the MCP relative to the target, the position can be related to the ion emission angle.

At the focal-plane x and y positions are constructed from the relative timing between either end of the relevant delay line. Calibration points are created by fusing the two central wires of each segment, creating an artificial spike. Each segment of the MWPPAC also produces a timing signal for the TOF stop. Each TAC gain is calibrated using a polynomial of third order, deduced from pulser measurements [91], to give an absolute TOF scale in ns.

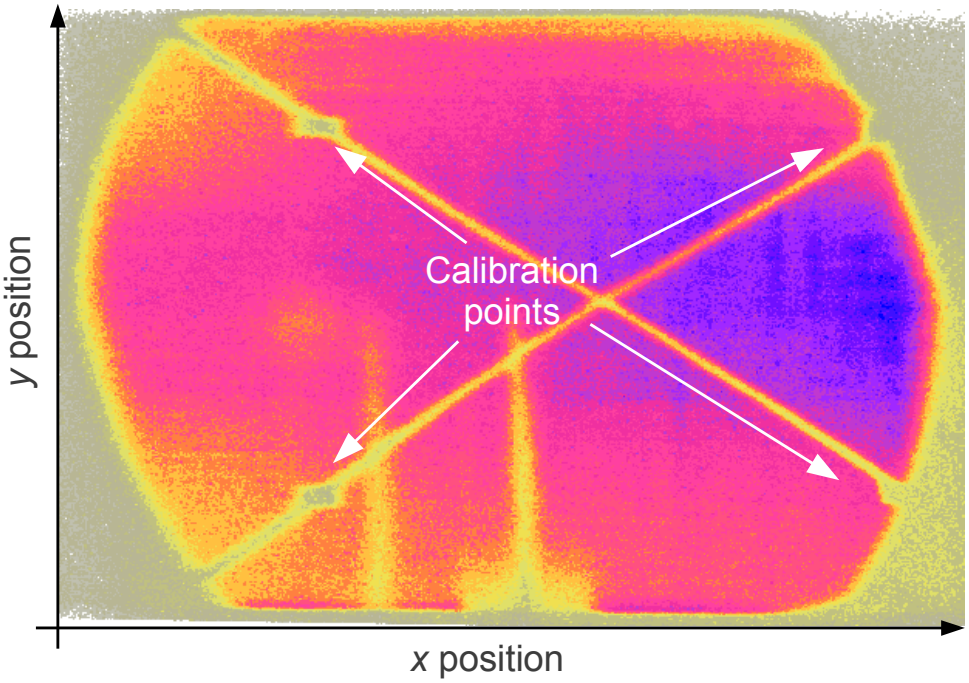

Figure 7.8: A matrix of x vs. y position for the MCP entrance detector. The shadow is produced by a mask placed downstream of the MCP and is used for calibration.

However, there remains a zero offset associated with the TOF provided by each MWPPAC section. A plot of TOF against focal-plane position permits the relative offsets to be observed and corrected, as shown in Fig. 7.9. The two ion groups visible in Fig. 7.9 are a result of both the target and particle-like reaction products entering the spectrometer, with the lighter fragments travelling relatively faster.

The absolute TOF offset is found at a later stage of the analysis using the Doppler corrected γ-ray energies (see Eqn. 7.2). These are sensitive to the calculated ion velocities, which in turn depend on the absolute TOF. The 1313-keV ground-state transition in ^{136}Xe is particularly well suited to this task due to the high yield of inelastically scattered beam observed over a wide range of ion-energies.

An absolute calibration is not required for the energy deposited the IC, since only relative values are important. The individual segments are gain

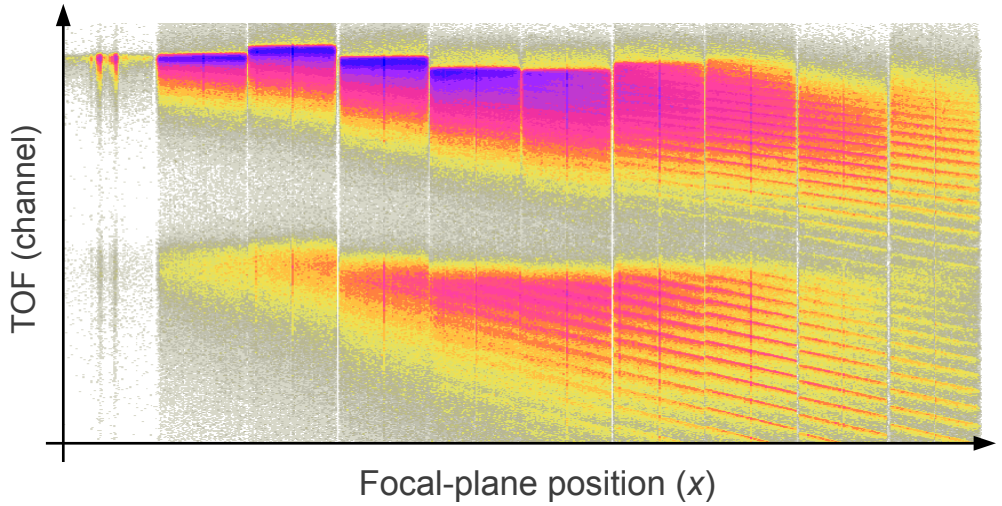

Figure 7.9: The timing signals from each MWPPAC section before correcting for the relative offsets. The upper group corresponds to the beam-like fragments entering the spectrometer and the lower group to target-like fragments. Before calibration increasing channel number corresponds to decreasing TOF.

matched using a linear calibration, again obtained from pulser measurements [91]. Absolute ion-energy measurements, if desired, are attainable with greater accuracy using the ion TOF and mass identification.

The CLARA array is calibrated using standard γ-ray sources of ^{133}Ba and ^{152}Eu. The energy of photons which scatter between multiple crystals, within the same cryostat, are recovered by an 'addback' routine, which sums the output of each crystal firing. The crystal that registers the greatest energy is taken as the initial interaction site for the purposes of Doppler correction (θ in Eqn. 7.2). The BGO shields which surround each cryostat are operated in a veto mode, rejecting all events where the photon scatters outside of an individual clover.

Ion tracking

The purpose of ion-tracking is to provide kinematic information vital for the complete identification of recoil fragments, and also for the correction of Doppler broadening in CLARA. For this the total flight path S, dipole

bending radius ρ and range in the IC R for each ion are required. An algorithm has been developed at LNL to compute these quantities, during offline analysis, based upon a detailed knowledge of the apparatus and calibrated measurements from the various detectors. An outline of the procedure is presented here, for a more complete description see Refs. [92, 93].

As input the algorithm needs both MCP and MWPPAC coordinates, IC energies and the field settings of both magnets. The magnetic field maps, provided by the manufacturer, are stored as external configuration files. The algorithm begins by initialising an ion at the entrance of PRISMA, from where it is transported to the focal-plane by a numerical ray-tracing calculation.

An initial estimate of the ion rigidity is made by simplifying the PRISMA optics, ignoring the quadrupole field and approximating the dipole as ideal. The ion trajectory up to the dipole is linear and given by the MCP. The outgoing trajectory, from the dipole exit to MWPPAC, is also linear and is taken from both the position along the focal-plane and the IC. The path within the IC is calculated by a weighted sum of the energy deposited in each segment

$$x = \frac{\sum_i x_i E_i}{\sum E_i}, \tag{7.3}$$

where x_i are the centres of each segment and E_i the energy loss. This is shown schematically in Fig. 7.10.

Using the estimated rigidity, the ray-tracing calculation transports the ion to the focal plane. The simulated position is compared to that measured using the quantity

$$\chi^2 = (x_{sim} - x_{exp})^2 + (y_{sim} - y_{exp})^2. \tag{7.4}$$

The χ^2 minimum is then found through adjustment of the ion-rigidity, and the values of S and ρ output. The range within the IC is found using the same method as in Eqn. 7.3, but in the longitudinal direction.

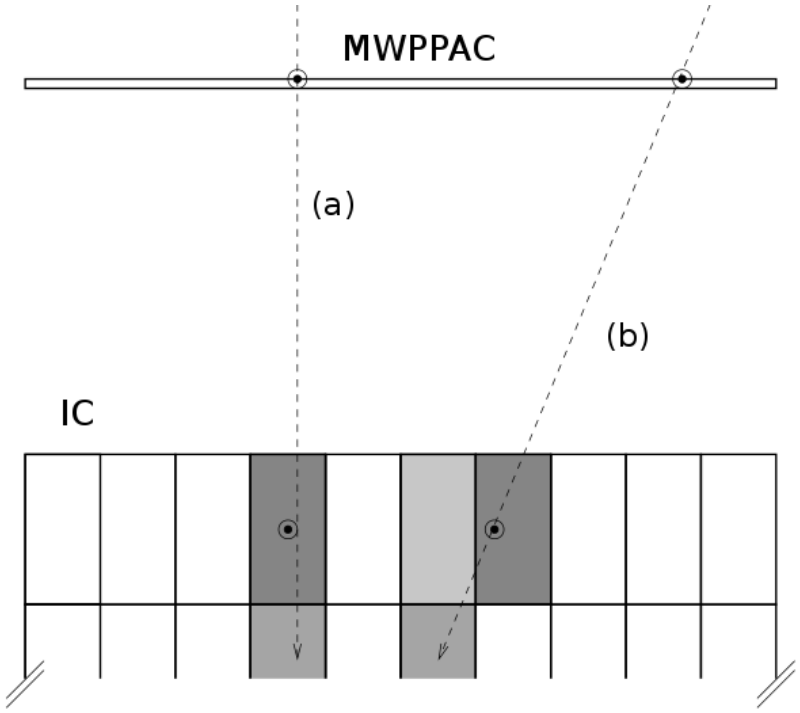

Figure 7.10: The calculation of ion-trajectory within the IC. The segments are shaded according to the energy deposited within them. In the worst case scenario (a) the ion crosses only one segment in each layer. The path is better defined in (b) where the ion intersects multiple segments. Figure adapted from Ref. [92].

Recoil identification

The parameters mentioned up to this point are in principle sufficient to unambiguously identify each recoil. This entails identifying both mass, A, and atomic number, Z. In practice some ambiguity invariably remains, due primarily to limits on the experimental accuracy. The procedure used in the present work to identify recoil fragments is detailed below.

Ions of different Z are separated according to their energy-loss characteristics in the IC. From the Bethe-Bloch equation [2]

$$\frac{dE}{dx} \propto \frac{Z^2}{v^2}, \tag{7.5}$$

therefore the range of ions of a given velocity decreases as Z increases. This dependence is manifest in a matrix of energy loss against range in the IC as

a series of diagonal bands, shown in Fig. 7.11.

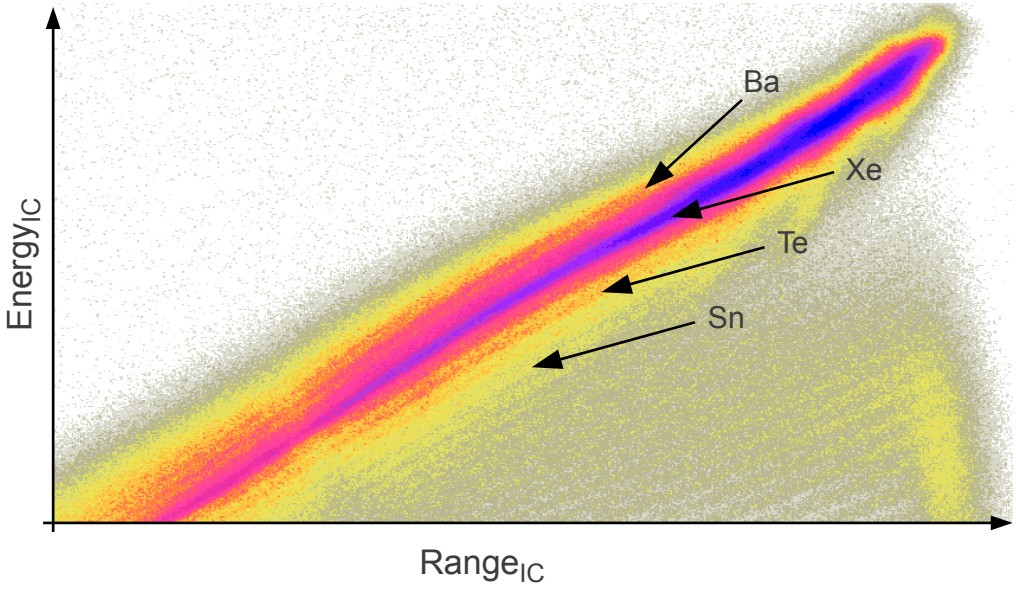

Figure 7.11: The range of ions in the PRISMA IC against total energy loss. Ions of different Z are separated according to their differential energy-loss.

The Z-resolution of PRISMA is expected to be $\sim 1/60$, based upon ions entering the IC with energies above the Bragg peak [89]. For the species studied here this is ~ 2.5 MeV/A, and the measured ion energies only just exceed this. The task of distinguishing Z becomes more challenging the higher in Z, and lower in energy, the ions become due to both greater energy losses in other regions of the spectrometer, and also the fractional decrease in $Z/(Z+1)$. It is expected that the beam-like fragments produced in the present work will be at the sensitivity limit of PRISMA. In practice a Z-resolution of 1/60 is measured. This figure was obtained using a thin slice of the matrix in 7.11, shown in Fig. 7.12. Due to the large amount of scattered beam entering the spectrometer, the isotopes neighbouring Xe are comparatively far more difficult to distinguish.

The velocity of each ion is calculated using the calibrated TOF and path-length through PRISMA

$$v = \frac{S}{\mathrm{TOF}}. \tag{7.6}$$

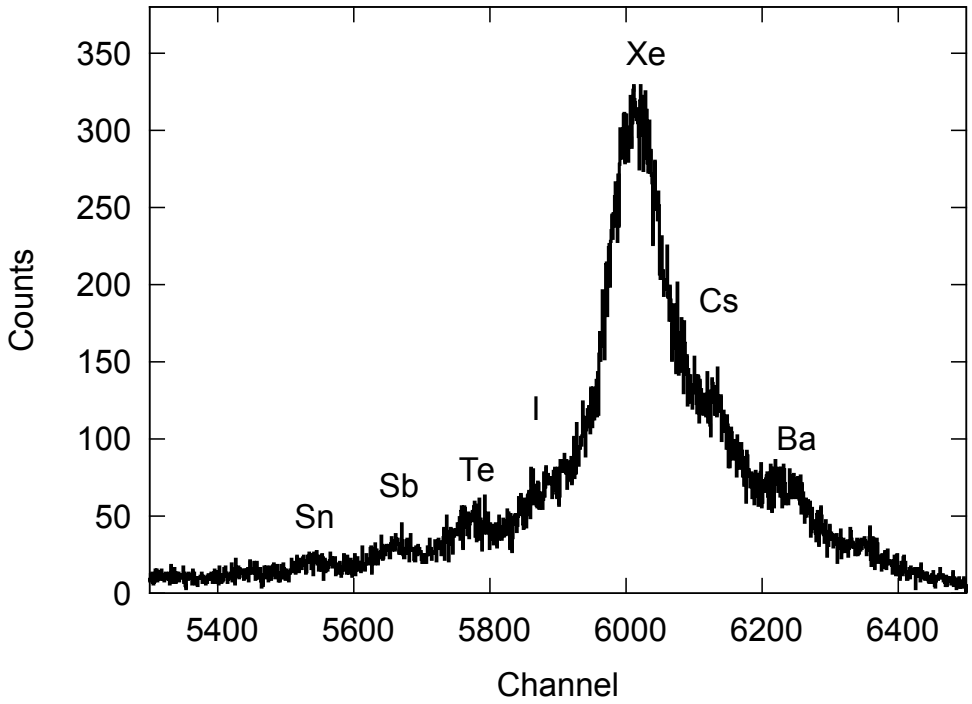

Figure 7.12: A cross section of the matrix shown in Fig. 7.11, over a small range of channels, showing the Z separation obtained. The measured resolution is $\sim 1/60$.

A knowledge of the velocity enables the charge-to-mass ratio to be determined by considering motion within the dipole field

$$\frac{Mv^2}{\rho} = qvB, \tag{7.7}$$

where M is the ion mass, q the charge and B the dipole field strength. Substituting $E_{IC} \propto Mv^2$, Eqn. 7.7 can be rewritten in terms of the remaining unknown, q

$$E_{IC} \propto qvB\rho. \tag{7.8}$$

With reference to Eqn. 7.8, a matrix of E_{IC} against the product $v\rho$ will separate out different charge states. This matrix is shown in Fig. 7.13 for Te isotopes, selected by placing a two-dimensional gate on the matrix in Fig. 7.11. It should be noted that there is a discontinuity in the charge states in Fig. 7.13. This is a result of ions below some value of E_{IC} depositing less

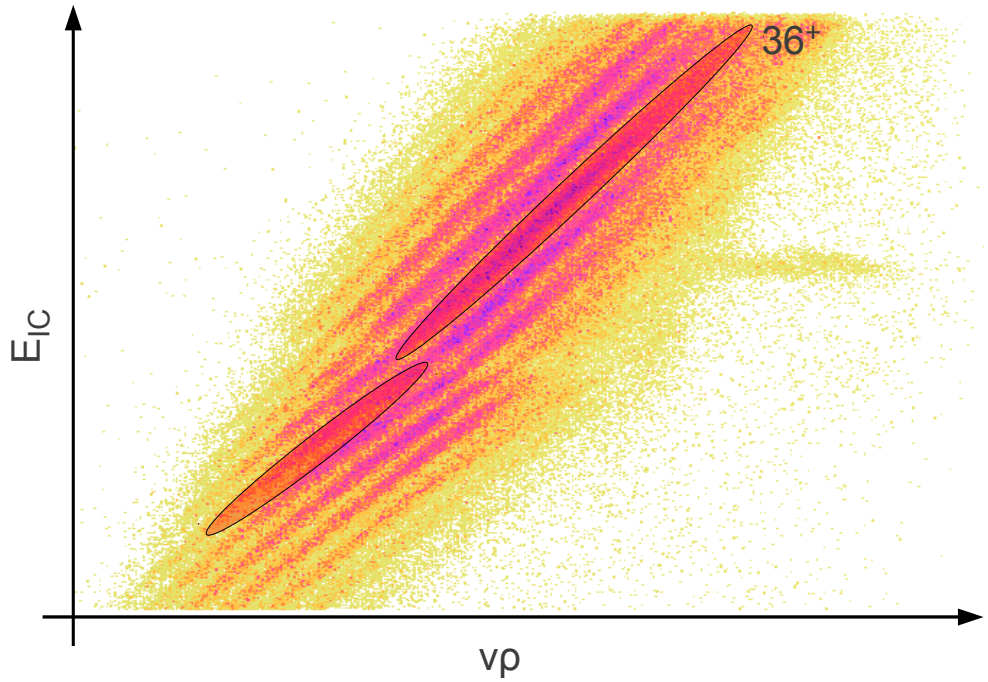

Figure 7.13: Plot of energy loss in the IC against the product of ion-velocity and bending-radius in the dipole field. A gate has been applied on Te isotopes using the matrix in Fig. 7.11. The bands correspond to different ion charge states, and that for 36^+ is highlighted. The discontinuity observed is a consequence of low-energy ions depositing less then the threshold energy at the final IC depth.

then the threshold energy in the final segment of the IC.

Returning to Eqn. 7.7 the charge-to-mass ratio can be expressed as

$$\frac{M}{q} = \frac{B\rho}{v}, \tag{7.9}$$

which becomes an expression for the ion mass if the charge-state is fixed using the matrix in Fig. 7.13. The resulting mass spectra are calibrated by producing mass-γ matrices and looking for characteristic transitions. For example, the coincident γ-ray spectrum for ^{136}Te is in Fig. 7.14 with the E2 cascade from the lowest 6^+ state labelled. Only a single nuclide need be identified in this manner since the neighbouring peaks in the mass spectra are simply $A \pm 1$.

In principle, the calibrated mass spectrum for each charge state can be

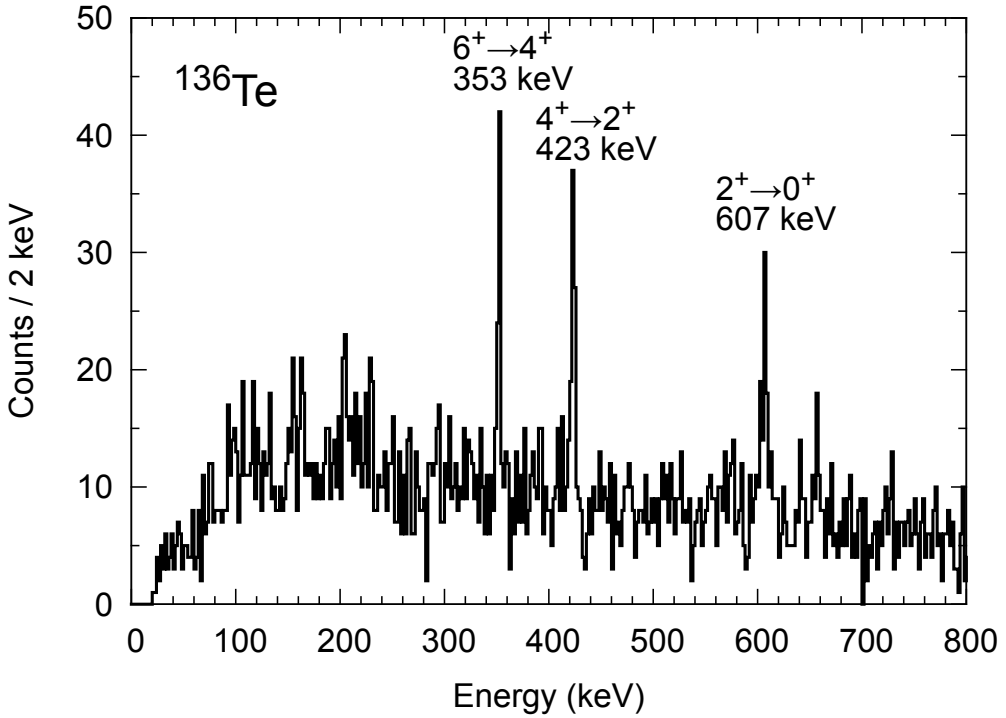

Figure 7.14: Coincident γ-ray spectrum for ^{136}Te with characteristic, low-lying transitions labelled. These provide unambiguous identification of nuclide masses.

summed at this stage to give the total focal-plane yields. In practice it is found that the deduced mass has a smooth dependence on both MCP and focal-plane coordinates. This is shown for the MCP y-coordinate, for example, in Fig. 7.15. It is possible that these arise due to, for example, inaccuracies in the detector calibrations or field-maps, or a slight misalignment of the apparatus. For each of these degrees of freedom, an equivalent matrix to Fig. 7.15 is produced and a correction, based upon fitting a third-order polynomial to the mass-dependence, applied. The effect of these corrections is illustrated in Fig. 7.16 for a single charge-state of Te. The initial mass resolution of $\sim 1/160$ is improved to $\sim 1/210$.

The overall focal-plane yields are found by summing the calibrated mass spectra for each isotope over all observed charge states. A side-by-side comparison of the resulting yields is shown in Fig. 7.17. Full mass spectra, showing also the mass-resolution achieved, are shown in Fig 7.18 for

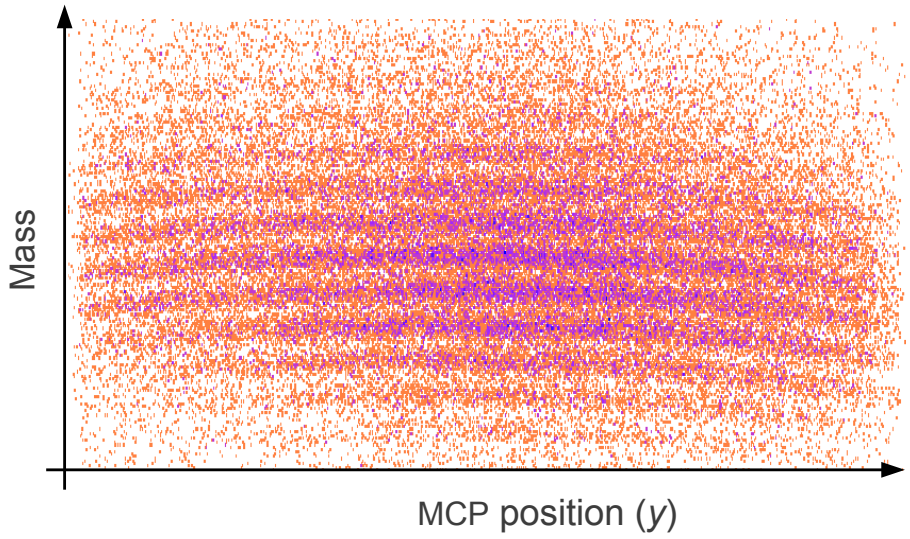

Figure 7.15: A matrix of ion mass against the MCP y coordinate, gated on a single charge state of Te (see text for details). The bowing of the mass states is approximated, then corrected, using a third-order polynomial.

$49 \leq Z \leq 53$. Tabulated yields are provided in Appendix B. It is noted that the mass-spectra shown are built without the requirement for coincident γ-ray detection in CLARA. Requiring at least one photon be detected in coincidence reduces these yields by ∼10%, although it should be remembered that transitions from the binary partner will also be in coincidence.

7.4 Discussion and outlook

The yields shown in Fig. 7.17 are clearly related to the reaction cross sections, however they cannot be assumed to directly reflect them. Of the reaction flux entering PRISMA, some fraction is not transmitted to the focal-plane, and still more is lost in cuts applied to the data during the analysis. It should be noted that, even in the absence of these effects, absolute cross section measurements require a detailed knowledge of the spectrometer acceptance, target thickness and beam current, none of which were accurately determined, or monitored, in this work.

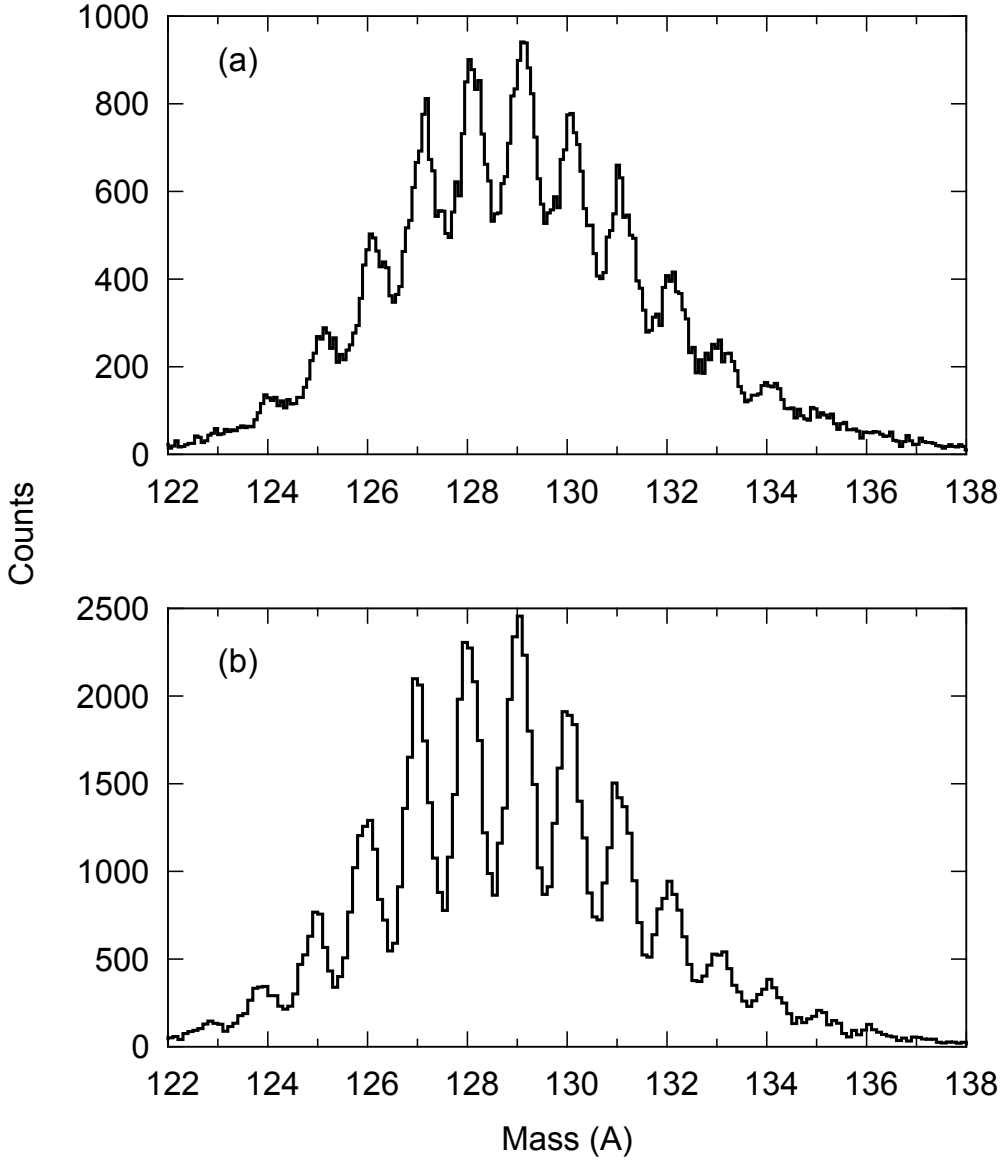

Figure 7.16: Isotopes of Te, gated on a single charge state. Before correcting for the dependence on MCP and focal-plane positions (a) the resolution is $\sim 1/160$, which rises to $\sim 1/210$ after these corrections are made (b).

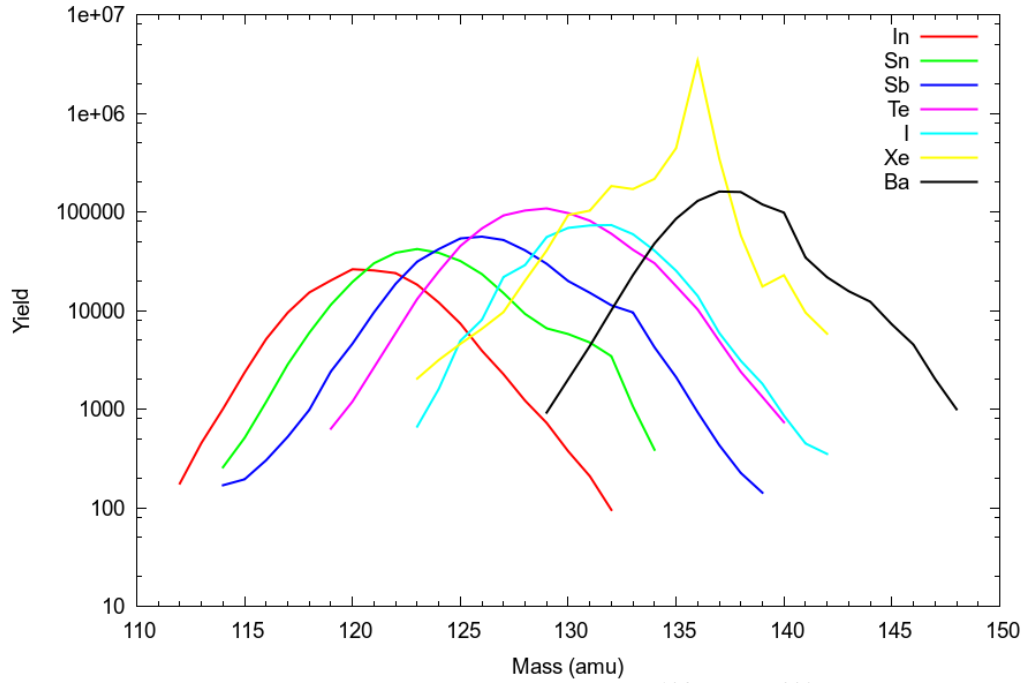

Figure 7.17: The yields of nuclei identified in the ^{136}Xe. + ^{238}U reaction using the PRISMA spectrometer. Results for Cs are not shown as the Z resolution is insufficient to separate it cleanly from Xe.

Cuts are applied to the matrices in Figs. 7.11 and 7.13 in order to select ions of a particular Z and q, respectively. In both instances two-dimensional gates are required, defined by as many as thirty individual points. Although an effort has been made to be systematic in these cuts, by defining regions of equal width for example, the strength of the Xe group (see Fig. 7.12) requires a more prohibitive Z cut to be made for I, and prevents any clean selection of Cs ions. The low yield of I relative to Te, and absence of Cs data, is a direct consequence of this. Nonetheless, these do represent fairly the yields expected in any future studies under similar reaction conditions at PRISMA, since the same issue will arise.

The transmission properties of PRISMA are complex, and depend on the distribution of energy and charge in the reaction products. These are not generally known, but for the high-mass species studied here it is reasonable to assume that the transmission is similar for neighbouring nuclei. On this basis the relative yields obtained can be compared, in a qualitative manner, to the

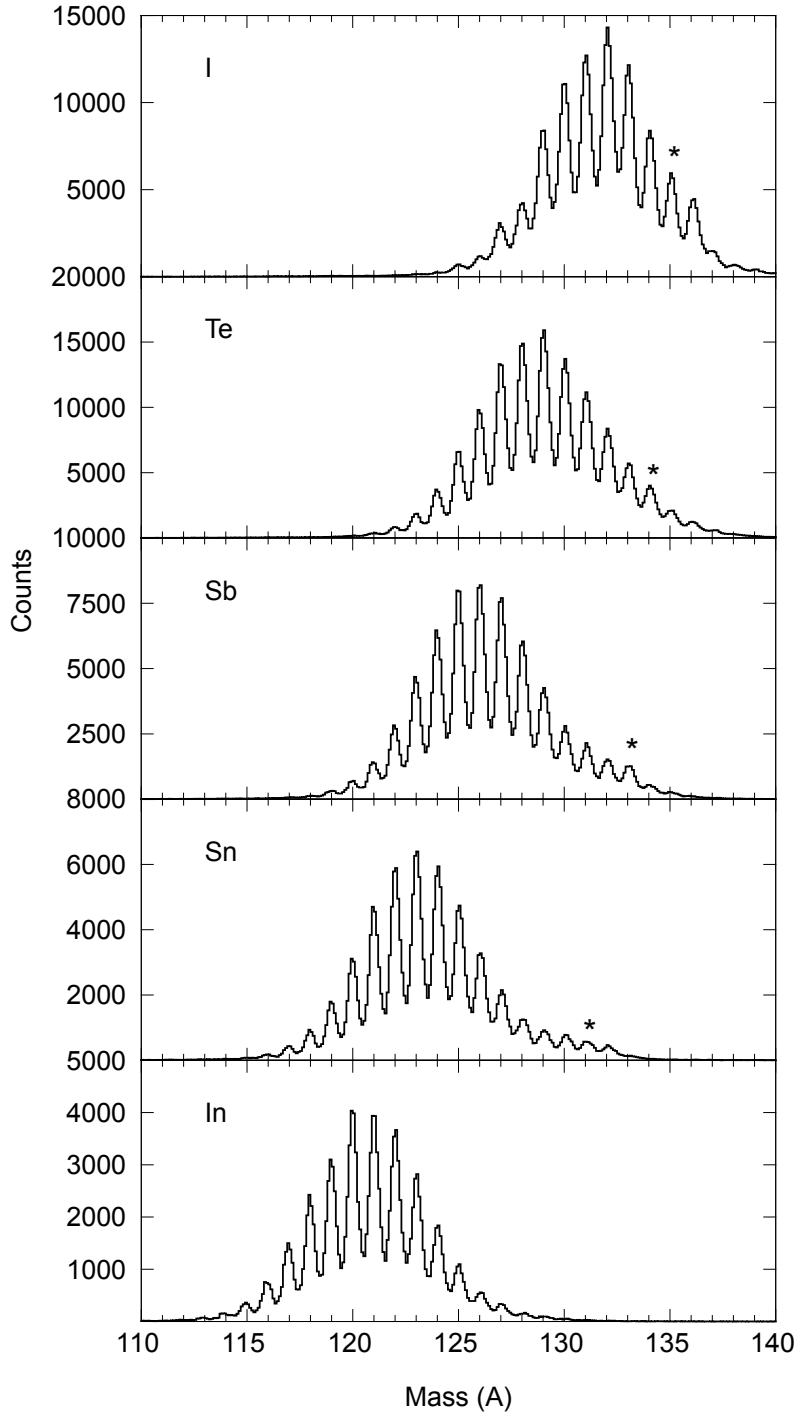

Figure 7.18: Mass-spectra of nuclei with $49 \leq Z \leq 53$ populated in the ^{136}Xe. + ^{238}U reaction at 926 MeV, identified using the PRISMA spectrometer. The attained mass resolution is $\gtrsim$1/200. The peak mass yields predicted by GRAZING calculations are marked $\star$.

results of the GRAZING calculation, shown in Fig. 7.3. It is immediately apparent that the mass states populated have, on average, lower neutron excess then expected. The centroid of the Te mass distribution, for example, is found at $A = 129$, compared to the predicted value of $A = 134$. It is noted that the GRAZING code uses an independent-particle description to account for nucleon transfer. The tendency of stripping neutrons in addition to protons may, therefore, be an indication of pairing effects. Alternatively, it has been suggested that neutron evaporation from the primary fragments in fact drives the yields to lower neutron excess [83]. This appears to be the more likely explanation given the present data, since the maximal yields are observed in channels with typically twice as many neutrons removed as protons. The poor reproduction of the reaction yields by multi-nucleon transfer calculations is clearly a topic of interest in its own right, and further investigation into the underlying reaction mechanism are likely warranted.

The results suggest that there is limited scope for extending spectroscopy in the region using the approach detailed here. The N=83 isotones below Z=54 are populated too weakly for any unknown transitions to be observed in the coincident γ-ray spectra, and well beyond the sensitivity limit for spin-assignments using angular distributions to be made. The situation is exacerbated by the large background created by Doppler broadened transitions in the binary partners.

The excellent recoil identification and moderate yields still provide ample opportunity for lifetime measurements of low-lying states in the region. A proposal to study the lifetimes of the first 2^+, 4^+ and 6^+ states in ^{136}Te has been accepted at LNL, using the differential recoil-distance Doppler-shift RDDS technique [94]. It should be noted that since this work the CLARA array has been replaced at LNL by the AGATA demonstrator (See Ref. [95] and references therein). When complete, AGATA promises to offer unparalleled sensitivity for spectroscopic studies, with an efficiency >40% at 1.3 MeV and position resolution for γ-ray interactions <1 mm thanks to γ-ray tracking algorithms. In its demonstrator phase of 15 out of 180 crystals, AGATA already

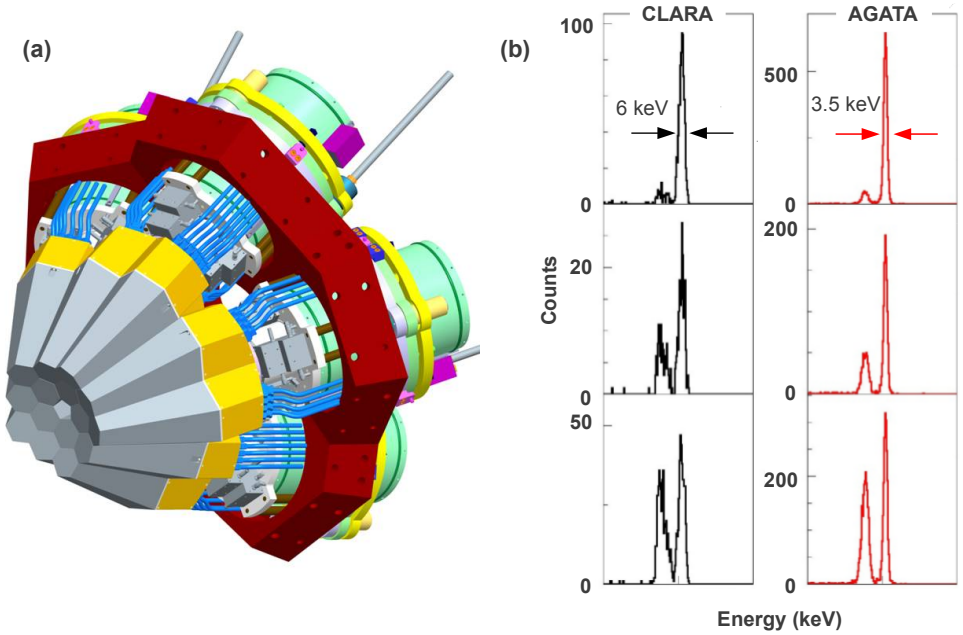

Figure 7.19: (a) The AGATA demonstrator, currently in testing at LNL. Of the 180 crystals comprising the final array, 15 are in place. (b) A comparative simulation of RDDS measurements using PRISMA coupled to the CLARA and AGATA arrays. Improvements in both photopeak efficiency and Doppler corrected energy resolution are expected with AGATA.

offers an efficiency twice that of CLARA, in addition to an improved energy resolution. The excellent Doppler correction in particular makes AGATA a particularly powerful tool when coupled with a time-of-flight spectrometer such as PRISMA. It is in fact ideally suited for RDDS lifetime measurements where the detection of small changes in γ-ray energy are required. Such studies have already been proven possible with CLARA (see for example Ref. [96]), and the enhanced performance expected with AGATA promises to provide a wealth of new information.

APPENDIX

A

MEASURED NEUTRON-REMOVAL CROSS SECTIONS

The measured cross sections for all observed states are included here for completeness. Details regarding the calculations of cross sections, and the spectroscopic associated factors, are given in Chapter 4. Although data were collected at multiple angles in both the (p,d) and (^{3}He,α) reactions, cross sections could not be measured for all states at all angles. The (p,d) data is, in general, most complete at 42° due to the increased time spent on these measurements. For (^{3}He,α) the spectra collected at 5° and 15° are comparable in their statistics (the measurement at 10° for ^{137}Ba is less detailed).

The errors shown on cross sections are statistical only. A discussion of additional errors in these values is given in Section 4.3. In summary, a relative uncertainty of ∼2% should be assumed and an absolute uncertainty of ∼5%. In some circumstances only an upper limit on the cross section could be set. Where this is the case the value is marked *.

Table A.1: Measured cross sections in the ^{138}Ba(p,d)^{137}Ba reaction at a beam energy of 23 MeV.

		σ (mb/sr)			
Peak	E (MeV)	5°	20°	35°	42°
1	0.000	0.952 37	2.966 31	1.231 12	1.645 11
2	0.281	13.29 13	2.016 26	1.344 13	0.636 7
3	0.662	0.328 21	0.435 12	0.664 9	0.643 7
4	1.252	0.016 5	0.050 4	0.058 3	0.054 2
5	1.290	0.462 25	0.771 16	0.271 6	0.412 5
6	1.460	0.472 25	0.833 16	0.314 6	0.457 6
7	1.840	1.070 38	0.303 10	0.129 4	0.057 3
8	1.900	0.377 23	0.503 13	0.184 5	0.321 5
9	2.040	0.538 28	0.629 14	0.256 6	0.390 5
10	2.117	0.023 7	0.037 4	0.016 2	0.024 1
11	2.230	0.012 7	0.039 4	0.057 3	0.042 2
12	2.271	-	0.021 3	0.023 2	0.015 1
13	2.320	0.037 8	0.059 5	0.081 3	0.080 2
14	2.380	-	0.037 4	0.059 3	0.040 2
15	2.440	-	0.059 5	0.043 3	0.033 2
16	2.530	0.066 12	0.067 5	0.028 2	0.042 2
17	2.610	-	0.008 2	0.014 2	0.007 1
18	2.670	0.023 7	0.039 4	0.017 2	0.020 1
19	2.750	-	0.019 3	0.027 2	0.023 1
20	2.810	-	-	0.005 1	0.009 1
21	2.890	0.050 11	0.026 4	0.020 2	0.028 2
22	2.990	0.031 19	0.029 5	0.048 3	0.045 2
23	3.030	0.023 19	0.036 5	0.024 2	0.028 2
24	3.120	-	-	0.011 2	0.015 1
25	3.150	-	0.027 4	0.012 2	0.011 1
26	3.210	-	-	0.016 2	0.021 1
27	3.420	-	0.006 2	0.009 1	0.008 1
28	3.550	-	0.031 4	0.022 2	0.029 2

Table A.2: Measured cross sections in the ^{138}Ba(^{3}He,α)^{137}Ba reaction at a beam energy of 34 MeV. Results marked * represent upper limits.

		σ (mb/sr)		
Peak	E (MeV)	5°	10°	15°
1	0.000	0.202 6	0.163 6	0.174 4
2	0.281	0.04* 1	-	0.03* 1
3	0.662	3.125 27	2.534 25	1.816 15
4	1.252	0.070 9	0.062 9	0.036 5
5	1.290	0.135 10	0.106 9	0.088 5
6	1.460	0.149 6	0.084 6	0.088 3
7	1.840	0.01* 1	-	0.006* 3
8	1.900	0.148 7	0.163 7	0.066 3
9	2.040	0.198 8	0.168 9	0.111 5
10	2.117	0.010 11	-	0.014 5
11	2.230	0.230 8	0.144 8	0.118 6
12	2.271	0.07* 2	-	0.009* 4
13	2.320	0.470 11	0.427 11	0.311 6
14	2.380	0.05* 1	-	0.02* 1
15	2.440	0.028 7	-	0.018 5
16	2.530	0.032 7	-	0.011 3
17	2.610	0.010 9	-	0.010 3
18	2.670	0.069 17	-	0.009 4
19	2.750	0.211 16	0.177 15	0.110 5
20	2.810	0.065 10	0.092 11	0.040 5
21	2.890	0.092 10	0.122 11	0.055 6
22	2.990	0.425 13	0.384 13	0.269 6
23	3.030	0.05* 1	-	0.02* 1
24	3.120	0.178 18	0.128 16	0.083 8
25	3.150	0.03* 1	-	0.01* 1
26	3.210	0.173 10	0.152 9	0.138 5
27	3.420	0.065 10	0.056 8	0.027 4
28	3.550	0.133 10	0.104 9	0.073 5

Table A.3: Measured cross sections in the ^{140}Ce(p,d)^{139}Ce reaction at a beam energy of 23 MeV.

		σ (mb/sr)			
Peak	E (MeV)	5°	20°	35°	42°
1	0.000	1.060 36	2.625 36	0.926 9	1.341 12
2	0.252	10.07 11	1.634 28	1.145 10	0.486 7
3	0.755	0.315 19	0.364 13	0.480 7	0.522 7
4	1.321	0.801 31	1.169 25	0.432 7	0.695 10
5	1.347	0.036 10	0.104 10	0.084 3	0.099 6
6	1.598	0.110 12	0.197 11	0.067 3	0.101 3
7	1.632	0.034 8	0.060 7	0.013 1	0.020 2
8	1.823	0.047 8	0.042 5	-	0.035 2
9	1.889	0.607 29	0.230 14	0.081 3	0.028 3
10	1.911	0.309 22	0.302 15	0.151 4	0.196 5
11	2.018	-	0.011 3	0.013 1	0.009 1
12	2.090	0.223 16	0.206 10	0.093 3	0.157 4
13	2.143	0.083 10	0.076 7	0.043 2	0.069 3
14	2.251	-	0.010 3	0.011 1	0.012 1
15	2.286	-	0.063 6	0.079 3	0.097 4
16	2.362	-	0.035 5	0.028 2	0.030 2
17	2.426	0.020 7	0.022 4	0.015 1	0.020 2
18	2.455	-	0.005 3	0.010 1	0.007 1
19	2.556	0.061 16	0.057 11	0.027 4	0.027 4
20	2.610	-	0.004 2	0.005 1	0.007 1
21	2.701	-	-	0.008 1	0.011 1
22	2.800	-	-	0.012 3	0.013 1
23	2.822	-	0.021 4	0.029 3	0.030 1
24	2.910	0.029 7	0.033 4	0.021 1	0.023 2
25	2.964	0.029 7	0.027 4	0.010 1	0.012 1
26	3.082	-	-	0.011 1	0.008 1
27	3.196	-	0.017 4	0.020 2	0.023 2
28	3.282	-	0.015 4	0.010 1	0.012 1
29	3.352	-	0.036 5	0.022 2	0.032 2

Table A.4: Measured cross sections in the ^{140}Ce(^{3}He,α)^{139}Ce reaction at a beam energy of 34 MeV. Results marked * represent upper limits. The cross sections of Peaks 22 and 23 are not measured directly, see Section 4.4 for details.

		σ (mb/sr)	
Peak	E (MeV)	5°	15°
1	0.000	0.191 8	0.169 4
2	0.252	0.006* 4	0.039* 3
3	0.755	2.705 29	1.717 13
4	1.321	0.147 20	0.107 7
5	1.347	0.240 20	0.111 7
6	1.598	0.049 5	0.019 3
7	1.632	0.011 12	0.011 4
8	1.823	0.008 5	0.005 2
9	1.889	-	-
10	1.911	0.084 7	0.058 3
11	2.018	0.029 18	0.018 2
12	2.090	0.077 29	0.053 4
13	2.143	0.043 12	0.024 3
14	2.251	0.051 9	0.029 5
15	2.286	0.512 15	0.348 9
16	2.362	0.170 11	0.086 4
17	2.426	0.04* 3	0.013* 2
18	2.455	0.065 16	0.031 6
19	2.556	0.123 13	0.071 4
20	2.610	0.043 13	0.013 4
21	2.701	0.039 7	0.022 3
22	2.800	0.085 6	0.048 2
23	2.822	0.231 15	0.171 5
24	2.910	0.07* 1	0.03* 1
25	2.964	0.006 9	0.008 4
26	3.082	0.055 8	0.009 3
27	3.196	0.206 19	0.120 5
28	3.282	0.160 20	0.076 4
29	3.352	0.082 14	0.034 5

Table A.5: Measured cross sections in the ^{142}Nd(p,d)^{141}Nd reaction at a beam energy of 23 MeV.

		σ (mb/sr)			
Peak	E (MeV)	5°	20°	35°	42°
1	0.000	1.010 27	2.005 26	0.804 10	1.195 11
2	0.192	7.184 72	1.374 22	1.115 12	0.373 6
3	0.759	0.328 15	0.348 11	0.482 8	0.498 7
4	1.222	0.931 26	0.966 18	0.564 8	0.752 9
5	1.343	0.006 2	0.023 3	0.054 3	0.048 2
6	1.565	0.096 8	0.079 5	0.040 2	0.061 2
7	1.597	0.009 3	0.020 3	0.011 1	0.009 1
8	1.822	0.257 14	0.209 9	0.138 4	0.190 4
9	1.888	0.236 14	0.129 7	0.076 3	0.020 1
10	1.968	-	0.006 2	0.010 1	0.007 1
11	2.070	0.100 9	0.113 6	0.079 3	0.099 3
12	2.111	0.042 7	0.037 4	0.025 2	0.034 2
13	2.180	0.065 8	0.022 3	0.018 2	0.005 1
14	2.208	0.035 7	0.057 7	0.072 3	0.068 3
15	2.310	-	0.023 4	0.026 2	0.025 2
16	2.349	-	0.015 3	0.018 2	0.015 1
17	2.384	-	0.013 3	0.010 2	0.006 1
18	2.512	0.019 4	0.015 3	0.014 2	0.004 1
19	2.581	0.020 4	0.010 2	0.016 2	0.017 1
20	2.616	0.009 4	0.004 2	0.009 1	0.004 1
21	2.705	0.007 3	0.011 2	0.006 1	0.004 1
22	2.809	0.019 4	0.013 2	0.008 1	0.008 1
23	2.915	0.017 6	0.019 4	0.030 2	0.027 2
24	2.939	0.049 7	0.030 6	0.034 2	0.033 2
25	3.042	-	0.008 2	0.007 1	0.009 1
26	3.112	-	0.019 8	0.017 2	0.016 2
27	3.315	-	0.006 2	0.002 1	0.003 1
28	3.369	0.047 7	0.030 4	0.027 2	0.028 2
29	3.407	0.061 8	0.039 4	0.039 2	0.037 2

Table A.6: Measured cross sections in the ^{142}Nd(^{3}He,α)^{141}Nd reaction at a beam energy of 34 MeV. Results marked * represent upper limits. The cross sections for Peaks 15-17 are not measured directly, see Section 4.4 for details.

		σ (mb/sr)	
Peak	E (MeV)	5°	15°
1	0.000	0.212 6	0.168 4
2	0.192	0.007* 3	0.003* 1
3	0.759	2.548 22	1.688 13
4	1.222	0.286 8	0.163 5
5	1.343	0.157 7	0.085 4
6	1.565	0.032 5	0.015 2
7	1.597	0.008 7	0.004 4
8	1.822	0.127 6	0.006 0
9	1.888	0.001* 1	0.003* 2
10	1.968	0.044 5	0.022 2
11	2.070	0.099 6	0.043 3
12	2.111	0.024 14	0.004 2
13	2.180	-	-
14	2.208	0.508 10	0.340 5
15	2.310	0.225 6	0.135 3
16	2.349	0.135 4	0.081 2
17	2.384	0.054 3	0.032 1
18	2.512	0.020 5	0.021 3
19	2.581	0.046* 6	0.053* 3
20	2.616	0.007 3	0.005 6
21	2.705	0.009 5	0.021 3
22	2.809	0.002 1	0.002 1
23	2.915	0.210 16	0.148 8
24	2.939	0.045 12	0.019 4
25	3.042	0.110 8	0.050 4
26	3.112	0.155 8	0.079 4
27	3.315	0.005 3	0.002 1
28	3.369	0.025 21	0.019 6
29	3.407	0.103 22	0.046 6

Table A.7: Measured cross sections in the ^{144}Sm(p,d)^{143}Sm reaction at a beam energy of 23 MeV. Due to the presence of elastically scattered protons at the focal plane, no states above ∼3.1 MeV were observed in (p,d).

		σ (mb/sr)			
Peak	E (MeV)	5°	20°	35°	42°
1	0.000	1.107 36	1.524 23	0.572 10	0.901 8
2	0.110	5.406 79	1.398 21	0.979 12	0.229 4
3	0.758	0.334 20	0.360 11	0.420 8	0.405 6
4	1.100	0.939 34	0.948 18	0.480 9	0.636 7
5	1.362	0.016 6	0.022 3	0.034 2	0.037 2
6	1.533	0.050 8	0.037 4	0.023 2	0.036 2
7	1.708	0.109 12	0.082 6	0.058 3	0.065 2
8	1.930	-	0.013 3	0.008 1	0.009 1
9	1.990	0.093 12	0.105 6	0.048 3	0.006 1
10	2.064	0.127 14	0.081 6	0.064 3	0.074 2
11	2.161	-	0.022 3	0.022 2	0.021 1
12	2.274	0.023 7	0.022 4	0.012 2	0.012 1
13	2.450	-	0.017 9	0.033 3	0.035 2
14	2.586	-	0.015 4	0.021 6	0.022 4
15	2.662	-	0.008 3	0.008 2	0.008 1
16	2.842	-	-	-	-
17	3.017	-	-	-	0.014 2
18	3.085	-	-	-	-
19	3.180	-	-	-	-
20	3.245	-	-	-	-

Table A.8: Measured cross sections in the ^{144}Sm(^{3}He,α)^{143}Sm reaction at a beam energy of 34 MeV. Results marked * represent upper limits.

		σ (mb/sr)	
Peak	E (MeV)	5°	15°
1	0.000	0.236 9	0.163 4
2	0.110	0.02* 1	0.035* 3
3	0.758	2.622 27	1.831 15
4	1.100	0.395 12	0.219 7
5	1.362	0.219 11	0.111 5
6	1.533	0.012 6	0.008 3
7	1.708	0.059 7	0.037 4
8	1.930	0.021 5	0.009 5
9	1.990	0.01* 1	0.01* 2
10	2.064	0.090 9	0.055 3
11	2.161	0.218 11	0.112 4
12	2.274	0.112 11	0.046 5
13	2.450	0.348 19	0.242 6
14	2.586	0.197 18	0.154 5
15	2.662	0.101 8	0.051 3
16	2.842	0.028 11	0.011 5
17	3.017	0.153 9	0.078 4
18	3.085	0.13* 1	0.063* 4
19	3.180	0.11* 1	0.034* 3
20	3.245	0.06* 1	0.019* 2

APPENDIX

B

MASS YIELDS FROM THE ^{136}XE + ^{238}U REACTION

The integrated yields of isotopes identified at the focal-plane of PRISMA in the range $49 \leq Z \leq 54$ are tabulated below. The experiment ran for four days at a beam energy of 926 MeV and with a beam current of ∼2 pna. The U targets had a nominal thickness of 500 μg/cm^2. They are known to have deteriorated during exposure to the beam, but no quantitative data on the extent of this is available. No attempt is made to extract cross sections from this data. Full details of the experimental setup and analysis procedure are provided in Chapter 7.

Table B.1: The yields of Te, I, and Xe isotopes measured at the PRISMA focal plane. See Chapter 7 for experimental details.

Te		I		Xe	
Mass	Yield	Mass	Yield	Mass	Yield
121	2700 300	123	670 300	123	2000 400
122	5900 500	124	1600 400	124	3100 400
123	13000 800	125	4900 600	125	4600 600
124	25000 400	126	8000 800	126	6500 600
125	45000 2000	127	22000 1000	127	9600 800
126	68000 2000	128	29000 500	128	20000 1000
127	92000 3000	129	56000 1000	129	41000 2000
128	100000 3000	130	69000 2000	130	93000 3000
129	110000 1000	131	73000 2000	131	100000 4000
130	97000 3000	132	74000 2000	132	180000 2000
131	81000 3000	133	59000 500	133	170000 6000
132	60000 2000	134	40000 1000	134	220000 8000
133	41000 2000	135	25000 700	135	440000 10000
134	30000 300	136	14000 500	136	3400000 40000
135	18000 600	137	5900 300	137	350000 2000
136	10000 500	138	3100 100	138	58000 4000
137	4900 300	139	1800 100	139	18000 2000
138	2400 200	140	860 80	140	23000 3000
139	1300 20	141	450 5	141	9500 70
140	740 10	142	350 4	142	5800 40

Table B.2: The yields of In, Sn and Sb isotopes measured at the PRISMA focal plane. See Chapter 7 for experimental details.

In		Sn		Sb	
Mass	Yield	Mass	Yield	Mass	Yield
112	180 60	114	260 60	119	2400 50
113	450 90	115	510 90	120	4600 300
114	1000 100	116	1200 100	121	9600 500
115	2300 200	117	2800 200	122	19000 700
116	5100 300	118	5900 300	123	31000 900
117	9500 100	119	11000 100	124	42000 400
118	15000 600	120	19000 200	125	54000 2000
119	20000 700	121	30000 1000	126	56000 2000
120	26000 800	122	38000 1000	127	52000 2000
121	25000 200	123	42000 1000	128	41000 1000
122	24000 600	124	38000 1000	129	30000 300
123	18000 500	125	32000 300	130	20000 600
124	12000 400	126	23000 800	131	15000 500
125	7400 200	127	15000 600	132	11000 400
126	3900 200	128	9200 500	133	9600 400
127	2300 100	129	6600 400	134	4200 40
128	1200 10	130	5800 60	135	2100 100
129	720 40	131	4700 200	136	930 70
130	370 30	132	3400 100	137	430 50
131	210 20	133	1100 80	138	230 3
132	95 10	134	390 6	139	140 2

REFERENCES

[1] R. F. Casten. *Nuclear Structure from a Simple Perspective.* 2nd edn. ("Oxford University Press", 2000).

[2] K. Krane. *Introductory Nuclear Physics.* 2nd edn. ("John Wiley and Sons", 1988).

[3] T. Otsuka, R. Fujimoto, Y. Utsuno *et al.* Phys. Rev. Lett. **87**, 082502 (2001).

[4] J. A. Cizewski and E. Glmez. Physics Letters B **175**, 11 (1986).

[5] A. Ozawa, T. Kobayashi, T. Suzuki *et al.* Phys. Rev. Lett. **84**, 5493 (2000).

[6] T. Otsuka, T. Suzuki, R. Fujimoto *et al.* Phys. Rev. Lett. **95**, 232502 (2005).

[7] A. Bohr and B. Mottleson". *Nuclear Structure, Volume 1: Single-Particle Motion.* 1st edn. ("W.A. Benjamin, inc", 1969).

[8] N. Smirnova, B. Bally, K. Heyde *et al.* Physics Letters B **686**, 109 (2010).

[9] T. Otsuka, T. Suzuki, M. Honma *et al.* Phys. Rev. Lett. **104**, 012501 (2010).

[10] J. P. Schiffer, S. J. Freeman, J. A. Caggiano *et al.* Phys. Rev. Lett. **92**, 162501 (2004).

[11] B. P. Kay. Ph.D. thesis, The University of Manchester (2007).

[12] B. Kay, S. Freeman, J. Schiffer *et al.* Physics Letters B **658**, 216 (2008).

[13] B. H. Wildenthal, E. Newman and R. L. Auble. Phys. Rev. C **3**, 1199 (1971).

[14] A. Chaumeaux, G. Bruge, H. Faraggi *et al.* Nuclear Physics A **164**, 176 (1971).

[15] R. K. Jolly and E. Kashy. Phys. Rev. C **4**, 887 (1971).

[16] E. Friedland, M. Goldschmidt, C. A. Wiedner *et al.* Nuclear Physics A **256**, 93 (1976).

[17] G. Berrier, M. Vergnes, G. Rotbard *et al.* Journal de Physique **37**, 311 (1976).

[18] S. El-Kazzaz, J. Lien, G. Lvhiden *et al.* Nuclear Physics A **280**, 1 (1977).

[19] S. Galès, G. M. Crawley, D. Weber *et al.* Nuclear Physics A **398**, 19 (1983).

[20] C. D. V. Rooden, D. Spaargaren, H. P. Blok *et al.* Nuclear Physics A **430**, 125 (1984).

[21] C. A. Bertulani. *Introduction to Nuclear Reactions*. 1st edn. ("Institute of Physics Publishing", 2004).

[22] S. T. Butler. Proceedings of the Royal Society of London. Series A. Mathematical and Physical Sciences **208**, 559 (1951).

[23] N. K. Glendenning. *Direct Nuclear Reactions*. 1st edn. ("Academic Press", 1983).

[24] C. M. Perey and F. G. Perey. Atomic Data and Nuclear Data Tables **17**, 1 (1976).

[25] G. R. Satchler. *Direct Nuclear Reactions*. 1st edn. ("Oxford University Press", 1988).

[26] M. Macfarlane and S. Pieper. ANL-76-11(Rev.1) (1976).

[27] M. H. Macfarlane and J. B. French. Rev. Mod. Phys. **32**, 567 (1960).

[28] H. Hyder, J. Baris, C. Gingell *et al.* Nuclear Instruments and Methods in Physics Research Section A: Accelerators, Spectrometers, Detectors and Associated Equipment **268**, 285 (1988).

[29] J. Ashenfelter. Pramana journal of physics **59**, 713 (2002).

[30] R. Middleton. Nuclear Instruments and Methods **122**, 35 (1974).

[31] J. E. Spencer and H. A. Enge. Nuclear Instruments and Methods **49**, 181 (1967).

[32] H. A. Enge. Nuclear Instruments and Methods **162**, 161 (1979).

[33] A. R. Parikh. Ph.D. thesis, Yale University (2006).

[34] S. J. Freeman. private communication (2008).

[35] E. Browne and J. Tuli. Nuclear Data Sheets **108**, 2173 (2007).

[36] T. W. Burrows. Nuclear Data Sheets **92**, 623 (2001).

[37] J. K. Tuli and D. F. Winchell. Nuclear Data Sheets **92**, 277 (2001).

[38] J. K. Tuli. Nuclear Data Sheets **94**, 605 (2001).

[39] J. A. Clarke. private communication (2003).

[40] R. K. Jolly and E. Kashy. Phys. Rev. C **4**, 1398 (1971).

[41] F. G. Perey. Phys. Rev. **131**, 745 (1963).

[42] C. M. Perey and F. G. Perey. Phys. Rev. **132**, 755 (1963).

[43] E. R. Flynn, R. E. Brown, F. Ajzenberg-Selove *et al.* Phys. Rev. C **28**, 575 (1983).

[44] R. Perry, A. Nadasen, D. L. Hendrie *et al.* Phys. Rev. C **24**, 1471 (1981).

[45] G. R. Satchler, W. C. Parkinson and D. L. Hendrie. Phys. Rev. **187**, 1491 (1969).

[46] J. P. Schiffer, S. J. Freeman, J. A. Clark *et al.* Phys. Rev. Lett. **100**, 112501 (2008).

[47] J. P. Schiffer. private communication (2009).

[48] K. S. Low and T. Tamura. Phys. Rev. C **11**, 789 (1975).

[49] E. Dragulescu, M. Ivascu, R. Mihu *et al.* Journal of Physics G: Nuclear Physics **10**, 1099 (1984).

[50] F. D. Becchetti and G. W. Greenlees. Phys. Rev. **182**, 1190 (1969).

[51] J. J. H. Menet, E. E. Gross, J. J. Malanify *et al.* Phys. Rev. C **4**, 1114 (1971).

[52] R. L. Varner, W. J. Thompson, T. L. McAbee *et al.* Physics Reports **201**, 57 (1991).

[53] J. M. Lohr and W. Haeberli. Nuclear Physics A **232**, 381 (1974).

[54] W. W. Daehnick, J. D. Childs and Z. Vrcelj. Phys. Rev. C **21**, 2253 (1980).

[55] S. S. Ipson, W. Booth and J. G. B. Haigh. Nuclear Physics A **206**, 114 (1973).

[56] J. Rekstad, I. Espe, G. Lvhiden *et al.* Nuclear Physics A **369**, 453 (1981).

[57] A. S. de Toledo, H. Hafner and H. V. Klapdor. Nuclear Physics A **320**, 309 (1979).

[58] F. T. Baker and R. Tickle. Phys. Rev. C **5**, 182 (1972).

[59] J. H. Barker and J. C. Hiebert. Phys. Rev. C **4**, 2256 (1971).

[60] G. Bassani and J. Picard. Nuclear Physics A **131**, 653 (1969).

[61] M. Dost and W. R. Hering. Physics Letters **19**, 488 (1965).

[62] L. J. B. Goldfarb, G. W. Greenlees and M. B. Hooper. Phys. Rev. **144**, 829 (1966).

[63] D. J. Baugh, J. A. R. Griffith and S. Roman. Nuclear Physics **83**, 481 (1966).

[64] J. Griffith and S. Roman. Physics Letters **19**, 410 (1965).

[65] M. D. Cohler, N. M. Clarke, C. J. Webb *et al.* Journal of Physics G: Nuclear Physics **2**, L151 (1976).

[66] B. H. Wildenthal, B. M. Preedom, E. Newman *et al.* Phys. Rev. Lett. **19**, 960 (1967).

[67] D. W. L. Sprung and P. C. Bhargava. Phys. Rev. **156**, 1185 (1967).

[68] W. Booth, S. Wilson and S. S. Ipson. Nuclear Physics A **238**, 301 (1975).

[69] P. R. Christensen, B. Herskind, R. R. Borchers *et al.* Nuclear Physics A **102**, 481 (1967).

[70] K. Heyde and P. J. Brussaard. Zeitschrift für Physik A Hadrons and Nuclei **259**, 15 (1973). 10.1007/BF01394476.

[71] A. Chalupka, W. Bartl, L. Schnauer *et al.* Nuclear Instruments and Methods in Physics Research **217**, 113 (1983).

[72] R. Krucken. private communication (2010).

[73] B. K. Kay. private communication (2010).

[74] A. Wuosmaa, J. Schiffer, B. Back *et al.* Nuclear Instruments and Methods in Physics Research Section A: Accelerators, Spectrometers, Detectors and Associated Equipment **580**, 1290 (2007).

[75] G. Savard, S. Baker, C. Davids *et al.* Nuclear Instruments and Methods in Physics Research Section B: Beam Interactions with Materials and Atoms **266**, 4086 (2008). Proceedings of the XVth International Conference on Electromagnetic Isotope Separators and Techniques Related to their Applications.

[76] Y. Khazov, A. Rodionov, S. Sakharov *et al.* Nuclear Data Sheets **104**, 497 (2005).

[77] D. Radford, C. Baktash, C. Barton *et al.* Nuclear Physics A **752**, 264 (2005). Proceedings of the 22nd International Nuclear Physics Conference (Part 2).

[78] J. Terasaki, J. Engel, W. Nazarewicz *et al.* Phys. Rev. C **66**, 054313 (2002).

[79] L. G. Moretto and R. P. Schmitt. Reports on Progress in Physics **44**, 533 (1981).

[80] A. Winther. Nuclear Physics A **572**, 191 (1994).

[81] R. Broda. Eur. Phys. J. A **13**, 1 (2002).

[82] L. Corradi, A. Stefanini, A. Vinodkumar *et al.* Nuclear Physics A **701**, 109 (2002). 5th International Conference on Radioactive Nuclear Beams.

[83] L. Corradi, A. M. Stefanini, C. J. Lin *et al.* Phys. Rev. C **59**, 261 (1999).

[84] A. Winther. Nuclear Physics A **594**, 203 (1995).

[85] A. Gadea. private communication (2009).

[86] G. Montagnoli. IP conference proceedings **610**, 942 (2002).

[87] A. Gadea. private communication (2008).

[88] G. Montagnoli, A. Stefanini, M. Trotta *et al.* Nuclear Instruments and Methods in Physics Research Section A: Accelerators, Spectrometers, Detectors and Associated Equipment **547**, 455 (2005).

[89] S. Beghini, L. Corradi, E. Fioretto *et al.* Nuclear Instruments and Methods in Physics Research Section A: Accelerators, Spectrometers, Detectors and Associated Equipment **551**, 364 (2005).

[90] A. Gadea, D. Napoli, G. Angelis *et al.* The European Physical Journal A - Hadrons and Nuclei **20**, 193 (2003). 10.1140/epja/i2002-10352-9.

[91] J. J. Valiente-Dobón. private communication (2008).

[92] A. Latina. Ph.D. thesis, Università Degli Studi Di Torino (2004).

[93] A. Gottardo. Ph.D. thesis, Università Degli Studi Di Padova (2007).

[94] A. Gadea. private communication (2010).

[95] J. Simpson. Journal of Physics G: Nuclear and Particle Physics **31**, S1801 (2005).

[96] J. J. Valiente-Dobón, D. Mengoni, A. Gadea *et al.* Phys. Rev. Lett. **102**, 242502 (2009).